UNIVERSITÀ
DEGLI STUDI
DI PADOVA

Sede Amministrativa: Università degli Studi di Padova
Dipartimento di Fisica e Astronomia

SCUOLA DI DOTTORATO DI RICERCA IN ASTRONOMIA
CICLO XXVIII

INVESTIGATION OF GAMMA-RAY PULSARS WITH THE CHERENKOV TELESCOPE ARRAY AND THE ASTRI MINI-ARRAY

Direttore della Scuola: Ch.mo Prof. Giampaolo Piotto
Supervisore: Dott. Luca Zampieri

Dottorando: Aleksandr Burtovoi

"Truth doesn't make a noise..."

Jack White

UNIVERSITÀ DEGLI STUDI DI PADOVA

Abstract

Dipartimento di Fisica e Astronomia

Doctor of Philosophy

Investigation of Gamma-ray Pulsars with the Cherenkov Telescope Array and the ASTRI Mini-array

by Aleksandr Burtovoi

This Thesis presents the prospects for investigating gamma-ray pulsars with future Cherenkov facilities, the Cherenkov Telescope Array (CTA) and ASTRI mini-array (possible precursor for CTA). Gamma-ray pulsars are compact astrophysical objects which emit photons with energies up to ∼100 GeV. The nature of the gamma-ray emission from these sources is not fully understood. In addition, the recent detection of the Crab pulsar with Cherenkov telescopes such as MAGIC and VERITAS at very high energies (VHE, >100 GeV) challenged current theoretical models. CTA will be a next-generation ground-based VHE gamma-ray instrument, designed to achieve a sensitivity of the order of one magnitude better than that of currently operating Cherenkov installations. It will consist of two arrays, one in northern and one in southern hemisphere, each with a large number of different-sized telescopes. Early observations can be carried out with CTA precursors, such as the ASTRI mini-array. I simulated the VHE emission from the 12 most energetic *Fermi* pulsars. I analyzed the *Fermi*-LAT data of these pulsars above 10 GeV and extrapolated their gamma-ray spectra up to ∼160 TeV, in order to estimate how many of them will be detectable with CTA. In addition, I performed a detailed investigation of the pulsed VHE emission from the Crab pulsar, simulating the light curve detectable with CTA. I calculated with which accuracy it will be possible to study the timing properties of this pulsar with CTA and the ASTRI mini-array. Finally, I investigated VHE gamma rays from the Vela X region. Assuming different spatial distributions for the emission from the Vela pulsar wind nebula, I calculated more realistic estimates of the significance of the Vela pulsar detection with CTA. Using different software packages (*ctools* and *Asrtisim*), I also studied the extended Vela X emission and tested the resolving capabilities of CTA and the ASTRI mini-array.

UNIVERSITÀ DEGLI STUDI DI PADOVA

Abstract

Dipartimento di Fisica e Astronomia

Dottorando

Studio dell'emissione delle Gamma-ray Pulsars con il Cherenkov Telescope Array ed il Mini-array ASTRI

Aleksandr Burtovoi

Questa Tesi contiene i risultati di uno studio dell'emissione delle pulsar a raggi gamma osservate con futuri telescopi Cherenkov, il Cherenkov Telescope Array (CTA) ed il mini-array ASTRI (uno dei possibili precursori per CTA). Le pulsar a raggi gamma sono oggetti astrofisici compatti che emettono fotoni con energie fino a ∼100 GeV. La natura dell'emissione di raggi gamma da queste sorgenti non è chiara. Inoltre, la recente rivelazione di emissione di altissima energia (VHE, >100 GeV) da parte della Crab pulsar con i telescopi Cherenkov MAGIC e VERITAS reppresenta una sfida per attuali modelli teorici. CTA sarà uno strumento nuova generazione, progettato per raggiungere una sensibilità un'ordine di grandezza migliore di quella dei telescopi Cherenkov attualmente in funzione. Esso comprenderà un array in ciascun emisfero con un gran numero di telescopi di dimensioni diverse. Le prime osservazioni verranno eseguite con precursori di CTA, come il mini-array ASTRI. Ho simulato l'emissione VHE dalle 12 *Fermi* pulsar più energiche. Ho analizzato i dati *Fermi*-LAT di queste pulsar ad energie superiori a 10 GeV ed estrapolato i loro spettri gamma fino a ∼ 160 TeV, per stimare quante di loro saranno rivelabili con CTA. Inoltre, ho eseguito un esame più dettagliato dell'emissione VHE pulsata dalla Crab pulsar, simulando la curva di luce osservabile con CTA. Ho calcolato con quali accuratezza sarà possibile studiare le proprietà del timing di questa pulsar con CTA ed il mini-array ASTRI. Infine, ho studiato l'emissione di altissima energia (VHE) dalla sorgente Vela X. Assumendo diverse distribuzioni spaziali per l'emissione della wind nebula della Vela pulsar, ho calcolato stime più realistiche delle significativita della Vela pulsar con CTA. Utilizzando diversi pacchetti software (*ctools* e *Asrtisim*), ho anche studiato l'emissione estesa della Vela X e verificato la risoluzione angolare ottenibile con CTA ed il mini-array ASTRI.

Acknowledgements

I am very grateful to all people who supported and helped me during three years of my PhD.

First of all, I would like to thank my supervisor Dr. Luca Zampieri for being my mentor during the PhD course, for teaching me and for answering all my questions. Your advices and suggestions significantly improved the level of my scientific research. I appreciate deeply all your help to me.

I am also grateful to Dr. Takayuki Saito for his help and collaboration. I learned a lot from our scientific discussions. Your very useful suggestions about the *Fermi* Science tools saved a lot of my time.

I am very happy to have a chance to work within the ASTRI Collaboration during my PhD course, especially with the ASTRI Science team. My gratitude to Dr. Stefano Vercellone for his interest and useful comments and suggestions to my work. I also thank Dr. Andrea Giuliani for introducing me the scientific software of the ASTRI team and for the chance to take a part in the development of this software. I am grateful to Dr. Enrico Giro and Dr. Maria Concetta Maccarone for their help with numerous organizational questions that I had.

I would like to thank Prof. Diego Torres and Dr. Emma de Oña-Wilhelmi and other guys from the high-energy group at the Institute of Space Sciences (Barcelona), with whom I had a pleasure to work during my 2-month stay in Barcelona. I learned a lot from this collaboration.

I thankful to members of the CTA Consortium for all their suggestions and comments to my work. Such a feedback helped to improve different aspects of my PhD Project.

I would like to thank Dr. Marina Orio, particularly for her significant help and support during the very first months of my PhD. Many thanks also to all my friends from Russia, University of Padova and from other places.

Finally, I would like to thank my family for supporting me all this time, specially my parents, my sister and brother-in-law. For sure, I would not be where I am now without my wife Polina, who went with me side-by-side all these years. Your care and support brought peace and calm to my soul during the most difficult parts of the PhD path. Thank you for all.

Contents

List of Figures

List of Tables

Abbreviations

1FHL	The First *Fermi*-LAT Catalog of >10 GeV Sources
2FGL	The Second *Fermi*-LAT Catalog
2PC	The Second *Fermi*-LAT Catalog of Gamma-ray Pulsars
AGN	**A**ctive **G**alactic **N**ucleus
ALP	**A**xion-**l**ike **P**articles
ASTRI	**A**strofisica con **S**pecchi a **T**ecnologia **R**eplicante **I**taliana
C. U.	**C**rab **U**nit
CMB	**C**osmic **M**icrowave **B**ackground
CTA	**C**herenkov **T**elescope **A**rray
DM	**D**ark **M**atter
EBL	**E**xtragalactic **B**ackground **L**ight
GC	**G**lobular **C**lusters
GRB	**G**amma-ray **B**ursts
HE	**H**igh **E**nergy
H.E.S.S.	**H**igh **E**nergy **S**tereoscopic **S**ystem
HPBW	**H**alf-**p**ower **B**eam **W**idth
IACT	**I**maging **A**tmospheric **C**herenkov **T**elescope
IC	**I**nverse **C**ompton
IGMF	**I**nter**g**alactic **M**agnetic **F**ield
IRF	**I**nstrument **R**esponse **F**unction
KSP	**K**ey **S**cience **P**rogram
LIV	**L**orentz **I**nvariance **V**iolation
LMC	**L**arge **M**agellanic **C**loud
LST	**L**arge **S**ize **T**elescopes
MAGIC	**M**ajor **A**tmospheric **G**amma **I**maging **C**herenkov Telescopes

MC	**M**onte **C**arlo
MGPS-2	Second **M**olongo **G**alactic **P**lane **S**urvey
MSP	**M**illi**s**econd **P**ulsar
MST	**M**edium **S**ize **T**elescopes
OG	**O**uter **G**ap
OP	**O**ff-**p**eak
PC	**P**olar **C**ap
PLEC	**P**ower-**L**aw With **E**xponential **C**ut-off
Prod1	**P**roduction 1
Prod2	**P**roduction 2
PSF	**P**oint **S**pread **F**unction
PSPC	**P**osition **S**ensitive **P**roportional **C**ounters
PWN	**P**ulsar **W**ind **N**ebula
RASS	**R**OSAT **A**ll **S**ky **S**urvey
ROI	**R**egion **O**f **I**nterest
SG	**S**lot **G**ap
SNR	**S**uper**n**ova **R**emnant
SST(-2M)	**S**mall **S**ize **T**elescopes (**D**ual-**M**irror)
TS	**T**est **S**tatistic
VERITAS	**V**ery **E**nergetic **R**adiation **I**maging **T**elescope **A**rray **S**ystem
VHE	**V**ery **H**igh **E**nergy

Physical Constants

Speed of Light	c	=	$2.997\ 924\ 58 \times 10^{8}$ ms$^{-\mathrm{S}}$ (exact)
1 Crab Unit	1 C.U.	=	$2.79 \times 10^{-11} \times (E/1\ \mathrm{TeV})^{-2.57}$ cm^{-2} s^{-1} TeV^{-1}
1 mCrab		=	$10^{-3} \times 1$ C.U.

Dedicated to Polina, my beloved wife...

Chapter 1

Introduction

1.1 Very High Energy Gamma-ray Astronomy

Very high energy (VHE) gamma-ray astronomy investigates astrophysical sources that emit photons with energies above 100 GeV. It is a relatively new branch of high-energy astronomy. The first VHE source – the Crab Nebula – was detected in 1989 [1]. Significant progress in the investigation of VHE gamma-ray phenomena has been made in recent years thanks to the entering in operation of ground-based Imaging Atmospheric Cherenkov Telescopes (IACTs) such as MAGIC, VERITAS and H.E.S.S. Nowadays, about 150 Galactic and extragalactic sources are known at VHE (Fig. 1.1).

In general, VHE gamma-ray emission can be associated with the acceleration of relativistic particles (leptons and hadrons). There is a wide range of astrophysical regions inside our Galaxy and beyond it, where acceleration processes occur with different intensities. Then it is very important to investigate the TeV energy domain, the highest band of the electromagnetic spectrum ever observed, because it provides information concerning the location and nature of particle acceleration in various environments across the Universe. Detecting energetic gamma-ray photons from different astrophysical objects, we can study physical processes under particular conditions, unachievable in the laboratory, and constrain theoretical models of both astrophysics and fundamental physics.

1.1.1 Pulsars

One of the more compact sources of VHE photons is a gamma-ray pulsar, an isolated rotation-powered neutron star. Its rotational energy is converted into the relativistic motion of electrons and positrons, which produce gamma-ray emission up to a few TeV.

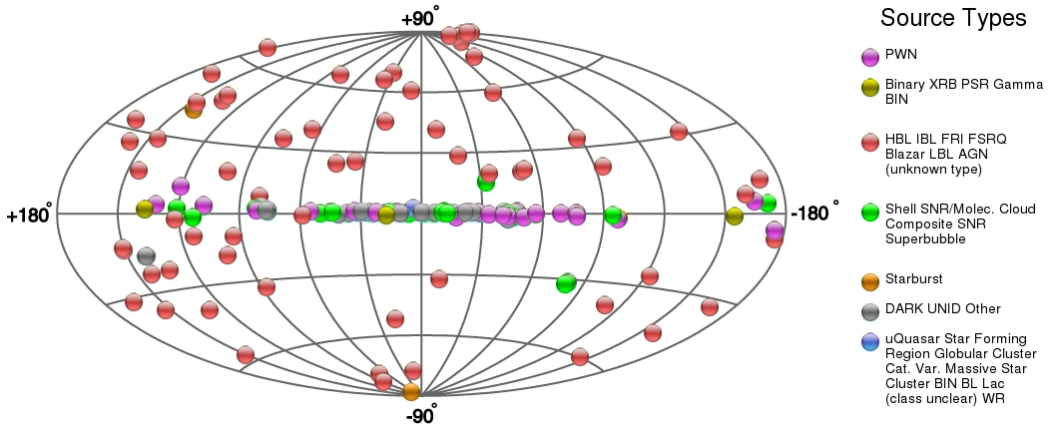

FIGURE 1.1: Map of VHE gamma-ray sources in Galactic coordinates, taken from the TeVCat catalog [2] as of 07/2015 (http://tevcat.uchicago.edu/).

Gamma-ray pulsars are the subject of this Thesis. They are presented and discussed in detail in Sect. 1.2.

1.1.2 Pulsar Wind Nebulae

Pulsar wind nebulae (PWNe) are strongly connected with pulsars activity. The winds of relativistic particles produced by the pulsar transfer the rotational energy of the neutron star to the surrounding medium, forming shocks at which particles are accelerated. Interacting with the intrinsic magnetic field of the medium and/or with background photons, these particles produce the non-thermal emission of the PWN that covers the whole electromagnetic spectrum. Several dozens of PWNe have been observed so far at VHE [3]. It is the most numerous class of detected VHE objects observed inside and outside our Galaxy. The extragalactic pulsar wind nebula N 157B located in the large Magellanic Cloud (LMC) was discovered by the H.E.S.S. Collaboration [4].

The brightest and best studied VHE source in the gamma-ray sky is the Crab Nebula. This PWN is used as a standard candle for TeV observations. Investigations of the Crab Nebula emission performed at all wavelengths (from the radio up to VHE gamma rays) allowed to shed light on the acceleration mechanisms and emission processes within PWNe. As mentioned above, the population of electrons which power the nebula is believed to be accelerated up to energies of about 10^{15} eV in relativistic outflows originating from the neutron star (pulsar winds) [5] and in termination shocks, where the pulsar wind interacts with the surrounding medium [6]. The mechanism of the particle acceleration up to the highest observed energies ($\sim 10^{15}$ eV) is still under debate (e.g. [7, 8]). Energetic particles injected into the PWN interact with the intrinsic magnetic field of the nebula and produce synchrotron emission in a broad energy range from the radio up to gamma rays below $\sim$1 GeV [6]. The high-energy gamma-ray photons above several

GeV are emitted via inverse Compton (IC) up-scattering of soft radiation fields (optical, X-ray) on relativistic electrons and positrons (see e.g. [9]). Analyzing the composite spectrum of both the low-energy synchrotron emission from the Crab Nebula, which requires the existence of a magnetic field (B), and the high-energy IC component, which is independent of B, it is possible to put constraints on the average value of the magnetic field intensity within the PWN. Inferred values are in the range $100 < B < 200$ μG [10]. Despite being considered a standard candle at other wavelengths, the Crab Nebula shows a rapid (1-day time scale) gamma-ray flaring activity, which has been observed with different gamma-ray telescopes (e.g. AGILE [11], *Fermi*-LAT [12]). During such flares (e.g. April 2011, March 2013) the high-energy part of the spectrum above 100 MeV becomes harder. This could be caused by an additional acceleration of leptons that increases both the synchrotron and IC emission [13, 14]. It is also possible that such flaring activity is produced by changes in the magnetic and/or electric field intensity occurring during reconnection events. In this case, only synchrotron emission is expected to be enhanced [15, 16]. Some models also predict gamma-ray variability of the Crab Nebula at TeV energies [13, 17]. However, only upper limits to the Crab PWN flux were found with IACTs during flares [18–20]. Further VHE gamma-ray studies are required to advance our knowledge concerning the nature of the very high energy variability of the Crab Nebula.

The acceleration and emission mechanisms of other PWNe are in general similar to those of the Crab Nebula. Some differences can occur with the age of PWNe. Young nebulae are seen at TeV energies as point sources with position consistent with that in the X-rays (e.g. Crab Nebula [9, 21, 22], HESS J1813−178 [23, 24]). The extended VHE emission from evolved PWNe (age $>10^4$ years) is usually larger than that in the X-rays (e.g. Vela X [25], HESS J1825−137 [26]). Pulsars which belong to old nebulae are observed offset from the center of the extended PWN emission. This is probably caused by the proper motion of the neutron star and/or by the deformation of the shape of the PWN after interacting with the reverse shock from the supernova remnant (SNR) [27]. The time scale of such process is about 10^4 years.

1.1.3 Supernova Remnants

A supernova explosion is the phenomenon which happens at the final stage of the evolution of a massive star $\gtrsim 8M_\odot$ (core-collapse supernova, for details see e.g. [28, 29]) or when the mass of a white dwarf exceeds the Chandrasekhar limit (thermonuclear supernova, for details see e.g. [30, 31]). During such events a huge amount of energy ($\sim 10^{51}$ erg) is released. The outer layers of the star expand very rapidly, interacting

with the surrounding medium and forming a shell-like SNR visible at different wavelengths. Several SNRs have been detected in VHE gamma rays: e.g. RX J1713.7−3846 [32], Vela Junior (RX J0852.0-4622) [33], Cas A [34, 35], Tycho [36] and SN 1006 [37]. The non-thermal gamma-ray emission from young SNRs (age $<10^4$ years) is produced by the population of relativistic particles (leptons and hadrons) that are accelerated in the supernova shocks through the first order Fermi acceleration mechanism[1] [38, 39]. The existence of a leptonic population in SNRs is confirmed by the detection of X-ray synchrotron emission within their thin filaments (see e.g. [40, 41]). Gamma-ray observations (e.g. [42]) detected also signatures of pion decay in supernova remnants, which points to the presence of a relativistic hadronic population. The VHE emission from SNRs can then be explained by IC scattering on energetic leptons (leptonic scenario) or/and by neutral pion decay (hadronic scenario). Although it is still unknown what mechanism plays the major role in the production of TeV photons, one can compare the high-resolution VHE morphology of a supernova remnant with that observed in radio and X-rays and try to quantify the ratio between the leptonic and hadronic populations (for more details see e.g. [43]).

To date SNRs are the best-candidate sites for acceleration of Galactic cosmic rays up to PeV energies. Such objects, called PeVatrons, are believed to produce extremely high-energy photons at energies >100 TeV. Since the Klein-Nishina cross-section of the electron-photon IC scattering is very small above few TeV, significant energetic gamma-ray emission at 100 TeV energies is not likely to be produced by leptons. Hadronic cosmic rays with PeV-energies are able to produce 100 TeV photons, e.g. through pion decay. Future VHE observations at energies >100 TeV will help us to clarify whether SNRs are efficient accelerators of Galactic cosmic rays and can be associated with PeVatrons.

1.1.4 Other Galactic Sources of VHE Gamma-ray Emission

Acceleration processes can occur also in star-forming regions and young stellar clusters. Supersonic stellar winds of young massive stars interact with each other, with the surrounding medium or with SNR shells and form shock fronts, where particles can be accelerated [44]. Star forming regions and young stellar clusters are possible candidates of the Galactic cosmic-ray accelerators, which can be observed with IACTs at VHE [45, 46].

TeV gamma-ray binaries are another class of VHE emitters. These sources consist of a massive star and a neutron star or black hole. The VHE emission from gamma-ray

[1] The first order Fermi acceleration mechanism is the acceleration of charged particles which repeatedly cross the shock front reflecting back and forth on magnetic inhomogeneities in the environment (magnetic mirrors).

binaries originates from acceleration processes in either relativistic jets energized by ongoing accretion (microquasars [47, 48]) or in shocks, where a pulsar wind interacts with the circumstellar environment [49]. The most famous and firmly identified VHE binary systems are PSR B1259−63 [50], HESS J0632+057 [51], LS 5039 [52] and LS I+61°303 [53, 54]. For example, PSR B1259−63 is a system of a massive Be star and a pulsar, whereas Cygnus X-1 is a binary system with an accreating black hole [48, 55].

1.1.5 Review of Extragalactic VHE sources

One of the closest extragalactic sources observed at VHE is the LMC – a satellite of the Milky Way Galaxy. As mentioned in Sect. 1.1.2, the first VHE extragalactic PWN N 157B was detected in the LMC [4]. The SNR N132D and a star-forming region 30 Doradus were discovered in VHE gamma rays with H.E.S.S. [56]. The LMC is an approximately face-on galaxy (inclination angle is ∼30–40° [57]) located at a distance of 50 kpc [58]. Being a galaxy with a high star formation rate[2], the LMC comprises regions, where an effective particle acceleration can occur: star-forming regions, more than 60 SNRs [59], dozens of HII regions [60], bubbles [61] and shells [62]. This makes the LMC a very fruitful target for the present and future VHE observations.

More distant extragalactic VHE gamma-ray emitters are associated basically with active galactic nuclei (AGNs). In these objects an accretion on the central super massive black hole ($M_{\mathrm{BH}} \gtrsim 10^7\, M_\odot$) is believed to cause an ejection of relativistic jets, in which the hadronic and leptonic particles can be accelerated. Almost all extragalactic sources (∼60) detected at VHE belong to the blazar class. Blazars are AGNs with jets pointed to an observer. Analyzing high-energy spectra of a large number of these active galaxies one can test the gamma-ray emission models, which describe the acceleration mechanisms in the AGN jets. Another class of AGNs detected at VHE is associated with radio galaxies. In contrast to blazars, their jets are not aligned with the direction to the Earth, and thus the Doppler boosting effect does not take place. This makes radio galaxies much fainter comparing with blazars. For this reason, only nearby radio galaxies have been detected at VHE so far (M 87, Centaurus A and NGC 1275). An investigation of such objects provides an opportunity to map a morphology of jets in VHE gamma rays and to study gamma-ray AGN activity less biased by relativistic beaming effects. Both the leptons and hadrons are supposed to be accelerating in jets of AGNs, emitting the gamma-ray photons. However, the ratio between hadronic and leptonic gamma-ray fluxes is not certainly determined. The mechanism of the VHE emission originated in jets of an AGN is also under debate. Another feature of active galaxies is the temporal variability

[2]The star formation rate of the LMC is equal to 10% of that in the Milky Way and distributed in 2% of its volume

of their luminosity down to minutes scale. The most rapid flux variation puts a strong constraint on the size of the emitting region [63]. More detailed review of the VHE properties of AGNs is reported in e.g. [64, 65].

At high red shifts (z>0.3) the population of detected VHE gamma-ray AGNs decreases significantly because of the attenuation of the VHE gamma-ray flux. TeV photons interact with the extragalactic background light (EBL) producing electron-positron pairs. The EBL can provide an important information concerning the star formation history of the Universe. Observing a distant TeV sources at different energies and assuming a reasonable model of their spectra, one can reconstruct the properties of the EBL (see e.g. [66]).

There is also a possibility to study the intergalactic magnetic field (IGMF) by searching for so-called "pair halos" around the source and delays in the time of arrival ("pair echoes") of gamma-ray photons (see e.g. [67]). Electrons and positrons, produced by the interaction of TeV and EBL photons, are deflected in the IGMF. A part of the charged particles can then interact with the low-energy background photon field and produce gamma rays via IC scattering. Directions and times of arrival of the re-produced photons will differ from the primary TeV photons. This leads to appearing of the "pair halos" and delayed "pair echoes".

Starburst galaxies, which show very high star formation rate, are believed to produce extragalactic cosmic rays up to 10^{16} eV and, therefore, VHE gamma-ray photons. So far, only two starburst galaxies are detected at VHE: M82 [68] and NGC 253 [69].

Gamma-ray bursts (GRBs) are extremely energetic explosions occurred at cosmological distances (see [70] for the review). GRBs can be classified by the duration of their burst. Progenitors of "short" bursts (duration of $\lesssim$2 s) are believed to be two coalescing neutron stars, whereas "long" GRBs with the duration of $\gtrsim$2 s are supposed to be supernova explosions of very massive stars with a subsequent formation of the black holes. Although no GRB has been detected with the present IACTs, this class of objects is rather promising for the future Cherenkov telescopes with high sensitivity level (more details in [71]).

1.1.6 Fundamental Physics: Investigations of Dark Matter, Axion-Like Particles and Lorentz Invariance Violation

In addition to the astrophysical issues, VHE gamma-ray observations can contribute to a number of fundamental physics studies like searches of the dark matter (DM) annihilation, the axion-like particles (ALPs) and Lorentz invariance testing.

According to the current paradigm, galaxies were formed at deep gravitational wells produced by DM. A high concentration of baryonic matter assumes a high density of DM in this region. Several theories predict that DM particles are able to annihilate producing gamma-ray photons. The spectrum of such emission is not typical for any other astrophysical object. For instance, it may contain sharp line-like features at energies close to the DM mass [72]. For indirect DM searches the center of our Galaxy is the closest target. However, it is contaminated by emission from numerous astrophysical sources (SNR, PWN, etc), which is difficult to account for. Several observations of the Galactic Center aimed to detect photons from the DM annihilation have been carried out with the currently operating IACTs [73–75]. Other objects, such as dwarf galaxies and galaxy clusters, are situated in less crowded regions on the sky and can be also investigated during DM observations (see e.g. [76–78]). So far, gamma-ray observations yielded only estimates of the upper limits to the mass of a DM particle.

Observations of distant VHE sources (e.g. AGNs) can help in searches of axions or ALPs – elementary particles, which were proposed as a solution of the strong-CP problem of quantum chromodynamics (for the review see e.g. [79]). Theory predicts that ALPs can be born through the electromagnetic interaction of TeV photons with a magnetic field (and vice versa). Because of this process a part of the gamma-ray emission from an AGN can be converted into ALPs in the magnetic field of a galaxy cluster/group. Propagating in the intergalactic medium without absorption, these particles can interact with the magnetic field of the Milky Way producing TeV photons (see e.g. [80]). This is expected to be observed as an excess of the VHE part of the AGN spectrum obtained with IACTs.

Lorentz invariance is a fundamental concept of the present-day theoretical physics according to which the speed of light in vacuum is constant and does not depend on the photon energy. Some models of quantum gravity (see e.g. [81]) assume a variation of the speed of photons with energy, called the Lorentz invariance violation (LIV). In TeV astronomy LIV can be tested by measuring a delay in time of arrival of photons with different energies, emitted simultaneously from an astrophysical object. If LIV occurs, the speed of light can be expanded as:

$$c(E) = c_0 \left[1 - \sum_{n=1}^{\infty} s_{\pm} \frac{n+1}{2} \left(\frac{E}{E_{\mathrm{LIV}}} \right)^n \right] , \tag{1.1}$$

where c_0 is a speed of light at low energies ($\approx 3 \times 10^{10}$ cm/s), $s_{\pm}$ equals to $+1/-1$ in the subluminal/superluminal case, E_{LIV} is the energy at which the LIV effects become non-negligible. If the linear term of Eq. (1.1) is dominant, the difference in the arriving time of high-energy (E_{high}) and low-energy (E_{low}) photons from the source situated at

the distance d will be the following ($s_{\pm} = +1$):

$$\Delta t_1 = \frac{d}{c_0} \frac{E_{\rm high} - E_{\rm low}}{E_{\rm LIV}} \,, \tag{1.2}$$

and if the quadratic term dominates:

$$\Delta t_2 = \frac{3d}{2c_0} \frac{E^2_{\rm high} - E^2_{\rm low}}{E^2_{\rm LIV}} \,. \tag{1.3}$$

As follows from Eqs. (1.2) and (1.3), distant sources, such as AGNs and GRBs, sufficiently bright at both the high and low energies, are the most promising targets for probing LIV [82]. Flaring activity of these objects allows to stamp precisely the time of arrival of photons with different energies. So far, only the linear (Eq. (1.4)) and quadratic (Eq. (1.5)) terms can be stringently constrained.

$$E_{\rm LIV} = \frac{d}{c_0} \frac{E_{\rm high} - E_{\rm low}}{\Delta t_1} \,. \tag{1.4}$$

$$E_{\rm LIV} = \sqrt{\frac{3d}{2c_0} \frac{E^2_{\rm high} - E^2_{\rm low}}{\Delta t_2}} \,. \tag{1.5}$$

Analyzing the *Fermi*-LAT data, Bolmont et al. [82] obtained lower limits to the linear and quadratic terms of $E_{\rm LIV}$ equal to $\sim 10^{20}$ GeV and $\sim 10^{11}$ GeV, respectively. It should be noted that since the nature of AGN flares and GRBs is not fully understood, the measured time shift can be due to some unknown intrinsic process and not to LIV effects.

Other astrophysical candidates for the LIV testing are gamma-ray pulsars [83]. Measuring the shift between the pulse positions at different energies, one can constrain the value of $E_{\rm LIV}$. Although the distances to known pulsars does not exceed few kiloparsecs, which is much lower than those to AGNs and GRBs, the almost regular (not flaring) periodic emission from neutron stars allows us to accumulate data during a long period of time and perform more precise measurements of the time shift in different energy bands. Present VHE observations of the Crab pulsar yielded the upper limits to the linear term of $E_{\rm LIV} > 3 \times 10^{17}$ GeV and to the quadratic term of $E_{\rm LIV} > 7 \times 10^{9}$ GeV [83].

1.2 Gamma-ray Pulsars

Isolated pulsars are young, rapidly rotating ($P = 10^{-3} \div 10$ s) and highly magnetized ($B = 10^{10} \div 10^{12}$ G) neutron stars, which represent one of the few rare multiwavelength laboratories in our Galaxy. Many of them show emission from the radio waves up to the extremely energetic gamma rays [84–87]. Being a time-varying dipole, an isolated pulsar

converts its rotational energy into electromagnetic radiation. In addition, it is believed to accelerate particles (mainly electrons and positrons) up to relativistic energies. Moving in the strong magnetic field of the neutron star, energetic electrons and positrons emit photons in different energy bands. However, the detailed mechanism of such emission is still largely debated [see e.g. 88, 89].

Gamma-ray emission from pulsars has been discovered with the SAS-2 telescope (see [90] and [91]). EGRET increased the number of detected pulsars to ∼10. Since the gamma-ray counts from pulsars are low, it is essentially impossible to detect the pulse profile within a single rotational period. However, taking into account the stable rotation of the neutron star (as a first approximation), one can obtain their light curves during long-term observations, folding the data on a certain time interval. A breakthrough on the observations of the gamma-ray pulsars was achieved with the launch of the current generation of gamma-ray space telescopes as AGILE [92] and *Fermi* [93]. About 150 pulsars were detected with the *Fermi*-LAT [94]. It was also found that 20 (12) of them show significant pulsations at energies >10 GeV (>25 GeV) [95]. So far only two pulsars have been detected with IACTs. The Crab pulsar was observed with MAGIC [96–98] (up to 1 TeV) and with VERITAS [99] (up to 400 GeV). A light curve of the Vela pulsar at energies <100 GeV was recently obtained with the H.E.S.S. instrument[3].

Different models have been proposed to explain the nature of the pulsed gamma-ray emission from pulsars (see Fig. 1.2). Goldreich and Julian [100] investigated a simple model of a rotating neutron star with a dipole magnetic field. The magnetic moment $\boldsymbol{\mu}$ is aligned with the rotational axis $\boldsymbol{\Omega}$. In this case, they showed that a quadrupole electric field appears outside the surface. At the polar cap there is a component of the electric field $E_{\parallel}$ parallel to the external magnetic field and strong enough to pull out particles (mostly electrons) from the surface of the pulsar.

$$E_{\parallel} \sim \frac{\Omega R B_p}{c} \sim 2 \times 10^8 \, B_{12}/P \text{ volt cm}^{-1}\,, \tag{1.6}$$

where R is the radius of the neutron star, $B_p \equiv 2\mu/R^3$, B_{12} is the magnetic field in units of 10^{12} G and $P = 2\pi/\Omega$ is the rotational period in seconds.

This process occurs until the electrons screen the parallel electric field. The critical charge density required for screening $E_{\parallel}$ is called the Goldreich-Julian density:

$$\rho_{\text{GJ}} = -\frac{(\boldsymbol{\Omega}\,\mathbf{B})}{2\pi c}. \tag{1.7}$$

[3] http://www.mpg.de/8287998/velar-pulsar

This pair plasma fills the magnetosphere around the neutron star. It is frozen along the magnetic field lines and therefore co-rotates with the pulsar. Such a rotation is possible within a cylinder with radius $R_{\rm L} = c/\Omega$ (light cylinder), within which the rotational velocity is lower than the speed of light c and the magnetic field lines are closed. Since the velocity of particles can not be higher than c, the magnetic lines that intersect the light cylinder are open. Electrons and positrons, which are moving along such field lines, escape from the magnetosphere, taking away the energy of the pulsar and leaving the $E_{\parallel}$ component unscreened.

Following the idea of Goldreich and Julian [100], Sturrock [101] proposed a polar cap (PC) model, which was later developed by e.g. [102–104]. In this model particles extracted from the surface and accelerated by the parallel electric field, move along the curved magnetic field lines and emit curvature radiation (up to $\sim$1 GeV). These gamma-ray photons interact with the strong magnetic field and produce e^--e^+ pairs. Secondary particles emit then synchrotron/curvature gamma rays, which produce the next generation of electrons and positrons. Such processes will continue in the PC regions near the surface of the neutron star (at a height smaller than 10 km, see Fig. 1.2) until the energies of the emitted photons become lower than the pair-production threshold. Survived high-energy photons contribute to the observed optical-through-gamma-ray emission from the pulsar. The instabilities in the electron-positron plasma are believed to be responsible for the coherent radio emission. Particle acceleration and pair-production processes occur in the regions, where the $E_{\parallel}$ component remains unscreened, i.e. in the regions of open magnetic field lines.

The production of secondary electrons directly at the magnetic poles is not effective because of the low curvature of the magnetic field lines and, thus, the low intensity of the curvature photons. Therefore, the plasma density in the inner part of the PCs is low. Ruderman and Sutherland [102] and Oster and Sieber [105] noted this effect and proposed the hollow cone model. This model can explain the single- and double- peak pulse profiles through the different orientation of the emitting hollow cone with respect to the line of sight of an observer.

According to the PC model, the gamma-ray emission from pulsars is produced at polar caps near the surface of the neutron star. However, in this case the major part of the high-energy photons will interact with the strong magnetic field, producing e^--e^+ pairs. Arons and Scharlemann [106] proposed an alternative slot gap (SG) model. Since the parallel electric field $E_{\parallel}$ decreases near the outer boundary of the PC, a larger distance is required for electrons to be accelerated to sufficiently high energies to initiate cascade processes. According to the SG model, the production and acceleration of particles occur along the last open magnetic field lines, at a height of several neutron star radii

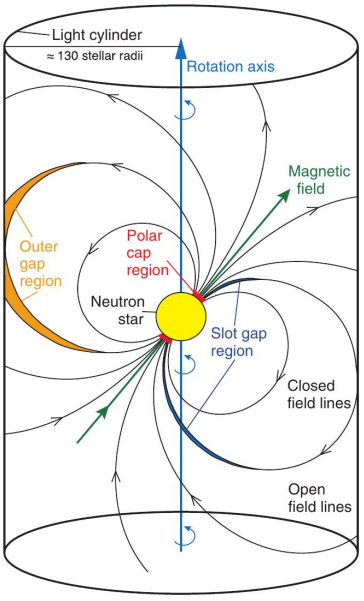

FIGURE 1.2: Schematic view of the magnetosphere of a pulsar. Polar cap, slot gap and outer gap acceleration regions are shown in red, blue and orange, respectively. (Image taken from [112]).

from the surface (so-called slot gap regions). In SGs, the unscreened electric field $E_{\parallel}$ accelerates particles, which emit gamma-ray photons (for more details, see Fig. 1.2 and [107, 108]).

Another model is based on the hypothesis that the high-energy emission originates in outer magnetospheric gaps (OGs, proposed in [109], see Fig. 1.2). According to the OG model, vacuum gaps extend from the null charge surface[4] to the light cylinder. A non-zero component of the electric field parallel to the magnetic field ($E_{\parallel}$) appears due to the return currents [109]. When the potential drop in gaps reaches the value of about 10^{16} V, pair-production and acceleration processes occur, similar to those described above for the PC model. The OG model predicts the production of gamma-ray photons at distances of a fraction of R_{L}. This decouples them from the radio emission originating in the PC region. Gamma rays are believed to be produced through the curvature and synchrotron radiation mechanisms (see e.g. [110, 111]).

For most of the gamma-ray pulsars the best fit spectral model of the emission in the 100 MeV – 100 GeV energy range is a power law with an exponential cut-off: $\mathrm{d}N/\mathrm{d}E \sim E^{-\gamma}\exp[-(E/E_c)^b]$ (see Eq. (2.2)). The values of the spectral index γ are between 0.5 and 2.5, whereas the cut-off energies E_c – between 1 and 10 GeV [87, 113]. Since in the vicinity of the PCs the gamma-ray emission is effectively attenuated due to γ-B absorption with subsequent e^--e^+ pair-production, the GeV emission from pulsars is

[4]The null charge surface (where $\mathbf{\Omega}\,\mathbf{B} = 0$) separates positive and negative charges in the magnetosphere of a pulsar.

better accounted for by the OG or SG models, which predict high-altitude emission. An investigation of the pulsating light curves provides another tool for testing different theoretical models (see e.g. [114–117]).

The detection of VHE gamma-ray emission from the Crab pulsar at energies >100 GeV puts rather strong constrains on the emission models. TeV gamma-ray emission from this pulsar was recently detected with the MAGIC telescope [118]. VHE observations showed no exponential cut-off in the spectrum of the Crab pulsar above 10 GeV. The best fit spectral model of the joint *Fermi*-LAT and VERITAS data is a broken power law: $\mathrm{d}N/\mathrm{d}E \sim (E/E_0)^{\alpha}/[1 + (E/E_0)^{\alpha-\beta}]$ (see [99]). The existence of VHE photons requires an emission region located at >10 stellar radii from the neutron star [64]. Different theoretical interpretations of the sub-TeV/TeV gamma-ray emission from the Crab pulsar are reported in e.g. [8, 14, 117, 119] and discussed in Chapter 3. Further VHE investigation of the Crab pulsar together with the discovery of other isolated neutron stars at energies >100 GeV will provide new data that will help us to improve our understanding of the gamma-ray pulsar phenomenon [120].

1.2.1 The Population of Millisecond Pulsars in Globular Clusters

Millisecond pulsars (MSPs) represent a class of old neutron stars, which were spun up to ms periods via accretion of matter from a companion star and for this reason are also called recycled pulsars [121]. About 40 gamma-ray MSPs have been discovered so far [87]. Although the typical magnetic field of millisecond pulsars is rather low ($B < 10^9$ G), the properties of their spectra and light curves in gamma rays are in general similar to those of non-recycled pulsars. It is believed that the emission mechanism of MSPs is similar to those described above. Moreover, the pulsed gamma-ray emission from source J1823-3021A is interpreted as coming from a MSP in the globular cluster NGC 6624 [123].

The population of MSPs in globular clusters (GCs) can be responsible for the unpulsed gamma-ray emission from the latter [122]. Recently, 15 GCs have been detected with *Fermi* and then listed in the Third *Fermi*-LAT Source Catalog (3FGL [94]). Some models (e.g. [124]) explain the unpulsed high-energy emission from GCs as curvature radiation of electrons and positrons accelerated in the magnetospheres of MSPs. The pulsar relativistic e^--e^+ plasma can also produce VHE photons via IC up-scattering of the softer photons produced by the surrounding stars and of the cosmic microwave background (CMB) photons. However, alternative origins for a possible VHE emission from clusters have also been proposed: leptons accelerated inside GCs (e.g. in the

colliding PWN shocks) can produce both high-energy ($\leq$100 GeV) and VHE (>100 GeV) emission through IC scattering of low-energy photons (see [125] and [126], respectively).

To date, no significant VHE gamma-ray emission from GCs has been detected with IACTs [127]. The source HESS J1747-248, observed in the close vicinity of Terzan 5 with H.E.S.S. [128], was considered as a part of the MSPs population of the nearby GC, although the origin of the significant offset ($4.0' \pm 1.9'$) from the location of Terzan 5 is still unclear.

Observations performed with future Cherenkov installations may reveal VHE emission from GCs. If the existence of VHE emission from the MSPs population is confirmed and is the main contributor to the gamma-ray flux from GCs, such high-energy observations will become a powerful tool for investigating the emission mechanisms of old recycled gamma-ray pulsars and also for studying the evolution of GCs.

1.3 Imaging Atmospheric Cherenkov Telescopes

The Earth's atmosphere is opaque for high-energy cosmic radiation. This makes direct ground-based observations in X-rays or gamma rays hardly possible. One way to overcome such natural obstacle is to carry out observations outside the atmosphere e.g. aboard space satellites. The first gamma-ray space missions, such as SAS-2 [129] and COS-B [130], were launched in 1970th. The major improvement of the sensitivity was achieved with the EGRET instrument [131], and then with the AGILE [92] and the *Fermi*-LAT [93] facilities, which are still in operation observing objects at energies up to 50 and 300 GeV, respectively. However, the steep VHE spectra of the majority of the astrophysical gamma-ray sources make the space TeV observations essentially ineffective. Upper bounds of the energy ranges of space gamma-ray telescopes are strictly limited by the size of their effective area ($\sim$1 m^2 for the *Fermi*-LAT).

Another possibility to investigate hard emission above a few tens of GeV is to perform indirect observations from the ground using the technique of IACTs. This technique is based on the phenomenon of the Cherenkov radiation discovered by P. Cherenkov in 1934. When a charged particle moves in a dielectric medium with a speed higher than the phase velocity of light in that medium, the wave front of blue Cherenkov emission appears. In 1948, Blackett [132] found out that there is a detectable contribution to the night sky emission (Cherenkov radiation) from air showers of particles, produced as a consequence of the gamma-ray photons and/or cosmic rays interactions with the upper layers of the Earth's atmosphere. An idea of an indirect detection of gamma rays, using the atmosphere as a part of an instrument, underlies the IACTs technique.

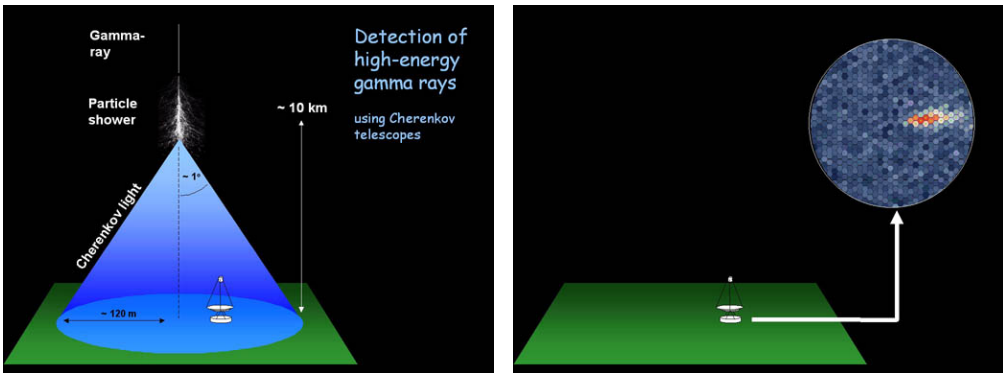

(A) (B)

FIGURE 1.3: The schematic view of the IACTs technique: (A) formation of the Cherenkov light pool; (B) detection of the Cherenkov light (and primary gamma-ray photon) with IACT. (Images taken from http://www.mpi-hd.mpg.de/hfm/HESS/).

1.3.1 The IACTs Observation Technique

Passing through the atmosphere, a gamma ray (primary) interacts with its upper layers at an altitude of ∼25 km and produces a particle shower. The energy of the primary is so high that produced particles (mainly electrons) are moving with velocities higher than the speed of light in the atmosphere and, thus, emit the Cherenkov radiation. The number of particles in the air shower reaches the maximum at an altitude of ∼10 km and then it continuously decreases as the shower goes deeper into the atmosphere and looses its energy. The Cherenkov radiation from the air shower forms a cone of blue visible light (light pool) around the primary gamma ray. Such flash of Cherenkov light lasts for about 10 ns. A typical size of a light pool on the ground is about 250 m in diameter with a density of ∼50 Cherenkov photons per m^2 for a 1 TeV gamma-ray primary. An optical telescope located inside the Cherenkov light cone will be able to detect it, if its dish is large enough for such low fluxes and its camera is fast for such short signals. An effective collecting area of a single Cherenkov telescope can be approximated by the area of the Cherenkov light pool on the ground ($\sim 5 \times 10^4$ m^2). This provides a remarkable advantage to IACTs comparing to the space gamma-ray telescopes. By means of the analysis of a signal detected with the IACT, it is possible to identify properties of the primary. The size and the brightness of obtained elliptical image corresponds to the energy of the initial gamma-ray photon[5], while its orientation allows us to reconstruct the direction of the primary or, in other words, the position of emitting source on the sky. A schematic view of the IACT technique is shown in Fig. 1.3.

Gamma rays are not the only particles, which produce air showers: a gamma-ray photon accounts for ∼10^4 cosmic-ray hadrons. Interacting with atoms and molecules of

[5] A high-energy gamma-ray photon produces more energetic and more extended shower comparing to the low-energy primary.

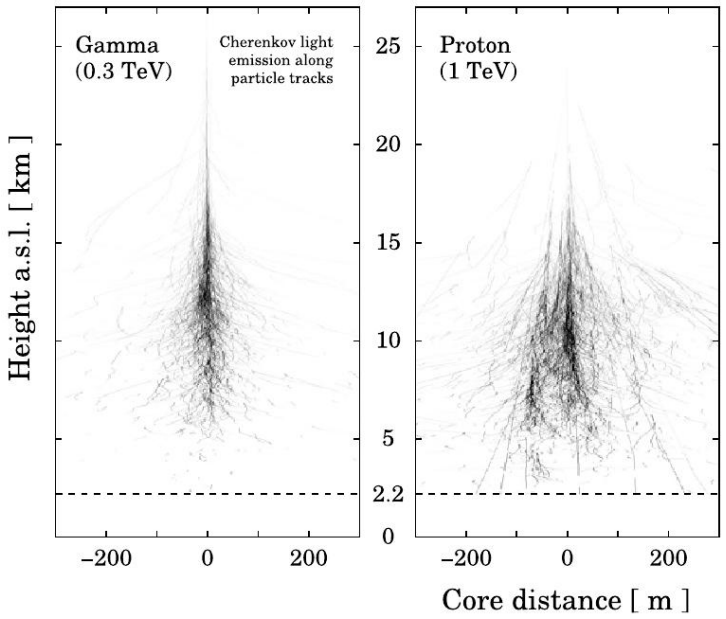

FIGURE 1.4: Simulated atmospheric showers for the 0.3 TeV gamma ray (on the left) and 1 TeV proton (on the right) as a primary particle. (Image adopted from [134]).

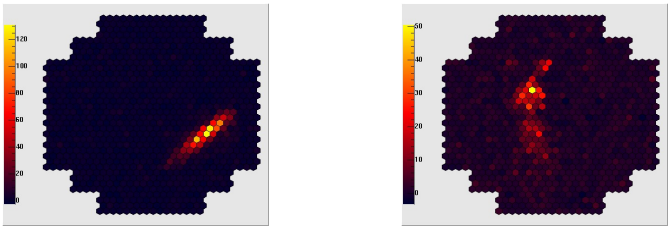

(A) (B)

FIGURE 1.5: Images of the IACT camera for the (A) gamma-ray and (B) hadronic events, taken from http://www.mpi-hd.mpg.de/hfm/HESS/.

the Earth's atmosphere, cosmic rays also produce energetic showers of pions, nuclei and products of their decays. The Cherenkov radiation from such hadronic shower detected with IACT is considered as a background event for VHE astrophysical studies. Showers originated from cosmic rays are much more extended than the electromagnetic ones, formed by gamma-ray primaries[6] (see Fig. 1.4). The differences between the structures of the gamma-ray and hadronic showers are imprinted on their images seen with Cherenkov telescopes. As shown in Fig. 1.5, an image of an electromagnetic shower has an elliptical shape, whereas that of an hadronic event – irregular. Analyzing obtained images of Cherenkov pools, we can discriminate signal events (gammas) from the background (hadrons) with ∼99% efficiency (see gamma-hadron separation method in [133]).

[6]Gamma-ray primary produces a shower consisted mainly of electrons and positrons.

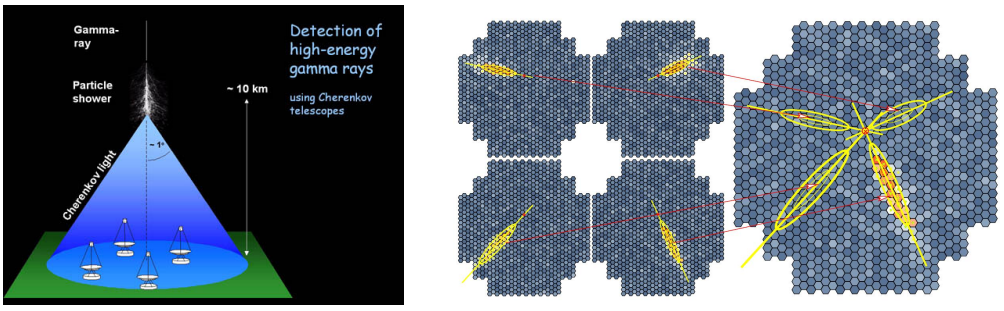

(A) (B)

FIGURE 1.6: (A) The schematic view of the stereoscopic IACTs observations (from http://www.mpi-hd.mpg.de/hfm/HESS/). (B) Images of four Cherenkov telescope cameras detected the same event and those projected into one camera plane (from [137]).

The energy threshold of Cherenkov telescopes is defined basically by a gamma-hadron separation efficiency. An image of an electromagnetic shower produced by a low-energy gamma ray (<100 GeV) is faint and it can be misinterpreted as a hadronic event with an irregular shape. Using IACTs with large mirrors, we can obtain images of a shower of a better quality. This leads to more efficient gamma-hadron discrimination and, therefore, to lower values of the energy threshold attainable with this telescope. The size of the largest currently operating Cherenkov telescope is 28 meters (the H.E.S.S. installation, for more details see Sect. 1.3.2). This instrument allows us to carry out observations down to 20 GeV.

Using several Cherenkov telescopes as a single gamma-ray instrument provides a number of advantages. Observing with a number of IACT-units spaced by a distance of ∼100 m can enlarge the collective area and increase the sensitivity of the whole instrument. In addition, analyzing multiple images of the same shower (stereoscopic observations, see Fig. 1.6) it is possible to improve the reconstruction of the primary gamma ray, i.e. to improve the determining of its energy and initial direction. This provides better angular and energy resolutions of a Cherenkov instrument (see e.g. [21, 135]). Stereoscopic observations also improve the gamma-hadron separation efficiency: e.g. by accepting only events, which simultaneously trigger all IACTs under the light pool [136].

1.3.2 The Status of Current IACTs

A great improvement of ground-based Cherenkov instruments was made since a detection of the first VHE gamma-ray source, the Crab Nebula, with the Whipple 10-meter IACT in 1989 [1]. Using the legacy and experience of the first-generation IACT projects (e.g. Whipple telescope, HEGRA [138], CAT [139], CANGAROO [140]), the currently operating Cherenkov telescopes such as MAGIC, VERITAS (successor of the Whipple

telescope) and H.E.S.S. (the HEGRA successor) have been developed. An order of magnitude improvement of the sensitivity was achieved with these instruments.

The MAGIC (Major Atmospheric Gamma Imaging Cherenkov Telescopes) instrument consists of two identical 17-meter Cherenkov telescopes spaced by 85 meters, which are situated at the Roque de los Muchachos Observatory (La Palma, Spain) [141]. The first telescope operates since 2004, the second unit joined in 2009. This IACT performs observations in the energy range from 50 GeV up to 30 TeV. VERITAS is the Very Energetic Radiation Imaging Telescope Array System of four 12-meter telescopes separated by a 100-meter distance, working at energies from 85 GeV to ∼50 TeV [142]. This facility is in operation in Mount Hopkins (Arizona, USA) since 2007. The High Energy Stereoscopic System (H.E.S.S.) was initially developed as an array of four 12-meter telescopes at a distance of ∼120 meters, observing the VHE gamma-ray sky in the 100 GeV – 100 TeV energy band since 2002 [143]. The second stage of the H.E.S.S. project started in 2013 after a construction and commissioning of the fifth large 28-meter telescope in the center of the array [144]. As mentioned above, this telescope enlarged the energy range of the H.E.S.S. instrument down to ∼20 GeV. In contrast to MAGIC and VERITAS, H.E.S.S. operates in the southern hemisphere (Khomas Highland, Namibia). Taking into account a large field of view of small H.E.S.S. telescopes (5°), this array can be considered as the best currently operating IACT machine for the Galactic Plane Survey [3]. A wide range of astrophysical objects – from pulsars to AGNs – is being investigated with these Cherenkov telescopes. In addition, a number of fundamental studies, like the DM/ALP searches and LIV tests, have been carried out with MAGIC, VERITAS and H.E.S.S. (see e.g. [145], [146, 147] and [148]). A large amount of important investigations, which expanded the frontier of our knowledge concerning the VHE sources, was already performed with the current generation of Cherenkov instruments (see Sect. 1.1). However, the potential of the IACT technique has not been fully realized yet.

1.3.3 Prospects for the Future Cherenkov Telescope Array Project

The Cherenkov Telescope Array[7] (CTA) is a modern project of the next-generation ground-based VHE gamma-ray facility, which aims to use all the advantages of the IACT technique [149, 150]. The CTA observatory will comprise two arrays, one in each hemisphere, with a large number of telescopes of 3 different types: Large Size Telescopes (LSTs, 23-meter diameter), Medium Size Telescopes (MSTs with diameters of 10–12 meters) and Small Size Telescopes (SSTs, 4-meter diameter). This will allow CTA to cover the full sky over the energy range from a few tens of GeV to more than 100

[7] https://portal.cta-observatory.org/Pages/Home.aspx

TeV and also to reach a 10 times better sensitivity and an improved angular resolution, compared to the present Cherenkov telescope installations.

There is a possibility of dividing the whole array into sub-arrays featuring different mirror sizes: LST-array, MST-array and SST-array consisting of only Large, Medium and Small Size Telescopes, respectively. These arrays are most sensitive in different parts of the CTA spectral range. A number of LSTs are responsible for the lower part of the CTA bandpass: from 20 to 200 GeV. The 23-meter dishes of these telescopes are able to detect faint Cherenkov light from low-energy showers produced by multiple-GeV photons[8]. Several dozens of MSTs, which will cover a 1 km^2 area, are designed to be most sensitive at 100 GeV – 10 TeV energies. A large number ($\sim$70) of SSTs will be spread over an area of 10 km^2 in order to provide an effective area and, therefore, a sensitivity level sufficiently high for the detection of rare energetic photons with energies from 5 up to 300 TeV.

The CTA sensitivity peaks at $\sim$5 TeV, reaching almost 1 mCrab level [151]. At low energies ($<$200 GeV), the performance of this IACT is limited by systematic uncertainties: Cherenkov events are faint and the gamma-hadron separation method is less effective. At energies above 10 TeV, the sensitivity is limited by low gamma-ray fluxes of observed sources. However, it should be noted that both the sensitivity and angular/energy resolution of CTA in the whole energy range (20 GeV – 300 TeV) will be much better that those of the currently operating IACTs. In addition, a 50-hour CTA observation at energies $>$20 GeV will be more sensitive than a 1-year *Fermi*-LAT exposure in the same energy range [150].

According to the preliminary Monte Carlo (MC) production 2 (Prod2) simulations[9], the northern CTA installation (CTA-North) will contain 4 LSTs and 15 MSTs, whereas the southern (CTA-South) – 4 LSTs, 25 MSTs and 72 SSTs (see Fig. 1.7). The CTA-South configuration can be possibly extended by 24 Schwarzschild-Couder Telescopes (SCTs). These units represent a class of medium size telescopes (10-meter diameter) with a dual-mirror optical design. CTA-South array is more extended than CTA-North, because the southern hemisphere observations will be focused on Galactic objects, including extended sources, which require a larger network of Cherenkov telescopes to be observed with better angular resolution, and also extremely energetic emitters of photons at energies $>$100 TeV (PeVatrons), which will be studied mainly with an array of SSTs. CTA-North is designed mainly for observations of point-like extragalactic objects, whose VHE emission is significantly attenuated above 10 TeV through interactions with the extragalactic background light.

[8] A flux of the Cherenkov light from an atmospheric shower on the ground is $\sim$1 photon/m^2 for the 20 GeV primary, $\sim$5 photon/m^2 for 100 GeV photon and $\sim$50 photon/m^2 for the 2 TeV gamma ray.

[9] https://portal.cta-observatory.org/Pages/CTA-Performance.aspx

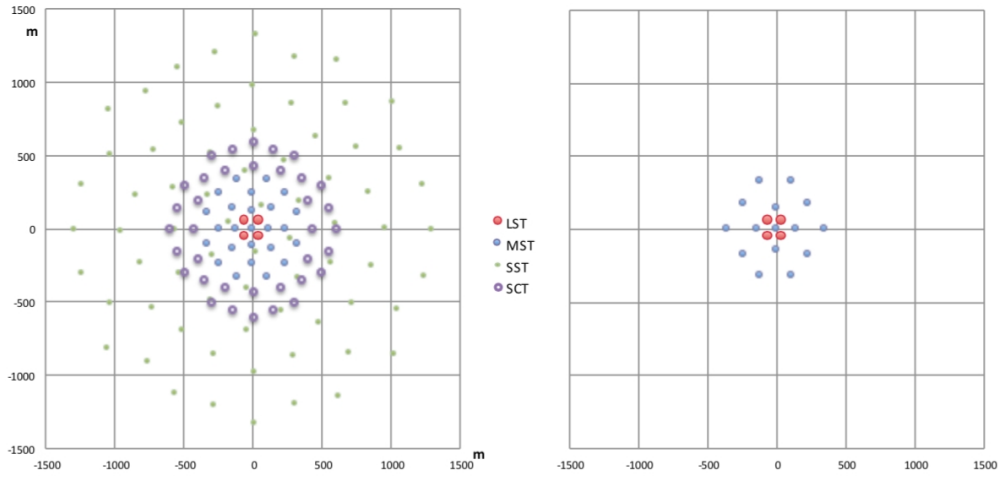

FIGURE 1.7: Layouts of the southern (on the left) and northern (on the right) CTA installations. CTA-South consist of 4 Large Size telescopes (LSTs, filled red circles), 25 Medium Size Telescopes (MSTs, filled blue circles), 72 Small Size Telescopes (SSTs, green dots), whereas CTA-North corresponds to the array of 4 LSTs and 15 MSTs. Schwarzschild-Couder medium size Telescopes (SCTs) are also shown in the left figure as 24 opened purple circles. x-, y- axes are in meters. (Credits: The CTA Consortium).

The main scientific objectives of the CTA Project are (i) to understand the origin and acceleration mechanism of relativistic cosmic-ray particles; (ii) to probe extreme environments and physical processes in close vicinity to compact objects (neutron stars, black holes) and also within relativistic jets/winds/shocks/outflows; (iii) to investigate questions of fundamental physics, such as the nature and distribution of DM, the quantum gravity effects on photon propagation (Lorentz invariance violation), the existence of axion-like particles [150]. The high sensitivity of CTA will allow us to perform more detailed analysis of already investigated sources and also to detect new objects of potentially unknown classes. For instance, CTA is expected to scan the whole Galaxy (up to 15 kpc) detecting distant SNRs [152]. Detailed morphological studies of extended sources (e.g. PWNe, SNRs, star-forming regions) will be possible due to high angular resolution of this IACT (about 1-3 arc minutes). Covering at least two decades in energy, CTA will perform both broadband studies and investigations at the high-/low-energy limit, such as a discovery of PeVatrons (at energies >100 TeV) and observations of gamma-ray bursts and active galactic nuclei (AGNs) at cosmological distances z=5 (at energies <100 GeV). The large field of view ($\sim 8^\circ$) of both the northern and southern installations makes CTA a powerful machine for both Galactic and Extragalactic Surveys. The energy resolution better than 10% makes the detailed spectral studies feasible with CTA (e.g. searches for the signatures of the DM annihilation [72]).

As a part of the CTA project, a dual-mirror end-to-end prototype of the Small Size Telescope (SST-2M) is under undergoing commissioning activities within the framework

of the ASTRI[10] flagship project of the Italian Ministry of Research and Education led by INAF [153]. The Schwarzschild-Couder optical solution [154] implemented for the ASTRI telescopes allows us to obtain a smaller plate scale, to reduce the size and the weight of the Cherenkov camera, and to adopt silicon photo-multipliers as light detectors. The first end-to-end prototype was recently inaugurated in Italy (Mount Etna, Sicily) [155]. In cooperation with the Universidade de Sao Paulo (Brazil) and the North-West University (South Africa), this project also foresees the construction of a mini-array of 9 ASTRI SST-2M units with a relative distance of about 300 m (ASTRI mini-array). The ASTRI mini-array possibly will be one of the precursors for the southern CTA installation [155]. This mini-array will perform early scientific investigations of prominent VHE sources[11] in the 5-100 TeV energy range. An improved sensitivity above 10 TeV with respect to the current IACTs, together with an angular resolution of few arc minutes and energy resolution of 10–15% will make the ASTRI mini-array a very promising facility for observations of bright known AGNs, PWNe, SNRs and also for scanning the Galactic center region at energies of hundreds of TeV [156].

1.4 This Thesis

Gamma-ray emission from isolated pulsars is not fully understood yet. Increasing the sample of detected neutron stars at VHE is necessary for a comprehensive study of such sources. At the same time, more detailed investigations of already known bright pulsars are also important for a deeper understanding of the nature of the emission from these sources.

In this Thesis, I investigated what type of studies can be carried out on gamma-ray pulsars with the next-generation CTA facility and with the ASTRI mini-array – a possible CTA precursor. I started with an analysis of the 12 most energetic pulsars, with significant pulsated emission at energies >25 GeV detected with the *Fermi*-LAT (Chapter 2). I estimated the fraction of these pulsars, that will be detectable with CTA, assuming a power-law VHE spectrum for each of them. For the well-studied bright gamma-ray pulsars, such as the Crab and Vela pulsars, I performed a more detailed analysis based on the recent results from IACTs (MAGIC, VERITAS, H.E.S.S.). In Chapter 3 I simulated the VHE gamma-ray pulse profiles of the Crab pulsar, obtained with different configurations of CTA and with the ASTRI mini-array, and then investigated, with which accuracy it will be possible to perform a VHE timing analysis of the Crab pulsar with these Cherenkov installations assuming different VHE spectral indexes. In Chapter 4, I

[10] Astrofisica con Specchi a Tecnologia Replicante Italiana (http://www.brera.inaf.it/astri/)
[11] with the flux of the order of $\sim 10^{-12}$ erg cm^{-2} s^{-1} at 10 TeV.

carried out detailed simulations of the Vela X region, assuming different spatial distributions for the diffuse Vela X emission at VHE. In this analysis I obtained more realistic estimates of the significance of the Vela pulsar detection with CTA (as compared to those from Chapter 2). In studying the morphology of the simulated Vela X emission, I tested also the resolving capabilities of CTA and the ASTRI mini-array. The general conclusions of the Thesis and a description of future work are reported in Chapter 5.

Chapter 2

Simulations of High Energy *Fermi* Pulsars Observations with the Cherenkov Telescope Array

Three years of *Fermi*-LAT operations yielded in the first high-energy catalog (1FHL, [95]), which contains 514 sources with significant emission at energies >10 GeV. The location, spectrum, a variability measure and associations with sources in catalogs at other wavelengths are presented in the 1FHL catalog for each of these objects. The catalog contains 12 pulsars identified at high energies (HE *Fermi* pulsars) with significant pulsed emission above 25 GeV [see 95, Tables 9, 11]. They are: PSRs J0007+7303, J0534+2201 (Crab), J0614−3329, J0633+1746 (Geminga), J0835−4510 (Vela), J1028−5819, J1048−5832, J1413−6205, J1809−2332, J1836+5925, J2021+3651 and J2229+6114. These pulsars are the best candidates for VHE investigations that can be performed with currently operating and future ground based Cherenkov facilities.

In order to investigate whether these 12 pulsars can be detected with CTA, I perform a spectral analysis of the *Fermi*-LAT data for all objects, simulate VHE observations extrapolating their *Fermi* spectra, and estimate their detection significances.

2.1 Gamma-ray Investigations of HE *Fermi* Pulsars

The *Fermi*-LAT data of these pulsars are investigated in detail. Phase-averaged spectral analyses were performed for PSRs J0614−3329 [157], J0633+1746 [158], J1028−5819 [159], J1048−5832 [160] and J2229+6114 [160]. An analogous algorithm with background/PWN subtraction was implemented for PSRs J0534+2201 [10, 12] and J0835−4510

(see [161] and [162] for the full energy range and >50 GeV analyses, respectively). Analyses of the on-peak and off-peak emission were performed for PSRs J0007+7303 [163], J1413−6205 [164], J1836+5925 [165] and J2021+3651 [166]. All 12 HE *Fermi* pulsars are included in the Second *Fermi*-LAT source catalog (2FGL, phase-averaged analysis in [167]) and in the Second Catalog of Gamma-ray Pulsars (2PC, phase-averaged analysis in [87]). The high-energy (>10 GeV) phase-averaged spectral parameters of all these pulsars are reported in the 1FHL catalog.

When studying the high-energy emission from pulsars it is important to account for the off-peak (OP) emission from the surrounding nebula and the pulsar itself. The emission form the Crab Nebula in the *Fermi*-LAT energy range can be modeled as a sum of two power laws [10] or as a sum of a power-law and a smoothly broken power-law component [12]. Abdo et al. [168] fitted the *Fermi*-LAT data corresponding to the PWN around the Vela pulsar (PSR J0835−4510) with a power-law. A more detailed analysis of the Vela X region [169] shows that a broken power law describes its gamma-ray spectrum better than a simple power law. Some pulsars, such as PSRs J0007+7303 and J1413−6205, show prominent OP point source emission at gamma rays [see 163, 164]. The spectra of these OP components can be modeled with a power law (for PSR J0007+7303) and a power law with an exponential cut-off (for PSR J1413−6205). A spectral analysis of the off-peak emission performed within the framework of 2PC confirmed significant OP emission for PSRs J0007+7303, J0534+2201, J0633+1746, J0835−4510, J1809−2332 and J1836+5925. Although such emission is usually associated with the presence of the PWN, in some cases it can correspond to the own pulsar emission, also called "second interpeak" (e.g. for PSRs J0633+1746 [158] and J1836+5925 [165]).

HE *Fermi* pulsars are the most suitable candidates for VHE observations. Some of them have been already investigated by currently operating IACTs. Recent VERITAS observations [170] discovered TeV emission from the supernova remnant CTA1, which is situated near PSR J0007+7303 (5′ apart) and associated with the TeV emission from the corresponding PWN. The VHE emission from the Crab pulsar has been investigated with the MAGIC and VERITAS telescopes [96, 97, 99, 118]. The Crab Nebula was observed with MAGIC [9], VERITAS [19] and H.E.S.S. [21]. The VHE timing analysis and the prospects for the CTA detection of the Crab pulsar are presented in [171] and [120], respectively. No significant pulsed emission from PSR J0633+1746 was observed with MAGIC[1] above 50 GeV and with VERITAS [172] above 100 GeV. The VHE pulsations of the Vela pulsar was detected at 10–100 GeV by CT5, the 28-meter telescope of the H.E.S.S. instrument[2]. The Vela X region was also investigated by H.E.S.S. Collaboration

[1] http://www.cbpf.br/~icrc2013/papers/icrc2013-0691.pdf
[2] http://www.mpg.de/8287998/velar-pulsar

in the 0.75–70 TeV energy range [25]. PSR J2021+3651 can be one of the possible contributors to the VHE emission from the bright extended source MGRO J2019+37, which was observed with VERITAS [45]. Residual VHE emission was seen with VERITAS at the position of PSR J2229+6114 during an observation of G106.3+2.7 [173].

2.2 Spectral Analysis of the *Fermi*-LAT Data

I analyze the data of 12 HE *Fermi* pulsars acquired during more than 5 years of the *Fermi*-LAT regular sky survey. The data reduction and the spectral fit are performed using the *Fermi* Science software package[3]. Using the tool `gtselect` I extract events within the time interval shown in Table 2.1 and from a region of interest (ROI) of 14° centered on the position of the pulsar (see Table 2.1). In this analysis the emission from 100 MeV up to 100 GeV is considered. I used the tool `gtmktime` to extract good quality data (`DATA_QUAL==1`), with the instrumental configuration flag set to 1 (`LAT_CONFIG==1`), with a rocking angle <52° and zenith angle <100°. In order to account for the dependence of the instrument response function (IRF) of the instrument on the off-axis angle, I calculated effective livetime cubes[4] with the tool `gtltcube`, whereas exposure maps were created with `gtexpcube2`.

In order to model the gamma-ray spectra I use the binned likelihood analysis tool `gtlike`. The IRF is "P7REP_SOURCE_V15"[5]. Each spectrum is fitted with a model consisting of background emission and a number of sources. The background component represents both Galactic (*gll_iem_v05_rev1*) and isotropic diffuse emission (*iso_source_v05*)[6]. The latter sums up the contribution of the extragalactic and instrumental backgrounds. The normalization of both background components is kept as a free parameter. In addition, I include spectra of all point and non-background diffuse sources within a radius ROI+5° (19°) from 2FGL and with a value of Test Statistic[7] (TS) ≥25. The gamma-ray spectra of these objects can be in general described by one of the following models:

1. power-law model:

$$\frac{\mathrm{d}N}{\mathrm{d}E} = N_0 \left(\frac{E}{E_0}\right)^{-\gamma}, \tag{2.1}$$

[3] http://fermi.gsfc.nasa.gov/ssc/data/analysis/software/

[4] Livetime cube is a product of the tool `gtltcube`, which calculates how long the source was observed at different inclination angles (off-axis angles) over the observation.

[5] http://fermi.gsfc.nasa.gov/ssc/data/analysis/LAT_caveats_p7rep.html

[6] http://fermi.gsfc.nasa.gov/ssc/data/access/lat/BackgroundModels.html

[7] Test Statistic is defined as TS $= -2\ln(L_0/L_1)$, where L_0 is the maximum likelihood value for a model without an additional source and L_1 is the maximum likelihood value for a model with the additional source at a specified location. As a basic rule of thumb, the square root of the TS is approximately equal to the detection significance for a given source (from http://fermi.gsfc.nasa.gov/ssc/data/analysis/documentation/Cicerone/Cicerone_Likelihood/Likelihood_overview.html).

2. power-law model with exponential cut-off (PLEC):

$$\frac{\mathrm{d}N}{\mathrm{d}E} = N_0 \left(\frac{E}{E_0}\right)^{-\gamma} \exp\left[-\left(\frac{E}{E_c}\right)^{b}\right], \tag{2.2}$$

3. log-parabola model:

$$\frac{\mathrm{d}N}{\mathrm{d}E} = N_0 \left(\frac{E}{E_b}\right)^{-\alpha+\beta\log(E/E_b)}, \tag{2.3}$$

4. smoothly broken power-law model:

$$\frac{\mathrm{d}N}{\mathrm{d}E} = N_0 \left(\frac{E}{E_0}\right)^{\gamma_1} \left[1+\left(\frac{E}{E_b}\right)^{(\gamma_1-\gamma_2)/\beta_1}\right]^{-\beta_1}, \tag{2.4}$$

where N_0 is the normalization factor, α, β, γ, γ_1 and γ_2 are spectral indexes, E_c is a cut-off energy, E_0 and E_b are reference energies and β_1 is a parameter. In this analysis I fix $b = 1$.

The following spectral parameters of objects inside the ROI are left free to vary during the fit:

- for the power-law model (Eq. (2.1)): normalization N_0 and spectral index γ,
- for the PLEC model (Eq. (2.2)): normalization N_0, spectral index γ and cut-off energy E_c,
- for the log-parabola model (Eq. (2.3)): normalization N_0 and spectral indexes α and β,
- for the smoothly broken power law model (Eq. (2.4)): all parameters except β_1.

Sources outside the ROI are taken into account due to the relatively large point spread function (PSF) of the *Fermi*-LAT at low energies ($\sim$10° at 100 MeV for the 95% containment radius[8]) which causes an additional contribution to the considered field of view. In performing the fit all spectral parameters of sources at a radius >8° are fixed [87][9].

2.2.1 Folded Light Curves

Pulsars have on- and off- pulse intervals and, in some cases, a bridge interval in phase. The former can be characterized by one (a few) prominent and sharp peak(s) emission.

[8] http://www.slac.stanford.edu/exp/glast/groups/canda/archive/p7rep_v15/lat_Performance.htm

[9] Except for the off-pulse analysis of PSR J0835−4510 and the on-pulse analysis of PSR J0614−3329 (for further details see Sect. 2.2.2).

The average level of the bridge emission (if present) between the two peaks is higher than that of the off-pulse phase interval. The off-pulse emission is dominated by the background, which includes the OP emission from the pulsar and its nebula (if present).

I folded the light curves of each pulsar (Fig. 2.1) using the TEMPO2 software package [174] and ephemerides [175] valid within the epochs reported in Table 2.1. I define the on- and off- pulse phase intervals of all profiles (Table 2.1), using the Bayesian Block and Knuth's rule algorithms [176, 177]. For all HE *Fermi* pulsars – except PSRs J0007+7303, J0835−4510 and J2229+6114 – I find the bridge emission (see Fig. 2.1). On the other hand, PSRs J0007+7303 and J2229+6114 (Figs. 2.1A, 2.1L) appear to have two closely spaced peaks or only one peak, respectively [160, 163]. Since PSR J0835−4510 has a more complex pulse shape with 3 peaks and bridge emission overlapping with each other [161], a single on-pulse interval comprising all peaks and any possible bridge emission is considered (Fig. 2.1E). It should be noticed that for PSR J1836+5925 only one event is detected at energies >25 GeV (Fig. 2.1J). Following Ackermann et al. [95], this event is considered significant. For this reason I include this pulsar in the present analysis.

TABLE 2.1: Pulsars with emission at energies >25 GeV detected with the *Fermi*-LAT investigated in this work. Galactic coordinates (l, b) of each pulsar are shown in the second and third columns [95]. Data are taken from the *Fermi*-LAT sky survey observations performed within the time intervals in modified Julian days (MJD) listed in the fourth column. On-/off- pulse phase intervals for the full energy range from 100 MeV to 100 GeV ($\Delta\phi_{\rm on}/\Delta\phi_{\rm off}$) and above 10 GeV ($\Delta\phi_{\rm on}^{\rm HE}$) are also reported. P1 and P2 (if present) correspond to the first and second peaks, respectively (see text for details).

Pulsar	l (deg)	b (deg)	Time interval of ephemerids (MJD)	$\Delta\phi_{\rm on}$ P1	$\Delta\phi_{\rm on}$ P2	$\Delta\phi_{\rm off}$	$\Delta\phi_{\rm on}^{\rm HE}$ P1	$\Delta\phi_{\rm on}^{\rm HE}$ P2
J0007+7303	119.7	10.5	54686–56583	[0.0;0.5]	-	[0.5;1.0]	[0.09;0.41]	-
J0534+2201	184.6	-5.8	54686–56583	[-0.14;0.092]	[0.23;0.55]	[0.55;0.86]	[-0.014;0.013]	[0.34;0.417]
J0614−3329	240.5	-21.8	54696–56572	[0.035;0.26]	[0.57;0.863]	[0.26;0.57]	[0.076;0.12]	[0.636;0.747]
J0633+1746	195.1	4.3	54689–56579	[-0.037;0.19]	[0.5;0.7]	[0.7;0.963]	[0.034;0.134]	[0.516;0.675]
J0835−4510	263.6	-2.8	54686–56583	[0.07:0.7]	-	[0.7;1.07]	[0.106;0.6]	-
J1028−5819	285.1	-0.5	54686–56583	[0.12;0.28]	[0.536;0.76]	[0.76;1.12]	[0.189;0.229]	[0.65;0.688]
J1048−5832	287.4	0.6	54686–56583	[0.07;0.172]	[0.47;0.6]	[0.6;1.07]	[0.067;0.18]	[0.5;0.57]
J1413−6205	312.4	-0.7	54689–56579	[0.1;0.241]	[0.48;0.7]	[0.7;1.1]	[0.14;0.28]	[0.42;0.56]
J1809−2332	7.4	-2.0	54689–56579	[-0.04;0.182]	[0.31;0.49]	[0.49;0.96]	[0.06;0.135]	[0.37;0.455]
J1836+5925	88.9	25.0	54689–56579	[-0.06;0.22]	[0.48;0.7]	[0.7;0.94]	[0.018;0.197]	[0.55;0.73]
J2021+3651	75.2	0.1	54686–56583	[0.0;0.183]	[0.48;0.64]	[0.64;1.0]	[0.076;0.11]	[0.51;0.59]
J2229+6114	106.7	3.0	54686–56583	[0.16;0.612]	-	[0.612;1.16]	[0.27;0.52]	-

2.2.2 On-pulse and Off-pulse Spectral Analysis >100 MeV

I perform separate spectral fits of the on- and off- pulse intervals to achieve a better background subtraction. A treatment of the OP emission is included following the method described in [113]. The off-pulse spectrum is fitted with a different model in which the pulsar component is replaced by a OP component (assumed to be a point source). For all pulsars except the Crab and Vela pulsars I check for the presence of the exponential cut-off in the OPs spectra. Performing two fits, one with a power law[10] and the other with a PLEC[11] model, I obtain TS values of the OP emission in both cases (TS_{pwl} and TS_{PLEC}). If $TS_{cut} \equiv TS_{PLEC} - TS_{pwl} \geq 9$ the PLEC model was used for the OP component in the following analysis. Otherwise a power law was accepted. For the Crab pulsar, the OP emission represents the Crab Nebula, whose spectrum is well known. I assume the sum of a synchrotron (power law) and an inverse Compton (smoothly broken power law) component with free normalization factors (from [12]). For the Vela pulsar, the OP represents emission from the Vela X PWN. I use a disk spatial template from 2FGL and a power-law model with free normalization parameter and spectral index. In order to reach convergence in the particular case of the Vela X fitting, I fixed the spectral parameters of all sources outside 9°. In case the Galactic, extragalactic and/or OP components are significant in the off-pulse spectral fit ($\geq 3\sigma$-significance or TS$\geq$9), I include them in the on-pulse spectral analysis, renormalizing their spectra according to the ratio ($\Delta\phi_{on}/\Delta\phi_{off}$) of the on/off-pulse phase intervals (see Table 2.1) and fixing their spectral parameters.

In case of non-significant detection of these components, the background is included in the fit of the on-pulse emission with free normalization parameters, while the OP contribution is not considered.

After dealing with the background and OP emission as described above, I fitted the on-pulse emission from the central pulsar using the PLEC model (Eq. (2.2)) and obtained the spectral parameters shown in Table 2.2. As mentioned above, the spectral parameters of all sources outside 8° are fixed. However, in order to achieve convergence, for PSR J0614−3329 I fixed parameters of all sources outside 7°. Results are shown in Figs. 2.2, 2.3 and 2.4, where the best fit spectra are also compared with those presented in the literature an in *Fermi* catalogs (2FGL, 2PC).

I also obtained the spectral energy distribution of HE *Fermi* pulsars and corresponding OPs, dividing the energy range from 100 MeV to 100 GeV into eight energy bins (see dots in Figs. 2.2-2.7). For each energy bin I select events with the tool `gtselect` and calculate livetime cubes and exposure maps using the tools `gtltcube` and `gtexpcube2`,

[10] N_0 and γ are considered as free parameters.
[11] N_0, γ and E_c are considered as free parameters, $b = 1$.

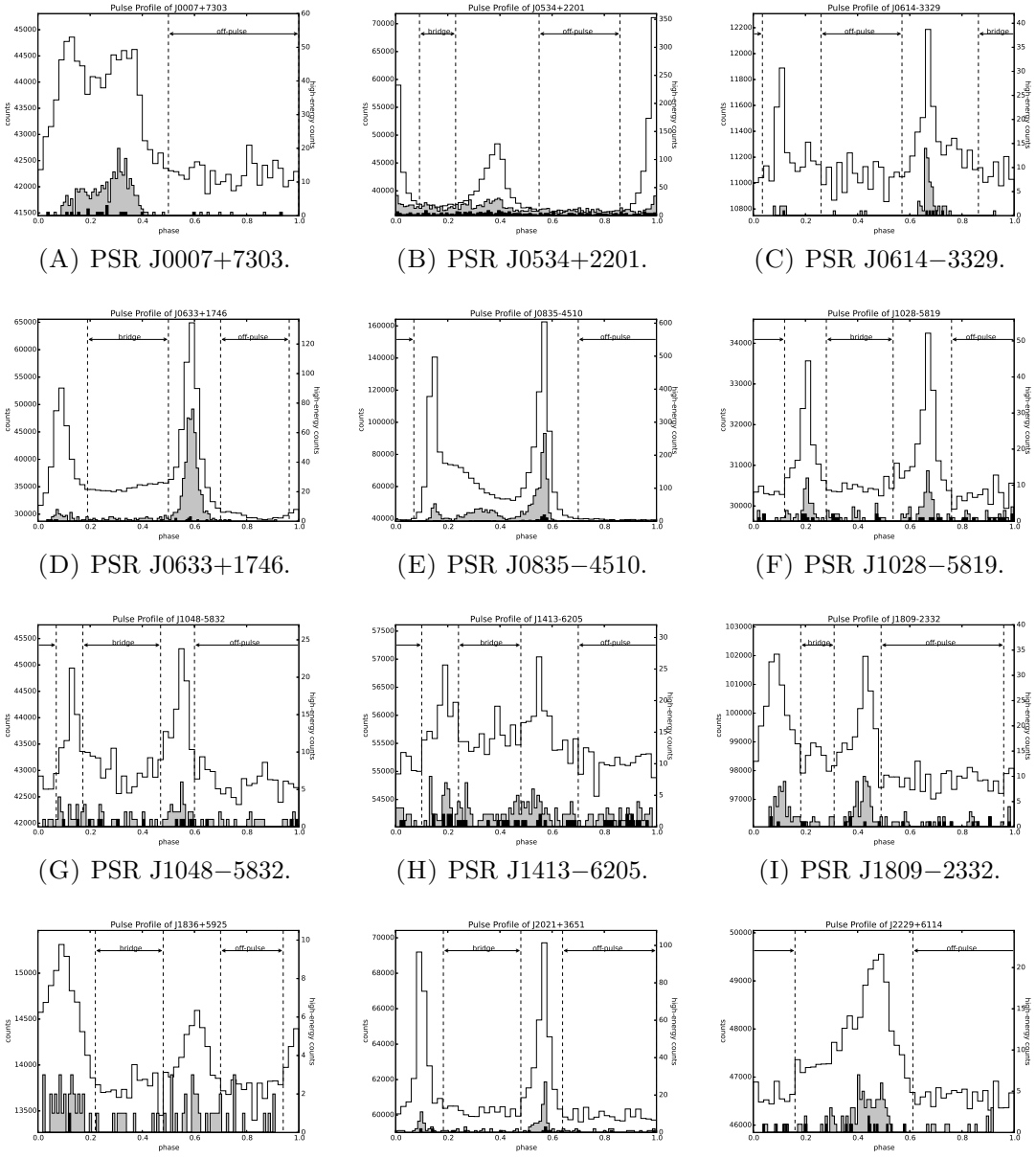

(A) PSR J0007+7303. (B) PSR J0534+2201. (C) PSR J0614−3329.

(D) PSR J0633+1746. (E) PSR J0835−4510. (F) PSR J1028−5819.

(G) PSR J1048−5832. (H) PSR J1413−6205. (I) PSR J1809−2332.

(J) PSR J1836+5925. (K) PSR J2021+3651. (L) PSR J2229+6114.

FIGURE 2.1: Pulse profiles of 12 pulsars with >25 GeV emission, obtained folding more than 5 years of the *Fermi*-LAT data. White (y-axis on the left), grey (y-axis on the right) and black (y-axis on the right) light curves correspond to events with energies >100 MeV, >10 GeV and >25 GeV, respectively. Counts at energies >100 MeV (>10 GeV/25 GeV) are extracted from a ROI of 14° (0.6°). Vertical dashed lines mark the on-pulse, off-pulse and bridge phase intervals in the energy range from 100 MeV to 100 GeV (see Table 2.1).

respectively. In order to obtain the flux of the pulsar in each energy bin, I fit the data with the `gtlike` tool using a power-law model with free normalization factor and fixed spectral index ($\gamma = 2.0$)[12]. The parameters of all other sources are also fixed. If TS_i of the i-th bin is <9, I determine an upper limit to the pulsar flux in that bin.

2.2.3 High Energy (>10 GeV) Spectral Analysis

The typical spectra of pulsars show a steep decline above 1 GeV (cut-off energy). Conventionally it is described by adding an exponential cut-off to the power-law model (PLEC in Eq. (2.2)). However, some pulsars appear to have a less steeper decline in the GeV energy range, than it is predicted by the PLEC model. In order to estimate it, PLEC fits with both fixed and free b-parameter were used in 2PC. As shown by Abdo et al. [87], a PLEC model with a shallower spectrum ($b < 1$) is statistically acceptable for a number of HE *Fermi* pulsars, such as PSRs J0534+2201, J0614−3329, J0633+1746, J0835−4510, J1028−5819, J1048−5832, J1809−2332, J1836+5925, J2021+3651 and J2229+6114.

With the aim of achieving a more accurate characterization of the high-energy part of the pulsars spectra, in this work I perform a spectral fit of the *Fermi*-LAT data above 10 GeV using a power-law model (Eq. (2.1)). Such an analysis is made using the method presented in Sect. 2.2.2 with a different ROI of 2°. With this value both an adequate coverage of the whole *Fermi*-LAT PSF (0.5° at 10 GeV for the 95% containment radius[13]) and a proper treatment of the background diffuse emission are achieved [95]. Since the peaks of the pulsars light curves become sharper with increasing energy (see Fig. 2.1), I re-define the values of the on-/off- phase intervals ($\Delta\phi_{\rm on}^{\rm HE}$) by applying the same Bayesian Block and Knuth's rule algorithms to the pulsars light curves at energies >10 GeV (see Table 2.1). However, to reach convergence for the Vela pulsar (PSR J0835−4510), I still use the value of $\Delta\phi_{\rm on}$, determined from the full energy range. Since the on-pulse phase interval for this pulsar does not have bridge emission, using $\Delta\phi_{\rm on}$ instead of $\Delta\phi_{\rm on}^{\rm HE}$ will not result in overestimating the value of the flux. The spectral model includes the target pulsar, which is described by a power-law spectrum, background components (*gll_iem_v05_rev1*, *iso_source_v05*) and other point-like/diffuse sources from 2FGL within the radius of 7° with TS>25. All parameters of out-of-ROI sources are fixed. I use a simple power-law model to describe high-energy (>10 GeV) OP emission in all pulsars. Off-/on- pulse analyses and background/OP subtraction are also performed (as in Sect. 2.2.2).

[12] Different slopes and spectral shapes have a small influence on the resulting value of the flux in such narrow energy bins

[13] `http://www.slac.stanford.edu/exp/glast/groups/canda/archive/p7rep_v15/lat_Performance.htm`

Resulting parameters of the high-energy analyses (off- and on- pulses) are presented in Table 2.2. In Figs. 2.2, 2.3 and 2.4 the best fitting high-energy spectra are compared with those from 1FHL.

In order to include the contribution of the Galactic diffuse background (GDB) into the VHE simulations, I also perform an additional spectral fit of the off-pulse *Fermi*-LAT data above 10 GeV, fixing all components with spectral values resulting from the high-energy off-pulse analysis described above and replacing the "standard" *Fermi* Galactic background (*gll_iem_v05_rev1*) with a model consisting of a uniform spatial distribution and a power-law spectrum[14]. GDB background spectra are shown in Table 2.3 (column 4).

2.3 Simulation of CTA Observations

I extrapolated high-energy (>10 GeV) spectral fits of 12 HE *Fermi* pulsars obtained in Sect. 2.2 up to ∼160 TeV and then simulated observations of these sources with CTA using the *ctools* software package [178] (tool `ctobssim`). Because of the different position on the sky, pulsars will culminate at different zenith angles during the observations with northern and southern CTA installations. Some pulsars, like PSRs J0007+7303, J0534+2201, J0633+1746, J1836+5925, J2021+3651 and J2229+6114, will be better observable from the northern hemisphere, i.e. with CTA-North, while the others (PSRs J0614−3329, J0835−4510, J1028−5819, J1048−5832, J1413−6205 and J1809−2332) with the southern installation CTA-South. I take into account for this by using CTA-North and CTA-South Monte Carlo Production 2 (MC-Prod2) configurations[15] in these simulations. As mentioned in Sect. 1.3.3, the CTA-South array is expected to consist of 4 large-size telescopes (LSTs, 24-meter diameter), 24 medium-size telescopes (MSTs, 12-meter dish) and 72 small-size telescopes (SSTs, 4-meter diameter), whereas CTA-North – of 4 LSTs and 15 MSTs. IRFs of these configurations and spectra of an isotropic background of charged cosmic-ray particles are derived from 50-hour simulated observations of a standard point source with 1 Crab Unit flux[16], at a 20° zenith angle, located at the center of the field of view.

Simulations are performed with a ROI of 3°, centered on the pulsar position. The input spectral model to be simulated consists of the extrapolated pulsar spectrum and the isotropic background of CTA. In case of significant OP detection during the high-energy off-pulse *Fermi*-analysis (see column 4 in Table 2.2), I add the corresponding

[14] Normalization factor N_0 and spectral index γ of the GDB are left free to vary.

[15] Public available files "CTA-Performance-South-20150511" and "CTA-Performance-North-20150511" on https://portal.cta-observatory.org/Pages/CTA-Performance.aspx

[16] 1 Crab Unit (C. U.) $= 2.79 \times 10^{-11} \times (E/1\ \mathrm{TeV})^{-2.57}\ \mathrm{cm}^{-2}\ \mathrm{s}^{-1}\ \mathrm{TeV}^{-1}$

extrapolated component into the VHE model, re-normalized to the total phase interval. I also account for the GDB. Since pulsars are point-like sources and the angular resolution of CTA above 40 GeV ($\sim$0.2°) is on the scale of the *Fermi*-LAT PSF ($\sim$0.5°) at 10 GeV, the spatial distribution of the GDB can be approximated as uniform. I extrapolate the GDB spectrum obtained in Sect. 2.2 up to 160 TeV, assuming a power-law model.

I simulate observations with a duration of 25 hours for the brightest pulsars J0534+2201 and J0835−4510 (the Crab and Vela pulsars), whereas for the others a 50-hour exposure time is used. $3° \times 3°$ count maps of all HE *Fermi* pulsars are shown in Figs. 2.8, 2.9 and 2.10.

Using the same extrapolated pulsars spectra, I carry out analogous simulations with reduced background/OP contamination, as if the sole data from the on-pulse phase intervals were considered for the analysis. For this, the background/OP contribution is renormalized to the high-energy on-pulse phase interval ($\Delta\phi_{\rm on}^{\rm HE}$).

I fit simulated data and estimate the significance S of pulsars detection in three energy bins (>0.04, >0.25 and >1 TeV) using the tool `ctlike`, which performs the unbinned maximum likelihood analysis. The simulated event list resulting from `ctobssim` together with an input spectral model are used. The square root of the output parameter TS roughly corresponds to the detection significance in Gaussian sigmas. In this analysis, the source is considered to be significantly detected, if $S \equiv \sqrt{TS} \geq 5$.

Uncertainties on the significance S for each pulsar are estimated in the following way, propagating the uncertainties on the high-energy power-law spectrum (Eq. (2.1)). Using the covariance matrix obtained in the *Fermi* likelihood analysis, an optimistic/pessimistic spectrum ($F_{\rm opt}/F_{\rm pes}$) can be obtained from the following expression:

$$F_{\rm opt,pes} = F(E) \pm \sqrt{\left(\frac{\partial F}{\partial N_0}\right)^2 \sigma_{N_0}^2 + \left(\frac{\partial F}{\partial \gamma}\right)^2 \sigma_\gamma^2 + 2\frac{\partial F}{\partial N_0}\frac{\partial F}{\partial \gamma}\sigma_{N_0\gamma}}\,. \tag{2.5}$$

In Eq. (2.5) $\partial F/\partial N_0$ and $\partial F/\partial\gamma$ correspond to the partial derivatives of F with respect to N_0 and γ, respectively. $\sigma_{N_0}^2$, σ_γ^2 and $\sigma_{N_0\gamma}$ are diagonal and non-diagonal elements of the corresponding covariance matrix, respectively.

I repeat VHE simulations for all pulsars with $F_{\rm opt}$ and $F_{\rm pes}$ spectra obtaining the range of significances, which are reported in Table 2.4.

2.4 Results

2.4.1 Analysis at 100 MeV – 100 GeV

In Figs. 2.2, 2.3 and 2.4 I compare the best fit spectra in the 100 MeV – 100 GeV energy range with those presented in the literature (see references in Table 2.2, 2FGL, 2PC). Some spectra differ from those reported in the literature because of the different data sets and analysis methods (e.g. phase averaged, phase resolved) adopted in the corresponding analyses (see e.g. solid/dashed black spectra of PSR J1836+5925 in Fig. 2.4B obtained with/without taking into account for the OP emission). In general, our results are consistent with the previous ones. All pulsars spectra used for the comparison correspond to the PLEC model with the parameter b equaled to 1. Only in [12] this parameter was varied.

TS_{cut} values, which give a measure of the significance of the exponential cut-off in OPs spectra, are shown in Table 2.2 (column 2). Spectral fits of the OP emission from PSRs J1413−6205 and J2229+6114 with the PLEC model did not converge. Therefore, for them I use a simple power law instead. The corresponding values of TS_{pwl} are listed in Table 2.2. The off-pulse spectral fit of PSR J2021+3651 did not converge with either the power-law or the PLEC models. I conclude that the OP emission from this pulsar is not significant. Table 2.2 also shows the significances of the Crab Nebula (TS_{Sync} and TS_{IC}) and Vela X (TS_X) spectral components.

The results of the OP spectral fits are shown in Table 2.3 (column 2, where all spectra are renormalized according to the total phase interval). There are significant exponential cut-off tails in PSRs J0007+7303, J0633−1746, J1028−5819 and J1836+5925. Figs. 2.5, 2.6 and 2.7 show the best fitting OP spectra together with those from the literature (references in Table 2.3, 2PC). It should me mentioned that different models were used in the past to describe the emission from the Vela X region (an ellipsoidal spatial template with a smoothly broken power-law spectral model [169]), of the OP in PSRs J0007+7303 (power-law, 2PC and [163]) and J1809−2332 (PLEC, 2PC).

2.4.2 High-energy Analysis Above 10 GeV

I also performed a spectral analysis of 12 HE *Fermi* pulsars at energies >10 GeV. Best fitting parameters of the off- and on- pulse analyses are reported in Table 2.2 (columns 4,5). All pulsars show significant emission in this energy range. OP emission was detected with $>3\sigma$-significance ($TS \gtrsim 9$) in PSRs J0534+2201, J0835−4510 and J1836+5925. Their spectra renormalized to the total phase interval are shown in Table

TABLE 2.2: Results of the spectral fits at energies >100 MeV and >10 GeV of our sample of high-energy *Fermi* pulsars. Best fit spectral parameters for the full energy range (100 MeV – 100 GeV) are reported in the third column. The second column contains the significances of the OP components from the off-pulse spectral fits above 100 MeV (see text for more details), while the fourth column those of the from the high-energy off-pulse spectral fits above 10 GeV. Best fitting parameters of the power-law spectra at energies >10 GeV are in the fifth column. References to previous spectral analyses are reported in the first column.

Pulsar	Spectral analysis >100 MeV[a]		Spectral analysis >10 GeV[b]	
	off-pulse	on-pulse	off-pulse	on-pulse
J0007+7303 [163]	$TS_{cut} = 11$	$N_0 = 0.748 \pm 0.009$ $\gamma = 1.36 \pm 0.01$ $E_c = 4.6 \pm 0.1$	-	$N_0^{HE} = 2.5 \pm 0.2$ $\gamma = 4.03 \pm 0.19$
J0534+2201[c] (Crab) [10],[12]	$TS_{Sync} = 5688$ $TS_{IC} = 6540$	$N_0 = 2.47 \pm 0.03$ $\gamma = 1.905 \pm 0.007$ $E_c = 4.44 \pm 0.14$	TS(Crab Nebula) = 5180	$N_0^{HE} = 3.0 \pm 0.3$ $\gamma = 3.0 \pm 0.2$
J0614−3329 [157]	$TS_{cut} = 7.5$	$N_0 = 0.156 \pm 0.005$ $\gamma = 1.24 \pm 0.04$ $E_c = 4.4 \pm 0.3$	-	$N_0^{HE} = 0.85 \pm 0.14$ $\gamma = 3.4 \pm 0.3$
J0633+1746 (Geminga) [158]	$TS_{cut} = 1739$	$N_0 = 7.27 \pm 0.04$ $\gamma = 1.201 \pm 0.005$ $E_c = 2.62 \pm 0.02$	-	$N_0^{HE} = 3.6 \pm 0.4$ $\gamma = 5.2 \pm 0.2$
J0835−4510[d] (Vela) [161],[162]	$TS_X = 3360$	$N_0 = 22.87 \pm 0.07$ $\gamma = 1.498 \pm 0.002$ $E_c = 2.99 \pm 0.02$	TS(Vela X) = 15	$N_0^{HE} = 18.4 \pm 0.8$ $\gamma = 4.38 \pm 0.08$
J1028−5819 [159]	$TS_{cut} = 31$	$N_0 = 0.45 \pm 0.01$ $\gamma = 1.59 \pm 0.03$ $E_c = 3.9 \pm 0.3$	-	$N_0^{HE} = 0.69 \pm 0.15$ $\gamma = 3.8 \pm 0.4$
J1048−5832 [160]	$TS_{cut} = 2.3$	$N_0 = 0.34 \pm 0.01$ $\gamma = 1.55 \pm 0.03$ $E_c = 2.97 \pm 0.15$	-	$N_0^{HE} = 0.3 \pm 0.1$ $\gamma = 4.0 \pm 0.8$
J1413−6205 [164]	$TS_{pwl} = 33$	$N_0 = 0.26 \pm 0.01$ $\gamma = 1.67 \pm 0.05$ $E_c = 4.4 \pm 0.5$	-	$N_0^{HE} = 0.5 \pm 0.1$ $\gamma = 3.9 \pm 0.6$
J1809−2332	$TS_{cut} = 0.5$	$N_0 = 0.90 \pm 0.02$ $\gamma = 1.55 \pm 0.02$ $E_c = 3.4 \pm 0.1$	-	$N_0^{HE} = 0.77 \pm 0.17$ $\gamma = 4.6 \pm 0.4$
J1836+5925 [165]	$TS_{cut} = 576$	$N_0 = 0.58 \pm 0.02$ $\gamma = 0.91 \pm 0.03$ $E_c = 2.09 \pm 0.07$	TS(OP) = 18	$N_0^{HE} = 0.3 \pm 0.1$ $\gamma = 4.4 \pm 0.6$
J2021+3651 [166]	-	$N_0 = 1.10 \pm 0.01$ $\gamma = 1.636 \pm 0.009$ $E_c = 3.12 \pm 0.05$	-	$N_0^{HE} = 0.720 \pm 0.008$ $\gamma = 4.41 \pm 0.02$
J2229+6114 [160]	$TS_{pwl} = 78$	$N_0 = 0.5027 \pm 0.0007$ $\gamma = 1.687 \pm 0.001$ $E_c = 3.67 \pm 0.01$	-	$N_0^{HE} = 0.71 \pm 0.13$ $\gamma = 3.5 \pm 0.4$

N_0 is the normalization factor in units of 10^{-10} cm^{-2} s^{-1} MeV^{-1}, N_0^{HE} is that of high-energy analysis in 10^{-14} cm^{-2} s^{-1} MeV^{-1}, E_c is the cut-off energy in GeV and γ is the spectral index (see Eqs. (2.1) and (2.2)). Errors include only statistical uncertainties.

[a] $E_0 = 1$ GeV for the analysis of 12 pulsars in the 100 MeV – 100 GeV energy range.

[b] $E_0 = 20$ GeV for those at energies >10 GeV.

[c] The spectral analysis of the Crab Nebula emission from 100 MeV to 100 GeV was performed with the two-component model reported in [12].

[d] The off-pulse analysis of PSR J0835−4510 (dominated by the Vela X emission) in both the full and high energy ranges was performed using a disk spatial template (from 2FGL) and a power-law model.

TABLE 2.3: Results of the spectral fits, obtained from the off-pulse analyses at energies >100 MeV and >10 GeV (columns 2 and 3, respectively). Spectral parameters are compared with those in the literature (references are in the last column). The forth column shows the results of a power-law fit of the diffuse Galactic background (GDB) emission above 10 GeV during off-pulse phases. Normalization factors N_0, $N_0^{\rm HE}$ and $N_{\rm GDB}^{\rm HE}$ are renormalized to the total phase interval. References to previous spectral analyses are reported in the first column.

OPs of pulsars	OP spectra		GDB
	>100 MeV[a]	>10 GeV[b]	power-law fit >10 GeV[b]
J0007+7303 [163],[170]	$N_0 = 0.07 \pm 0.01$ $\gamma = 2.2 \pm 0.1$ $E_c = 2.0 \pm 0.6$	-	$N_{\rm GDB}^{\rm HE} = 0.025 \pm 0.007$ $\gamma = 2.5 \pm 0.3$
J0534+2201[c] (Crab Nebula) [10],[12] ,[9]	$N_0^{\rm Sync} = 208 \pm 5$ $\gamma^{\rm Sync} = 3.59$ $E_0^{\rm Sync} = 100$ MeV $N_0^{\rm IC} = 5.3 \pm 1.4$ $\gamma_1^{\rm IC} = 1.48$ $\gamma_2^{\rm IC} = 2.19$ $E_0^{\rm IC} = 100$ MeV $E_b^{\rm IC} = 13.9$ GeV $\beta_1^{\rm IC} = 0.2$	$N_0^{\rm HE} = 14.7 \pm 0.7$ $\gamma = 1.93 \pm 0.07$	$N_{\rm GDB}^{\rm HE} = 0.06 \pm 0.01$ $\gamma = 3.2 \pm 0.4$
J0614−3329	$N_0 = 0.039 \pm 0.002$ $\gamma = 2.34 \pm 0.05$	-	-
J0633+1746	$N_0 = 2.69 \pm 0.09$ $\gamma = 1.45 \pm 0.02$ $E_c = 1.50 \pm 0.05$	-	$N_{\rm GDB}^{\rm HE} = 0.02 \pm 0.01$ $\gamma = 3.1 \pm 0.5$
J0835−4510[d] (Vela X) [168],[169],[25]	$N_0 = 0.323 \pm 0.007$ $\gamma = 2.272 \pm 0.016$	$N_0^{\rm HE} = 1.5 \pm 0.5$ $\gamma = 1.8 \pm 0.5$	$N_{\rm GDB}^{\rm HE} = 0.1 \pm 0.02$ $\gamma = 3.0 \pm 0.4$
J1028−5819	$N_0 = 0.19 \pm 0.05$ $\gamma = 1.4 \pm 0.2$ $E_c = 1.7 \pm 0.5$	-	$N_{\rm GDB}^{\rm HE} = 0.37 \pm 0.02$ $\gamma = 2.3 \pm 0.1$
J1048−5832	$N_0 = 0.026 \pm 0.005$ $\gamma = 2.3 \pm 0.1$	-	$N_{\rm GDB}^{\rm HE} = 0.24 \pm 0.02$ $\gamma = 2.64 \pm 0.17$
J1413−6205 [164]	$N_0 = 0.031 \pm 0.006$ $\gamma = 2.5 \pm 0.1$	-	$N_{\rm GDB}^{\rm HE} = 0.79 \pm 0.03$ $\gamma = 2.7 \pm 0.1$
J1809−2332	$N_0 = 0.047 \pm 0.006$ $\gamma = 2.50 \pm 0.08$	-	$N_{\rm GDB}^{\rm HE} = 0.32 \pm 0.02$ $\gamma = 2.5 \pm 0.1$
J1836+5925 [165]	$N_0 = 1.34 \pm 0.05$ $\gamma = 1.46 \pm 0.03$ $E_c = 2.1 \pm 0.1$	$N_0^{\rm HE} = 0.07 \pm 0.09$ $\gamma = 6.37 \pm 2.6$	$N_{\rm GDB}^{\rm HE} = 0.026 \pm 0.009$ $\gamma = 2.71 \pm 0.13$
J2021+3651 [45]	-	-	$N_{\rm GDB}^{\rm HE} = 0.27 \pm 0.02$ $\gamma = 2.67 \pm 0.16$
J2229+6114 [173]	$N_0 = 0.014 \pm 0.003$ $\gamma = 2.9 \pm 0.1$	-	$N_{\rm GDB}^{\rm HE} = 0.09 \pm 0.01$ $\gamma = 2.3 \pm 0.2$

N_0, $N_0^{\rm HE}$, E_c and γ are defined as in Table 2.2. $N_{\rm GDB}^{\rm HE}$ is the normalisation factor of the GDB power-law spectra in units of 10^{-14} cm^{-2} s^{-1} MeV^{-1} sr^{-1}. A power-law model was used to describe the OP emission from PSRs J0835−4510, J0614−3329, J1048−5832, J1413−6205, J1809−2332 and J2229+6114, whereas a PLEC model was used to fit OP component of PSRs J0007+7303, J0633−1746, J1028−5819 and J1836+5925 in the 100 MeV – 100 GeV energy range. PSR J2021+3651 shows no significant OP emission. Errors include only the statistical uncertainties.

[a] $E_0 = 1$ GeV for all OP components (except for PSR J0534+2201)

[b] $E_0 = 20$ GeV

[c] The spectral model of the Crab Nebula corresponds to the sum of the synchrotron (Sync) and inverse Compton (IC) components described by the power-law (Eq. (2.1)) and smoothly broken power-law models (Eq. (2.4) [12]), respectively. Normalization factors $N_0^{\rm Sync}$ and $N_0^{\rm IC}$ are both in units of 10^{-10} cm^{-2} s^{-1} MeV^{-1}.

[d] For the Vela X analyses a disk spatial template (from 2FGL) and a power-law model were used in both the full and high energy ranges.

2.3 (column 3). For all other pulsars no significant OP component was found during the off-pulse high-energy analysis.

In Figs. 2.2, 2.3 and 2.4 the best fitting high-energy spectra are compared with those from 1FHL (red and blue butterfly plots, respectively). For comparison in Fig. 2.2B I also show the VHE spectrum of the Crab pulsar (hatched area) found with the MAGIC telescope [96] and extrapolated down to 10 GeV. The hatched area in Fig. 2.3A corresponds to the *Fermi*-LAT spectrum of the Vela pulsar at energies >50 GeV [162]. The latter is characterized by a PLEC model with varying b-parameter, in contrast to the simple power law used in 1FHL.

Spectral parameters of significant OPs are presented in Figs. 2.5-2.7 and Table 2.3 (column 3, where all spectra are renormalized according to the total phase interval). The best fitting power-law OPs spectra are compared with those detected at VHE and extrapolated down to 10 GeV (red and hatched butterfly plots in Figs. 2.5A, 2.5B, 2.6A and 2.7B). Log-parabola and PLEC models were used to fit the MAGIC data of the Crab Nebula [9] and the H.E.S.S. data of Vela X [25], respectively.

The GDB emission above 10 GeV around each pulsar was estimated. Assuming a power-law spectral shape and uniform spatial distribution, I detected significant emission from the GDB around all pulsars, except for PSR J0614−3329, which is rather distant from the Galactic Plane (see column 4 in Table 2.3). The VHE measurements of the Galactic diffuse emission with ARGO-YBJ at 0.35–2 TeV [179] indicate that these estimates can be considered as conservative. Nevertheless, the contribution of the GDB to the total VHE background is not higher than 1%.

2.4.3 Simulated CTA Observations

Using the results of the spectral fitting at energies >10 GeV, I extrapolated the pulsar emission at VHE up to ∼160 TeV and simulated CTA observations of these objects, including an isotropic background, GDB and OP emission (if present). I consider observations with the northern or southern CTA installations (CTA-North and CTA-South). In Figs. 2.2-2.7 I compare extrapolated spectra of pulsars or their OP components with the sensitivity of the corresponding CTA installation. The resulting significances of point source detections in different energy bins (>0.04, >0.25 TeV) with or without background/OP subtraction are presented in Table 2.4. Count maps of all pulsars are shown in Figs. 2.8, 2.9 and 2.10.

I calculated optimistic and pessimistic spectra for each pulsar (from Eq. (2.5)), considering the uncertainties resulting from the high-energy *Fermi* spectral fits above 10 GeV

TABLE 2.4: Significances S of VHE pulsars detections during observations with the northern and southern CTA configuration for all data (VHE) and considering only the on-pulse phases (VHE-ON). The S-values are the square root of the corresponding test statistics (TS) in two energy bands (>0.04 and >0.25 TeV).

Pulsar	(Array $t^b_{\rm sim}$)	VHE		VHE-ON		
		>0.04 TeV	>0.25 TeV	>0.04 TeV	>0.25 TeV	($\Delta\phi^{\rm HE}_{\rm on}$)
J0007+7303	(North 50h)	$5.1^{+2.4}_{-2.0}$	-	$6.0^{+4.5}_{-3.1}$	-	(0.32)
J0534+2201[a]	(North 25h)	$6.0^{+1.2}_{-3.3}$	$2.6^{+1.4}_{-1.6}$	$20.3^{+7.4}_{-8.3}$	$5.2^{+4.5}_{-2.7}$	(0.10)
J0614−3329	(South 50h)	$7.4^{+5.8}_{-5.7}$	$4.8^{+4.2}_{-3.8}$	$19.6^{+12.7}_{-13.0}$	$8.9^{+8.4}_{-8.9}$	(0.16)
J0633+1746	(North 50h)	-	-	$3.4^{+1.4}_{-0.7}$	-	(0.26)
J0835−4510[a]	(South 25h)	$28.2^{+4.2}_{-3.5}$	-	$37.1^{+6.2}_{-3.9}$	$4.5^{+0.7}_{-0.6}$	(0.49)
J1028−5819	(South 50h)	$0.0^{+5.8}_{-0.0}$	-	$14.4^{+7.9}_{-8.9}$	$0.0^{+7.6}_{-0.0}$	(0.08)
J1048−5832	(South 50h)	-	-	$2.9^{+2.1}_{-2.9}$	-	(0.18)
J1413−6205	(South 50h)	$0.0^{+4.7}_{-0.0}$	-	$4.4^{+4.9}_{-3.6}$	-	(0.28)
J1809−2332	(South 50h)	-	-	$0.0^{+5.2}_{-0.0}$	-	(0.16)
J1836+5925[a]	(North 50h)	-	-	-	-	(0.36)
J2021+3651	(North 50h)	-	-	-	-	(0.11)
J2229+6114	(North 50h)	$2.5^{+2.6}_{-2.5}$	-	$6.3^{+5.0}_{-4.8}$	$1.7^{+5.2}_{-1.7}$	(0.25)

[a]Pulsars simulated with OP emission.
[b]$t_{\rm sim}$ is a duration of the observations.

(red butterfly plots in Figs. 2.2-2.4). Performing simulations, similar to those described above, the corresponding uncertainties in the significance S were obtained (see Table 2.4).

As shown in Table 2.4 (column 3), the simulated observations with CTA above 0.04 TeV show significant detections for PSRs J0007+7303 (50 h), J0534+2201 (25 h), J0614−3329 (50 h), J0835−4510 (25 h), J1028−5819 (50 h), J1413−6205 (50 h) and J2229+6114 (50 h)[17]. In addition, pulsars J0633+1746, J1048−5832 (50 h) and J1809−2332 are significantly detected in 50 hours after off-pulse background subtraction (Table 2.4, column 5, VHE-ON). A longer observing time is required for a significant detection of other pulsars above 0.04 TeV.

I also considered different energy intervals. Pulsars J0534+2201 and J0614−3329 can be detected at energies >0.25 TeV on the full pulse analysis, while other 3 pulsars (PSRs J0835−4510, J1028−5819 and J2229+6114) turn out to be detectable in the on-pulse analysis. Only PSR J0614−3329 can be marginally detected above 1 TeV with $S = 2.3^{+2.2}_{-2.3}$ ($6.7^{+3.5}_{-6.7}$ for on-pulse intervals) during simulated observations with the same exposure times.

[17]$S \geq 5$ at least. Pulsar J1413−6205 has $S = 4.7$ and I consider it very close to the significance threshold.

2.4.4 Analysis of Pass 8 *Fermi*-LAT Data

I repeated all the simulations using the results of the high-energy (>10 GeV) spectral fits of recently the released Pass 8 *Fermi*-LAT data[18]. The new data provide better measurements of the energy and position for each event in a wider energy range, than the previous Pass 7 data used above. This allows us to obtain better spectral fits especially in the high-energy tail of the pulsars spectra (>10 GeV). This leads in turn to more realistic VHE simulations.

For all HE *Fermi* pulsars I analyzed 5-year Pass 8 data at energies >10 GeV using the ephemerides reported above (see [175] and Table 2.1). The adopted IRF is "P8R2_SOURCE_V6"[19]. The background components included in the spectral fitting are the Galactic (*gll_iem_v06*) and isotropic diffuse emission (*iso_P8R2_SOURCE_V6_v06*)[20]. Spectra of all point sources and non-background diffuse sources included in the analysis are taken from 3FGL [94].

I extrapolated the best-fit power-law spectra of each pulsar (Table 2.5) up to ∼160 TeV and simulated CTA observations of these objects (similarly to what done for Pass 7 data in Sect. 2.4.3). The significances of the pulsars detection with CTA are listed in Table 2.6.

More than 7 years of *Fermi*-LAT data are available to date. In order to accurately fold light curves of HE *Fermi* pulsars using the full data set, new ephemerids that account for the effects of the timing noise are required. However, there are two pulsars of our sample, J0614−3329 and J1836+5925, that have a rather stable timing evolution and for which the ephemerides over a 5-year time interval provide a rather accurate timing solution also for 7 years. For these objects I performed an analysis of the high-energy data acquired from MJD 54682 to MJD 57350 (∼7 years). The resulting spectra and detection significances are reported in Tables 2.5 and 2.6, respectively.

The calculations performed for Pass 8 data at energies > 10 GeV give results similar to those from the Pass 7 analysis, which will be discussed in Sect. 2.5.

2.5 Discussion

In this chapter I presented the spectral analysis of 12 HE *Fermi* pulsars in the full *Fermi* bandpass (100 MeV – 100 GeV) and at high energies (>10 GeV). It was found that

[18] http://fermi.gsfc.nasa.gov/ssc/data/analysis/documentation/Pass8_usage.html
[19] http://fermi.gsfc.nasa.gov/ssc/data/analysis/LAT_caveats.html
[20] http://fermi.gsfc.nasa.gov/ssc/data/access/lat/BackgroundModels.html

TABLE 2.5: Results of the Pass 8 spectral analysis above 10 GeV for our sample of high-energy *Fermi* pulsars. The second column contains the significances of the OP components from the off-pulse spectral fits above 10 GeV. Best fit spectral parameters of the power-law spectra at energies >10 GeV are reported in the third column.

Pulsar	Spectral Pass 8 analysis >10 GeV	
	off-pulse	on-pulse
5 years of data		
J0007+7303	-	$N_0^{\rm HE} = 2.6 \pm 0.2$ $\gamma = 4.07 \pm 0.16$
J0534+2201 (Crab)	TS(Crab Nebula) = 8530	$N_0^{\rm HE} = 3.4 \pm 0.3$ $\gamma = 3.0 \pm 0.2$
J0614−3329	-	$N_0^{\rm HE} = 0.93 \pm 0.14$ $\gamma = 3.5 \pm 0.3$
J0633+1746 (Geminga)	-	$N_0^{\rm HE} = 3.6 \pm 0.3$ $\gamma = 5.2 \pm 0.16$
J0835−4510[a] (Vela)	TS(Vela X) = 13	$N_0^{\rm HE} = 19.0 \pm 0.7$ $\gamma = 4.41 \pm 0.07$
J1028−5819	-	$N_0^{\rm HE} = 0.63 \pm 0.13$ $\gamma = 4.0 \pm 0.4$
J1048−5832	-	$N_0^{\rm HE} = 0.25 \pm 0.09$ $\gamma = 4.4 \pm 0.7$
J1413−6205	-	$N_0^{\rm HE} = 0.485 \pm 0.004$ $\gamma = 3.92 \pm 0.02$
J1809−2332	-	$N_0^{\rm HE} = 0.83 \pm 0.14$ $\gamma = 4.2 \pm 0.3$
J1836+5925	TS(OP) = 119	$N_0^{\rm HE} = 0.34 \pm 0.09$ $\gamma = 4.1 \pm 0.5$
J2021+3651	-	$N_0^{\rm HE} = 0.72 \pm 0.14$ $\gamma = 4.7 \pm 0.4$
J2229+6114	-	$N_0^{\rm HE} = 0.58 \pm 0.10$ $\gamma = 3.4 \pm 0.4$
7 years of data		
J0614−3329	-	$N_0^{\rm HE} = 0.85 \pm 0.11$ $\gamma = 3.7 \pm 0.3$
J1836+5925	TS(OP) = 130	$N_0^{\rm HE} = 0.31 \pm 0.07$ $\gamma = 4.4 \pm 0.5$

$N_0^{\rm HE}$ is the normalization factor in units of 10^{-14} cm^{-2} s^{-1} MeV^{-1} and γ is the spectral index (see Eq. (2.1), $E_0 = 20$ GeV). Errors include only statistical uncertainties.

[a]The off-pulse analysis of PSR J0835−4510 in the high energy range (dominated by the Vela X diffuse emission) was performed using a disk spatial template (from 3FGL) and a power-law model.

TABLE 2.6: Same as Table 2.4 for pulsars spectra obtained from an analysis of Pass 8 *Fermi*-LAT data.

Pulsar	(Array $t^{b}_{\rm sim}$)	VHE		VHE-ON		
		>0.04 TeV	>0.25 TeV	>0.04 TeV	>0.25 TeV	($\Delta\phi^{\rm HE}_{\rm on}$)
5 years of data						
J0007+7303	(North 50h)	$4.7^{+1.2}_{-1.3}$	-	$6.7^{+1.2}_{-1.6}$	-	(0.33)
J0534+2201[a]	(North 25h)	$7.1^{+1.6}_{-2.1}$	-	$21.2^{+4.3}_{-5.4}$	$4.6^{+3.7}_{-4.6}$	(0.13)
J0614−3329	(South 50h)	$6.6^{+4.0}_{-3.0}$	$3.4^{+3.5}_{-2.6}$	$16.5^{+7.7}_{-9.0}$	$5.0^{+7.0}_{-5.0}$	(0.20)
J0633+1746	(North 50h)	-	-	$2.5^{+1.1}_{-0.0}$	-	(0.22)
J0835−4510[a]	(South 25h)	$28.2^{+2.6}_{-3.7}$	-	$40.3^{+3.5}_{-4.2}$	$2.4^{+2.1}_{-2.4}$	(0.49)
J1028−5819	(South 50h)	$0.0^{+3.9}_{-0.0}$	-	$5.8^{+5.4}_{-5.0}$	-	(0.16)
J1048−5832	(South 50h)	-	-	-	-	(0.25)
J1413−6205	(South 50h)	-	-	$3.5^{+0.7}_{-0.4}$	-	(0.22)
J1809−2332	(South 50h)	-	-	$8.6^{+2.8}_{-5.0}$	-	(0.11)
J1836+5925[a]	(North 50h)	-	-	-	-	(0.44)
J2021+3651	(North 50h)	-	-	-	-	(0.12)
J2229+6114	(North 50h)	$1.8^{+3.0}_{-1.8}$	$0.0^{+3.1}_{-0.0}$	$5.4^{+8.1}_{-5.4}$	$3.5^{+4.8}_{-3.4}$	(0.15)
7 years of data						
J0614−3329	(South 50h)	$4.2^{+2.4}_{-4.2}$	$2.7^{+1.2}_{-1.8}$	$10.7^{+6.4}_{-5.6}$	$3.7^{+2.3}_{-3.7}$	(0.20)
J1836+5925[a]	(North 50h)	-	-	-	-	(0.44)

[a]Pulsars simulated with OP emission.
[b]$t_{\rm sim}$ is the duration of the observations.

PSRs J0534+2201, J0835−4510 and J1836+5925 have significant OP emission above 10 GeV.

The results of the *Fermi*-analysis are compared with those from the literature (for references see Tables 2.2 and 2.3) and from the 1FHL catalog. I performed the spectral analysis of both the on- and off- peak components in the full *Fermi*-LAT energy range. In almost all cases the found spectra are consistent with those from the previous investigations. Only for PSR J1836+5925 obtained spectrum shows significant differences below a few GeV with respect to e.g. Abdo et al. [165] (see Fig. 2.4B). Spectra adopted from the previous works [87, 165, 167][21] are phase-averaged and does not account for the OP component. For the sake of comparison I then performed additional spectral fits of PSR J1836+5925 assuming no contribution from the OP emission. Spectral parameters resulting from this analysis are consistent with those from the literature (see dashed line in Fig. 2.4B). However, since the spectral analysis of PSR J1836+5925 shows the presence of significant OP emission, I considered it more accurate and used it for performing the VHE spectral simulations.

For the Crab pulsar, the spectral parameters obtained from the analysis in the full and high energy ranges are consistent with those from the detailed investigations made by Abdo et al. [10] and Buehler et al. [12], who considered the Crab Nebula emission. However, these results are rather different from those reported in 2FGL or 1FHL. In

[21]It should be noted that Abdo et al. [165] reported both a phase-resolved and phase-averaged spectral analyses for PSR J1836+5925. However, in this work I refer only to phase-averaged one.

both these catalogs the spectral analysis of all pulsars was performed without taking into account for the presence of OP components.

It should be noted that the high-energy spectral fit of the Crab pulsar obtained for the data within $\Delta\phi_{\rm on}^{\rm HE}$ phases is not consistent with the spectral energy distribution above 10 GeV calculated for the $\Delta\phi_{\rm on}$ intervals (see red line and black data points in Fig. 2.2B). I then calculated the spectral energy distribution at energies >10 GeV for the data corresponding to the $\Delta\phi_{\rm on}^{\rm HE}$ phase intervals and found that they are consistent with the high-energy spectral fit (see gray data points in Fig. 2.2B). Such an effect may take place also for other HE *Fermi* pulsars, but it is probably negligible because we do not observe significant bridge emission above 10 GeV (see Figs. 2.1 and 2.2-2.4).

I obtained the spectra of the OP emission in the 100 MeV – 100 GeV energy range for all pulsars except PSR J2021+3651, which showed no significant irrespective of the adopted models. In contrast to what reported in 2PC and in [163] for PSR J0007+7303, the present analyses resulted in the detection of a significant exponential cut-off tail in the OP emission at energies >100 MeV (Fig. 2.5A). On the contrary, I found no evidence of an exponential cut-off in the OP spectrum of PSR J1809−2332 (see Figs. 2.5, 2.6 and 2.7).

I then simulated CTA observations of our sample of 12 energetic gamma-ray pulsars detected with the *Fermi*-LAT. Assuming that the VHE pulsar spectrum is an extrapolation of the high-energy *Fermi* spectral fit above 10 GeV, I calculated significances of pulsar detection. So far, there are only two pulsars, for which significant pulsations, have been detected with ground-based Cherenkov telescopes – the Crab and Vela pulsars (with MAGIC [96, 97], VERITAS [99] and H.E.S.S.[22]). According to performed calculations CTA will probably detect ∼7–10 HE *Fermi* pulsars (during 50 hours, >40 GeV). Although the angular resolution of CTA improves with energy [see e.g. 151], which tends to lead to an improvement in the detection significance because of a decrease in the isotropic background contamination[23], only 2 pulsars J0534+2201 and J0614−3329 with rather flat spectra ($\gamma = 3.0$ and $\gamma = 3.4$, respectively) are still bright enough for the CTA detection above 0.25 TeV. PSR J2229+6114 which has a similar spectral index ($\gamma = 3.5$) is not significantly detected due to the lower flux and higher GDB contamination. Considering only the on-peak emission, I obtain significant detection at energies >0.25 TeV also for pulsars J0835−4510, J1028−5819 and J2229+6114. Above 1 TeV only PSR J0614−3329 is sufficiently bright to be detectable. Despite of the even harder high-energy spectrum ($\gamma = 3.0$), a simulation of a 25-hour observation of the Crab pulsar

[22] http://www.mpg.de/8287998/velar-pulsar

[23] For CTA-South the 68% of the PSF at 0.04, 0.25 and 1 TeV is 0.19°, 0.09° and 0.05°, respectively

above 1 TeV yields $S < 5$ because of the presence of the bright point-like (in gamma rays) Crab Nebula.

In addition to the pulse-averaged point source detection discussed above, I calculated also the S-values corresponding to the most prominent peak emission from each pulsar, concentrated within the on-pulse phase intervals (see columns 5, 6 in Table 2.4). Considering only the counts within these specific phases (see Fig. 2.1), it is possible to increase the signal-to-noise ratio. This leads to higher detection significances as compared to the phase-averaged ones. On-pulse phase intervals $\Delta\phi_{\rm on}^{\rm HE}$ were obtained from the *Fermi*-LAT high-energy pulse profiles (>10 GeV). These values are smaller than those obtained in the 100 MeV – 100 GeV energy range (cmp. $\Delta\phi_{\rm on}$ and $\Delta\phi_{\rm on}^{\rm HE}$ in Table 2.1). Recent results from MAGIC and VERITAS confirm this trend of narrowing of the pulsars peaks with energy, found with the *Fermi*-LAT at energies from 100 MeV to 100 GeV [see 10, 96, 97, 99]. Therefore, in this respect the results presented here can be considered as rather conservative. Clearly, in order to perform this type of measurements a knowledge of the accurate pulsars ephemerides is required, which can be obtained from simultaneous low-energy observations (e.g. radio, optical).

Obtained results are strongly dependent on the assumed spectral behaviour of pulsars above few hundreds GeV. Comparing the extrapolated VHE spectral slope of the Crab pulsar ($\gamma = 3.0 \pm 0.2$) with that obtained with MAGIC ($\gamma_{\rm MAGIC} = 3.57 \pm 0.27$, from [96]) and VERITAS ($\gamma_{\rm VERITAS} = 3.8 \pm 0.5$, from [99]), it appears that the value obtained here is slightly flatter, but still marginally consistent within the error bars[24]. In this respect, our extrapolated VHE spectral slopes may be considered to provide upper limits to the detection significance for each pulsar, which, in any case, is not expected to be much lower. However, recent spectral results reported in [118] for the main pulse and the interpulse indicate that the spectrum of the Crab pulsar is flatter ($\gamma \sim 3.0$) than what was obtained in previous measurements, which is consistent with our estimates.

It should be noted that the extrapolation of the OP spectra to VHE can also affect the results of simulations. This is particularly relevant for PSRs J0534+2201, J0835−4510 and J1836+5925. For the Crab Nebula, the spectrum used in our calculations is harder than that recently obtained with IACTs (see Figs. 2.5B and [9]). This leads to an underestimation of the Crab pulsar significances. Simulations of 25-hour observations of the Crab pulsar performed with the log-parabola model of the Crab Nebula from [9] give the following values for the detection significances S:

- for all data (VHE):
  - >40 GeV: $6.3^{+5.6}_{-2.7}$

[24] Only statistical uncertainties are reported here.

  - >250 GeV: $0.0^{+5.0}_{-0.0}$

- for on-pulse phases (VHE-ON):
  - >40 GeV: $25.3^{+11.6}_{-7.6}$
  - >250 GeV: $10.0^{+3.9}_{-5.6}$

Detailed investigations of the VHE emission from the Vela pulsar and its PWN are presented and discussed in Chapter 4.

Alternative criteria for the selection of good candidates for VHE detection were investigated within the framework of 1FHL [95]. None of the HE *Fermi* pulsars, except those which have been already detected at VHE (extended emission in PSRs J0007+7303, J0633+1746, J0835−4510, J2021+3651, J2229+6114 and point-like emission in PSR J0534+2201), passed these criteria. de Oña-Wilhelmi et al. [120] estimated a number of gamma-ray pulsars detectable with CTA, assuming a power-law tail with $\gamma = 3.52$ above the cut-off energies for the whole population of pulsars. They found that about 20 pulsars will be detected in 50 hours with the full-energy-range CTA configuration.

During the first years of operations, CTA will focus on the observations of the most interesting objects in our Galaxy. Several regions are being considered for the CTA Key Science observational program (KSP). Cygnus and η-Carina regions together with the central part of the Galactic plane are among the primary candidates of the Galactic Science studies. Some of the sky regions where HE *Fermi* pulsars are located will be covered by CTA during KSP observations: the Cygnus region contains PSR J2021+3651; η-Carina is in the vicinity of PSRs J1028−5819 and J1048−5832; PSRs J1413−6205 and J1809−2332 will be observed during the Galactic Plane Survey (GPS). According to the results of the simulations performed here, the total observing time of each KSP (as envisaged at present) would not be sufficient to detect the pulsars. However, considering the large uncertainties on the actual VHE pulsar spectrum, I performed an additional set of simulations to assess what is the minimum value of the spectral index for which a pulsar detection would be possible. Fixing all other parameters including those of the background, I obtain the value of $\gamma_{\rm signif}$, with which a hypothetical point source would be significantly detected ($S = 5$) with CTA during observing time $t_{\rm obs}$ within the framework of KSPs (Table 2.7). These values are flatter than those from our analysis, but some of them are consistent with the spectral index obtained for the Crab pulsar at VHE (3.57 ± 0.27 from [96] and 3.8 ± 0.5 from [99]).

TABLE 2.7: Pulsars in sky areas covered by the CTA Key Science Projects with observing time $t_{\rm obs}$ and corresponding minimum value of the spectral index for a significant detection.

Pulsar	KSP ($t_{\rm obs}$)	$\gamma_{\rm signif}$
J1028−5819	Carina (25h)	3.4
J1048−5832	Carina (25h)	3.0
J1413−6205	GPS (11h)	3.0
J1809−2332	GPS (11h)	3.4
J2021+3651	Cygnus (20h)	3.2

2.6 Conclusions

I presented the prospects of pulsars detection at VHE with the next-generation IACT instrument – CTA. In our most optimistic scenarios CTA will increase the number of known VHE gamma-ray pulsars by a factor 10. I also found that up to 5 pulsars of our sample are sufficiently bright to be significantly detected with CTA above 250 GeV. PSR J0614−3329 is detectable also above 1 TeV. Observations of HE *Fermi* pulsars in the energy range from 100 GeV up to several TeV will help us to clarify whether the VHE emission is intrinsic to all gamma-ray pulsars or unique only to the Crab pulsar.

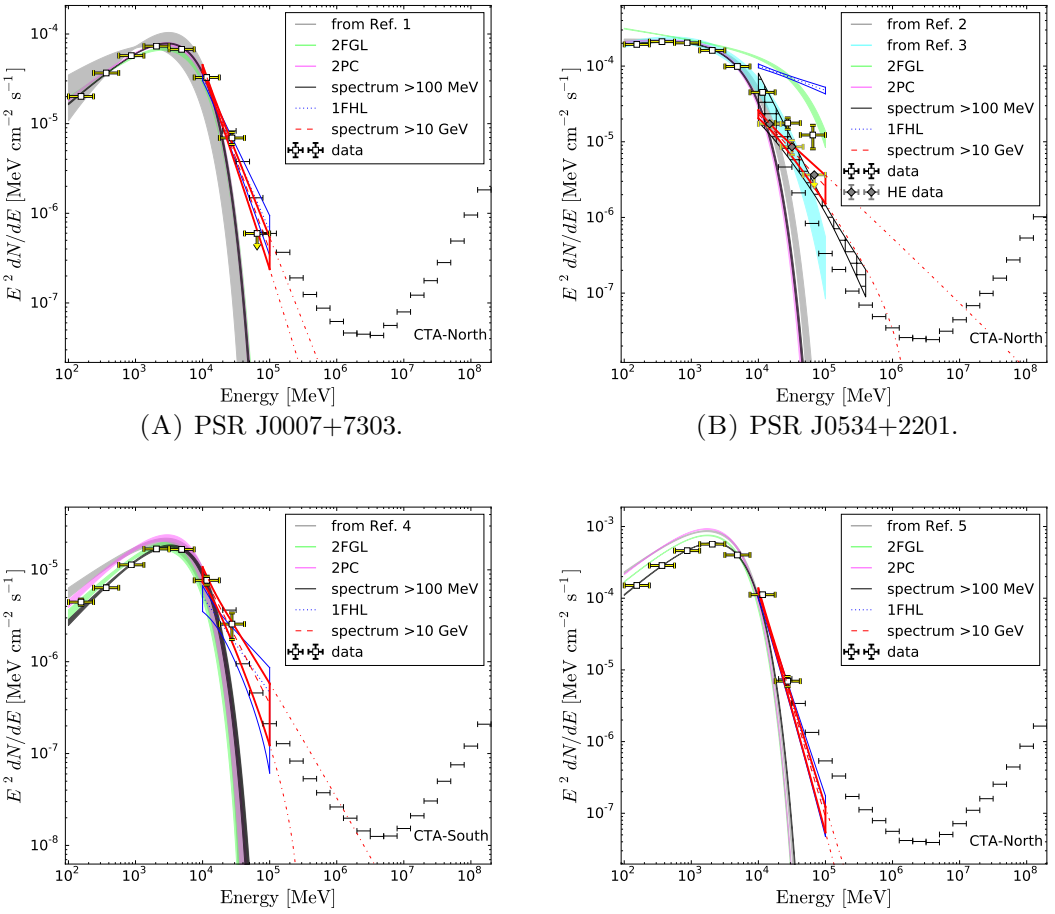

(A) PSR J0007+7303. (B) PSR J0534+2201.

(C) PSR J0614−3329. (D) PSR J0633+1746.

FIGURE 2.2: Spectral energy distributions of PSRs J0007+7303, J0534+2201 (Crab), J0614−3329 and J0633+1746 (Geminga) in the full *Fermi*-LAT energy range (100 MeV – 100 GeV, black) and above 10 GeV (red), compared with those from the literature (grey, cyan, see references in Table 2.2), 2FGL (green, from [167]), the PLEC1 model with fixed $b = 1$ from 2PC (magenta, from [87]), 1FHL (blue, from [95]). The red dashed (blue dotted) lines correspond to the mean values of spectra from the high-energy fits (>10 GeV). Horizontal bars represent the sensitivity curve of CTA-North or CTA-South installation, renormalized by the square root of the on-pulse phase interval of each pulsar. The red dot-dashed lines are the high-energy fits extrapolated up to ∼160 TeV. The hatched area in Fig. 2.2B corresponds to the VHE spectrum found with MAGIC [96] and extrapolated down to 10 GeV. Black dots show the the *Fermi*-LAT spectral energy distribution in eight energy bins (upper limits correspond to $\mathrm{TS}_i < 9$, see text for details), whereas gray data points in Fig. 2.2B correspond to three high-energy bins calculated within $\Delta\phi_{\mathrm{on}}^{\mathrm{HE}}$ phase interval. Only statistical errors are considered in all butterfly plots and spectral energy distribution dots. References: 1. Abdo et al. [163]; 2. Abdo et al. [10]; 3. Buehler et al. [12]; 4. Ransom et al. [157]; 5. Abdo et al. [158].

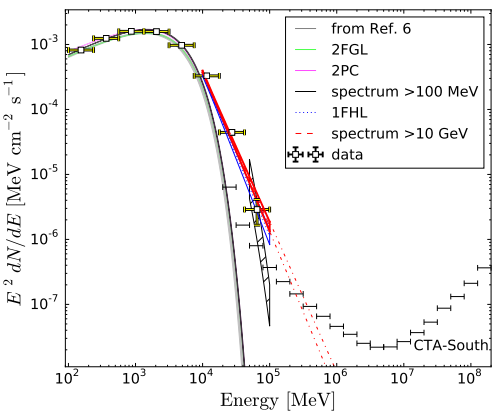

(A) PSR J0835−4510.

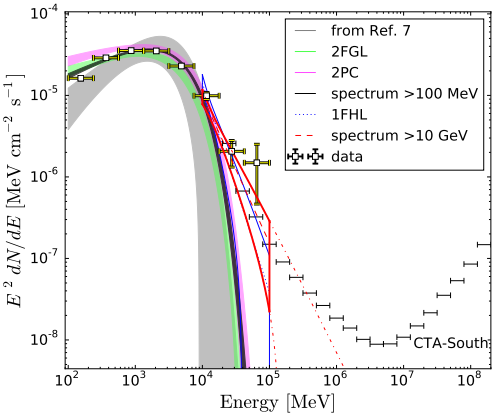

(B) PSR J1028−5819.

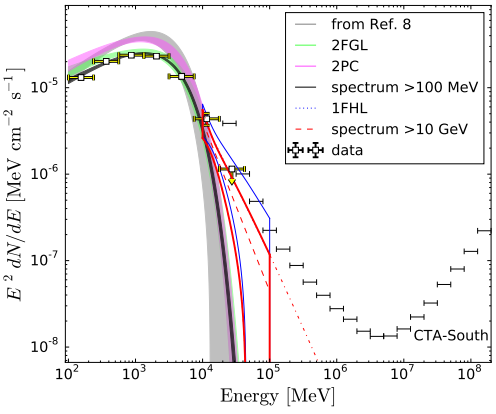

(C) PSR J1048−5832.

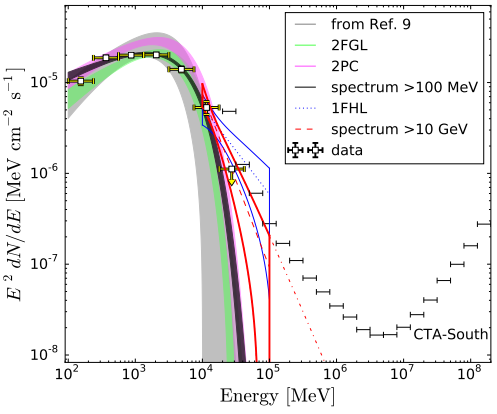

(D) PSR J1413−6205.

FIGURE 2.3: Same as Fig. 2.2 for PSRs J0835−4510 (Vela), J1028−5819, J1048−5832 and J1413−6205. The hatched area in Fig. 2.3A represents the results of the spectral analysis at energies >50 GeV from [162]. References: 6. Abdo et al. [161]; 7. Abdo et al. [159]; 8. Abdo et al. [160]; 9. Saz Parkinson et al. [164].

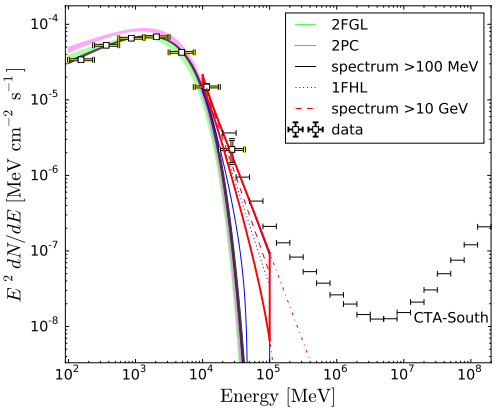

(A) PSR J1809−2332.

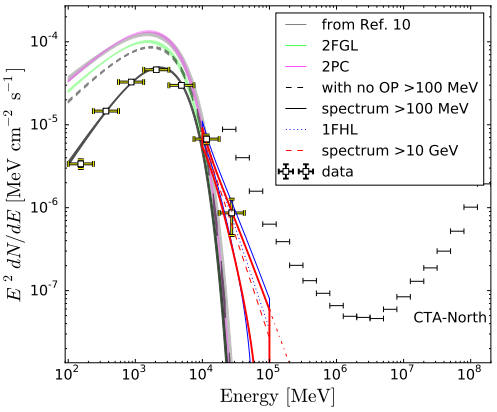

(B) PSR J1836+5925.

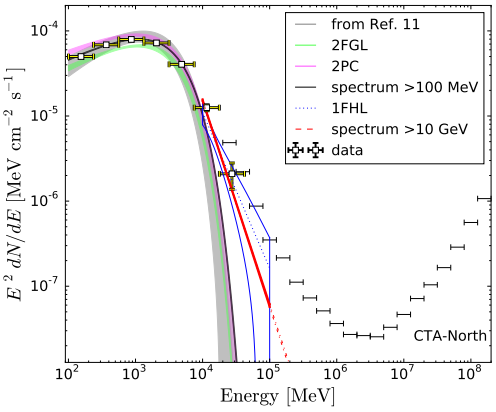

(C) PSR J2021+3651.

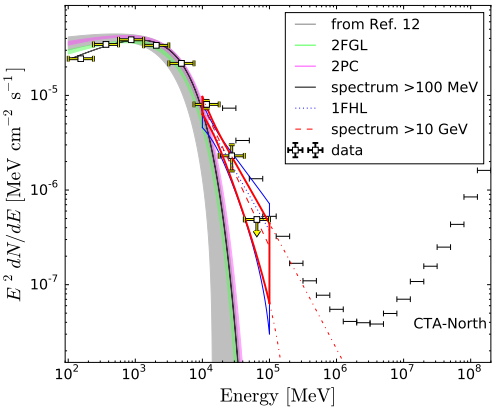

(D) PSR J2229+6114.

FIGURE 2.4: Same as Fig. 2.2 for PSRs J1809−2332, J1836+5925, J2021+3651 and J2229+6114. The black dashed spectrum in Fig. 2.4B corresponds to the spectral analysis of PSR J1836+5925 above 100 MeV without taking into account OP emission. References: 10. Abdo et al. [165]; 11. Abdo et al. [166]; 12. Abdo et al. [160].

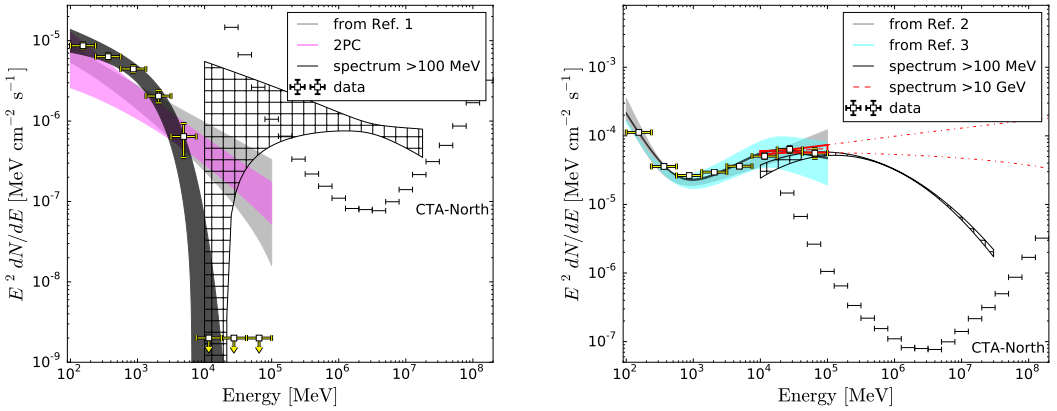

(A) PSR J0007+7303. (B) PSR J0534+2201.

(C) PSR J0614−3329. (D) PSR J0633+1746.

FIGURE 2.5: Point sources off-peak (OPs) spectral energy distributions in PSRs J0007+7303, J0534+2201, J0614−3329 and J0633+1746 in the full *Fermi*-LAT energy range (100 MeV – 100 GeV, black) and above 10 GeV (red), compared with those from the literature (grey, cyan, see references in Table 2.3), 2PC (magenta, from [87]). The red dashed lines correspond to the mean values of spectra from the high-energy fits (>10 GeV). Horizontal bars represent the sensitivity curve of CTA-North or CTA-South installation. The red dot-dashed lines are the high-energy fits extrapolated up to ∼160 TeV. Hatched areas in Figs. 2.5A and 2.5B are the VHE spectra, extrapolated down to 10 GeV from [170] and [9], respectively. Dots show the *Fermi*-LAT spectral energy distribution in eight energy bins (upper limits correspond to TS< 9, see text for the details). Only statistical errors are considered in all butterfly plots and spectral energy distribution dots. References: 1. Abdo et al. [163]; 2. Abdo et al. [10]; 3. Buehler et al. [12].

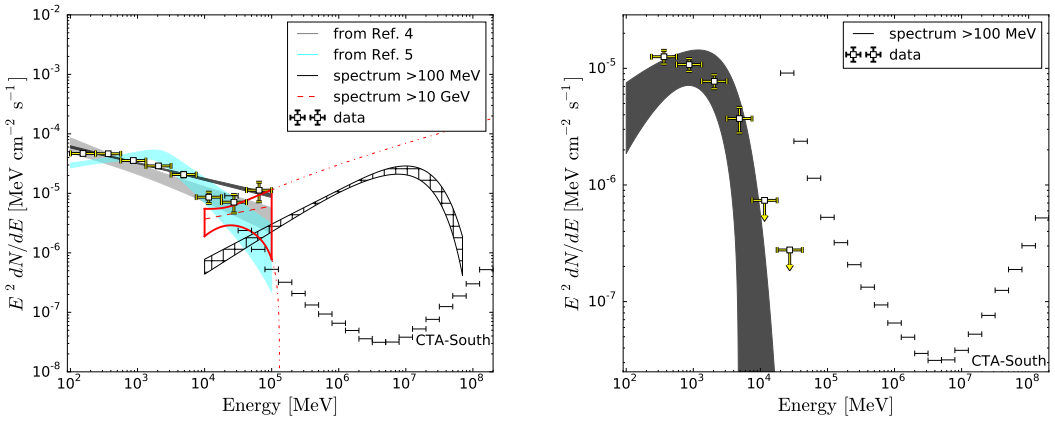

(A) PSR J0835−4510.

(B) PSR J1028−5819.

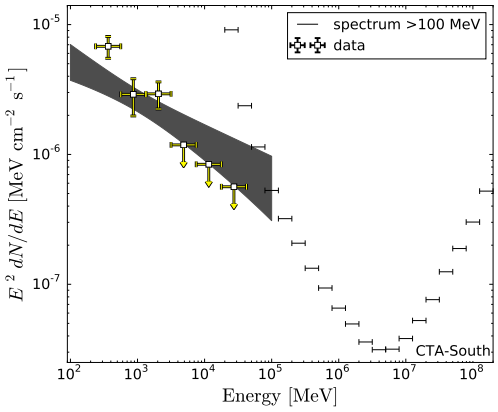

(C) PSR J1048−5832.

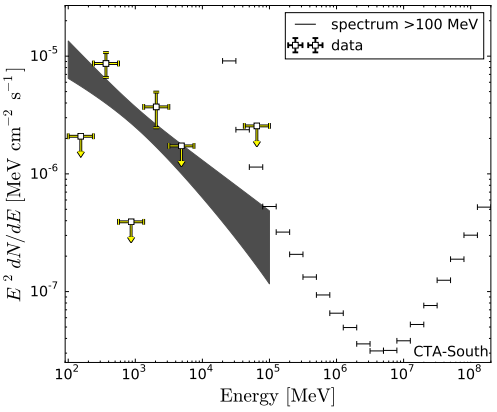

(D) PSR J1413−6205.

FIGURE 2.6: Same as Fig. 2.5 for PSRs J0835−4510, J1028−5819, J1048−5832 and J1413−6205. The hatched area in Fig. 2.6A is the VHE spectrum, extrapolated down to 10 GeV from [25]. The off-peak component of PSR J0835−4510 is dominated by the diffuse Vela X emission (disk spatial template from 3FGL). References: 4. Abdo et al. [168]; 5. Grondin et al. [169].

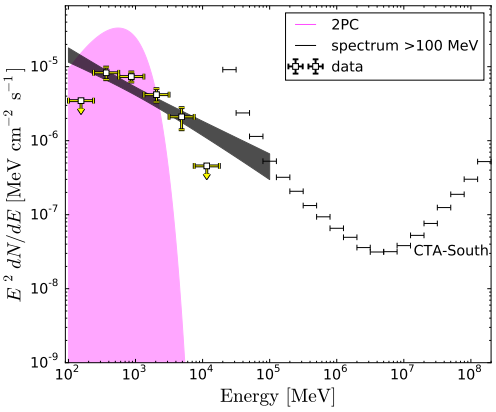

(A) PSR J1809−2332.

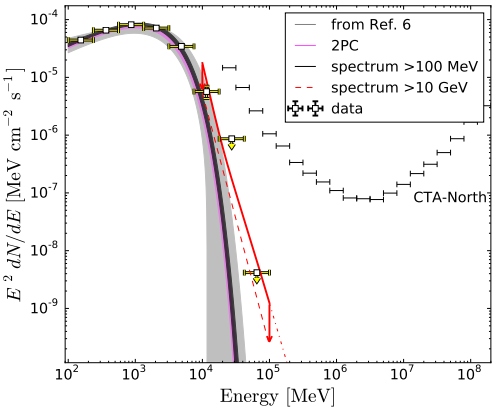

(B) PSR J1836+5925.

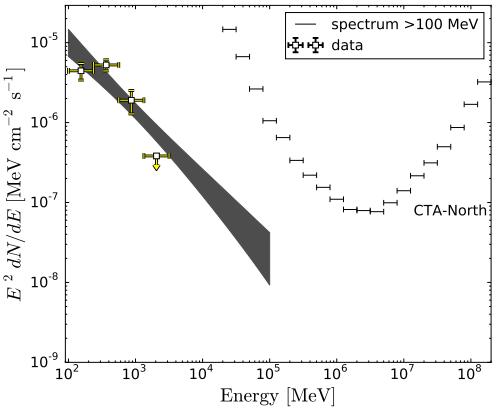

(C) PSR J2229+6114.

FIGURE 2.7: Same as Fig. 2.5 for PSRs J1809−2332, J1836+5925 and J2229+6114. For PSR J1836+5925 the arrows correspond to the upper bound of the corresponding spectra. References: 6. Abdo et al. [165].

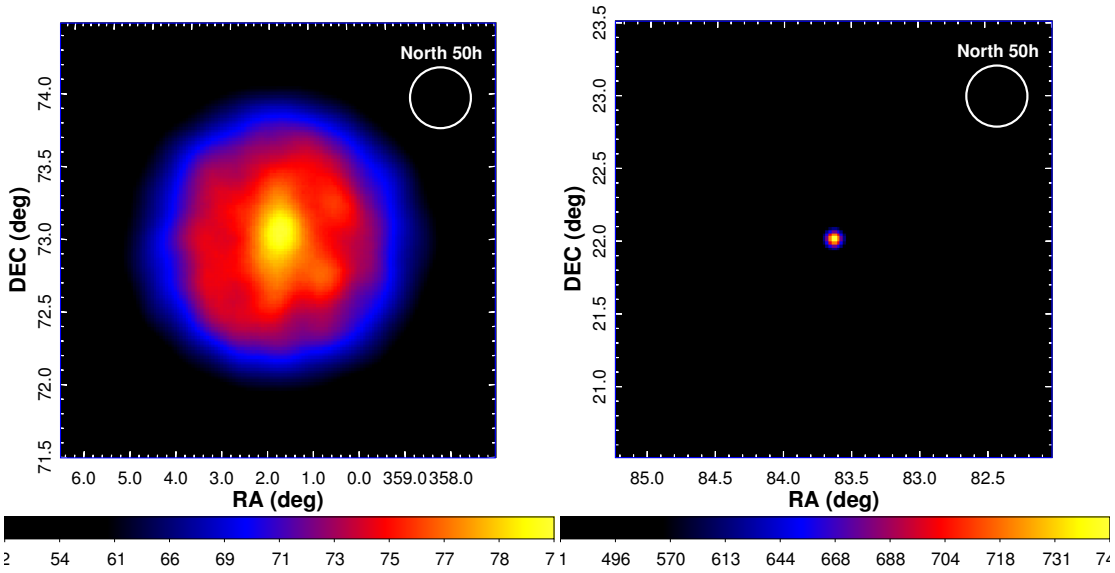

(A) PSR J0007+7303. (B) PSR J0534+2201 with Crab Nebula.

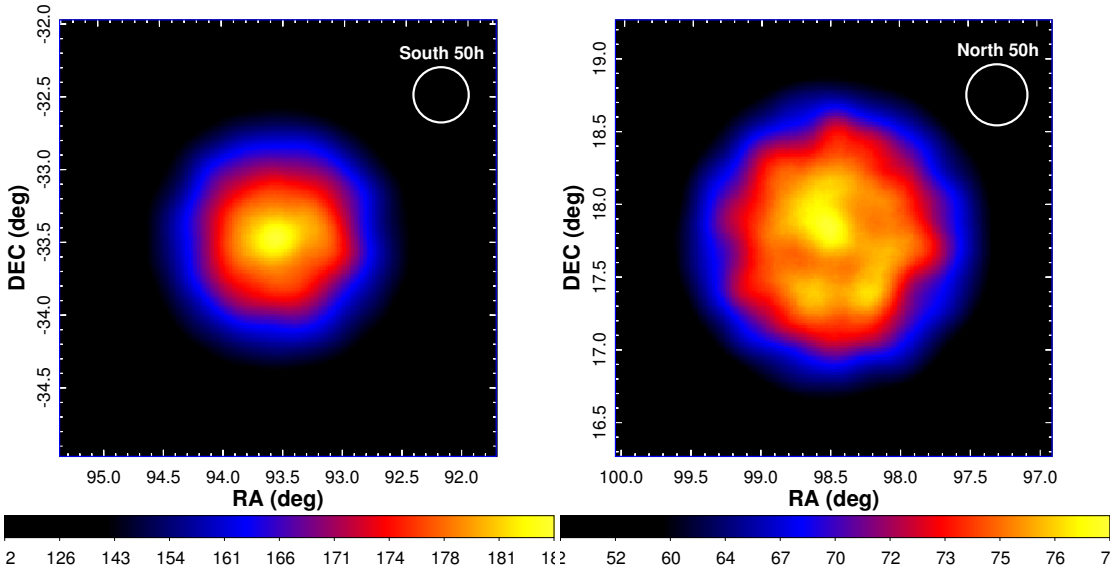

(C) PSR J0614−3329. (D) PSR J0633+1746 (Geminga).

FIGURE 2.8: VHE count maps of PSRs J0007+7303, J0534+2201, J0614−3329 and J0633+1746, simulated with *ctools* in the 0.04–160 TeV energy range. Each map covers a 3° × 3° area on the sky centered on the pulsars position. x-, y- axes are right ascension (RA) and declination (DEC) in degrees, respectively. The Color bars represent the number of counts in power scale. Simulations are computed assuming a 50-hour exposure of the central point source and background. For PSR J0534+2201 the exposure time is 25 hours and also the PWN emission is included in the simulation. All count maps are smoothed with the 68% of the PSF at 0.04 TeV, equaled to 0.21° and 0.19° for CTA-North and CTA-South arrays (white circles), respectively.

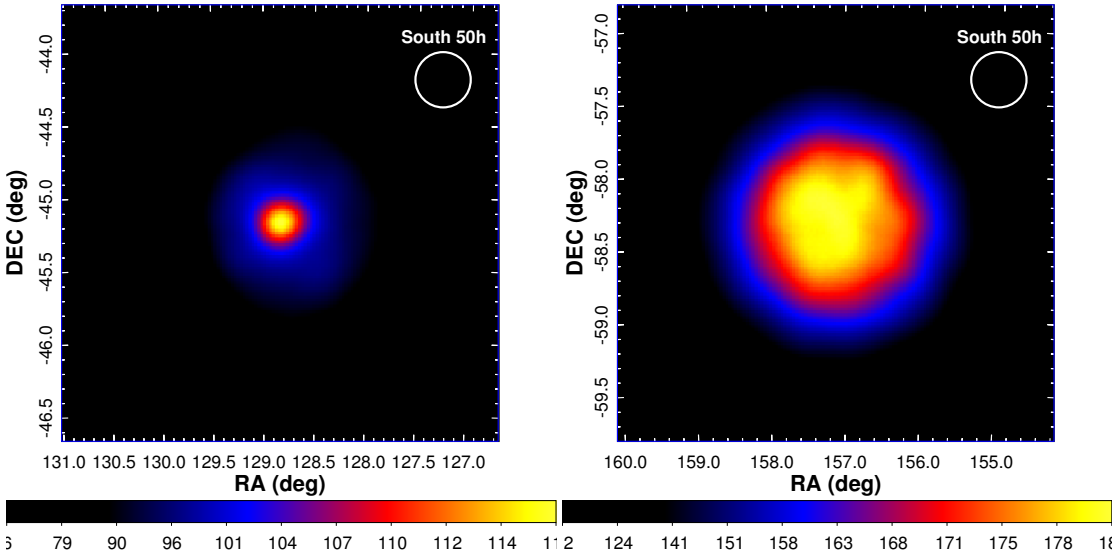

(A) PSR J0835−4510 with Vela X. (B) PSR J1028−5819.

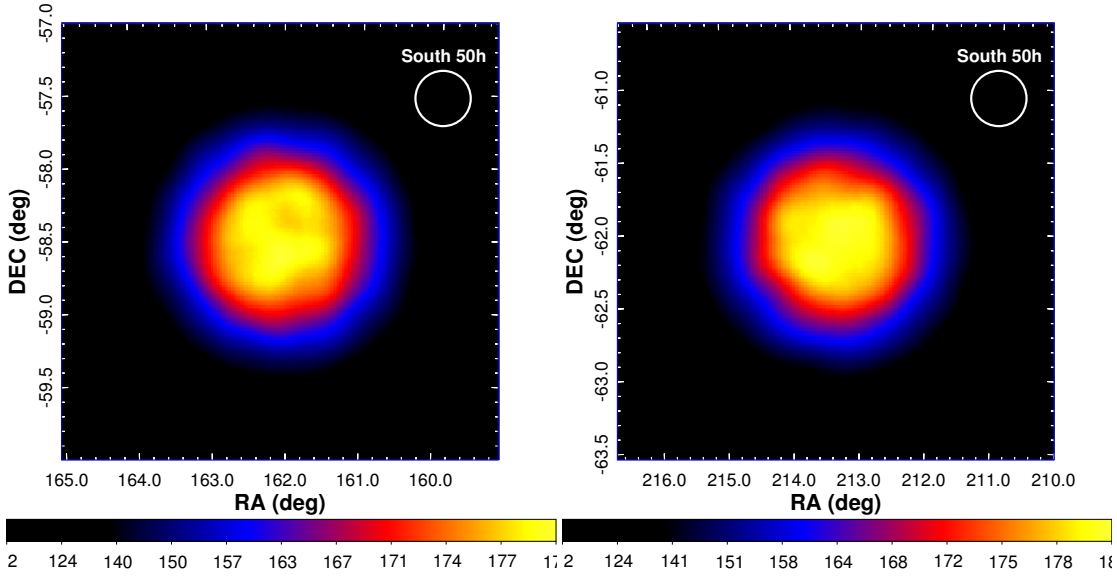

(C) PSR J1048−5832. (D) PSR J1413−6205.

FIGURE 2.9: Same as Fig. 2.8 for PSRs J0835−4510, J1028−5819, J1048−5832 and J1413−6205. For PSR J0835−4510, the exposure time is 25 hours and also the PWN emission is included in the simulation.

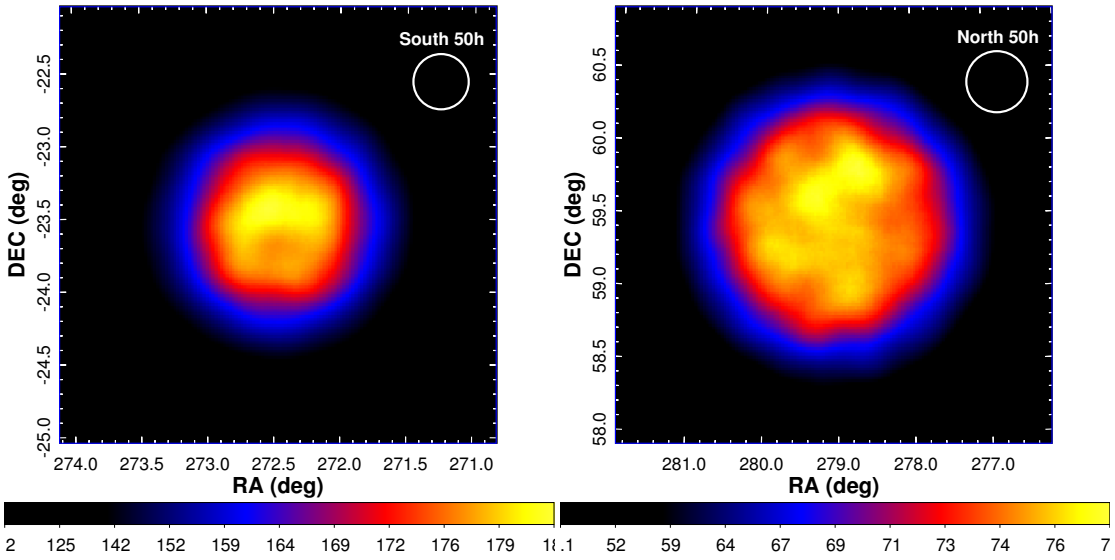

(A) PSR J1809−2332. (B) PSR J1836+5925 with OP emission.

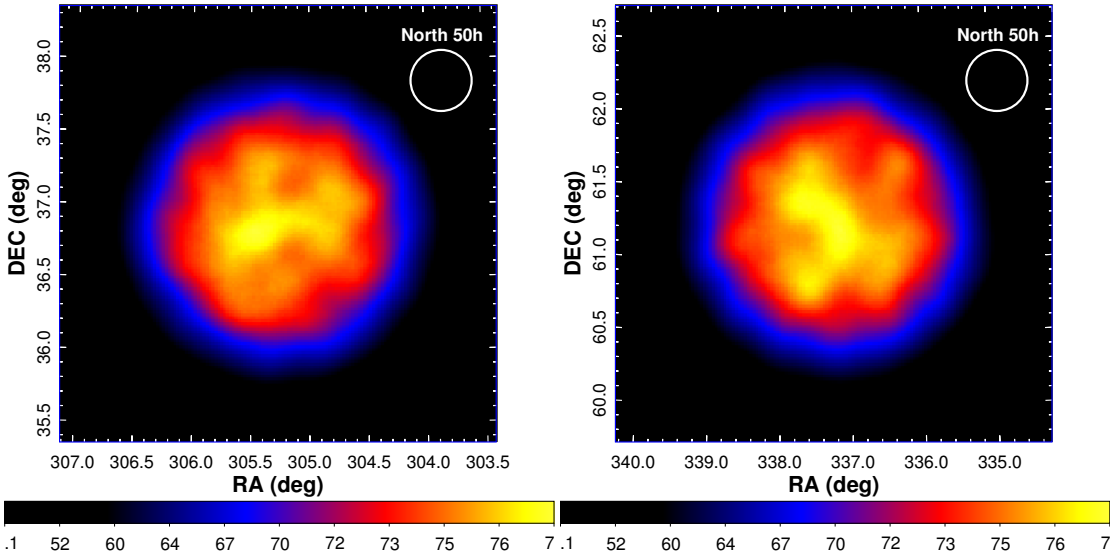

(C) PSR J2021+3651. (D) PSR J2229+6114.

FIGURE 2.10: Same as Fig. 2.8 for PSRs J1809−2332, J1836+5925, J2021+3651 and J2229+6114. PSR J1836+5925 is shown together with OP emission.

Chapter 3

Investigating the Crab Pulsar Gamma-Ray Pulse Profile with the Cherenkov Telescope Array

The Crab pulsar is one of the most well studied gamma-ray pulsars in our Galaxy and is also detected at VHE. One of the important tool that can constrain theoretical models of pulsar emission is the timing analysis. In addition to investigating the Crab pulsar spectrum and/or the shape of its light curve in gamma rays studying its timing properties at VHE can shed light on the location of the acceleration region and the mechanism of gamma-ray emission from the neutron star.

In this chapter I present a detailed analysis of the VHE gamma-ray emission from the Crab pulsar, simulating the VHE light curve which will be observed with CTA.

3.1 Gamma-ray Emission from the Crab Pulsar

The Crab pulsar (PSR J0534+2201) was the first pulsar to be detected by Cherenkov telescopes at VHE gamma rays above a few tens of GeV (e.g. [96, 99, 112, 180]). It is the compact remnant of a supernova, which exploded approximately 1000 years ago at a distance of about 2 kpc from the Sun. The magnetic field of the pulsar is 3.8×10^{12} G, its rotational period ∼33.62 ms, and its spin-down power $\sim 4.6 \times 10^{38}$ erg s^{-1} [84]. The Crab pulsar is detected at all wavelengths from radio to TeV gamma rays.

As mentioned in Chapter 2, the gamma-ray spectrum (100 MeV – 100 GeV) of the Crab pulsar can be described by the power law with exponential cut-off [10] (see Eq. (2.2)). However, less steep spectral shape was observed at energies >10 GeV (see [12]). The

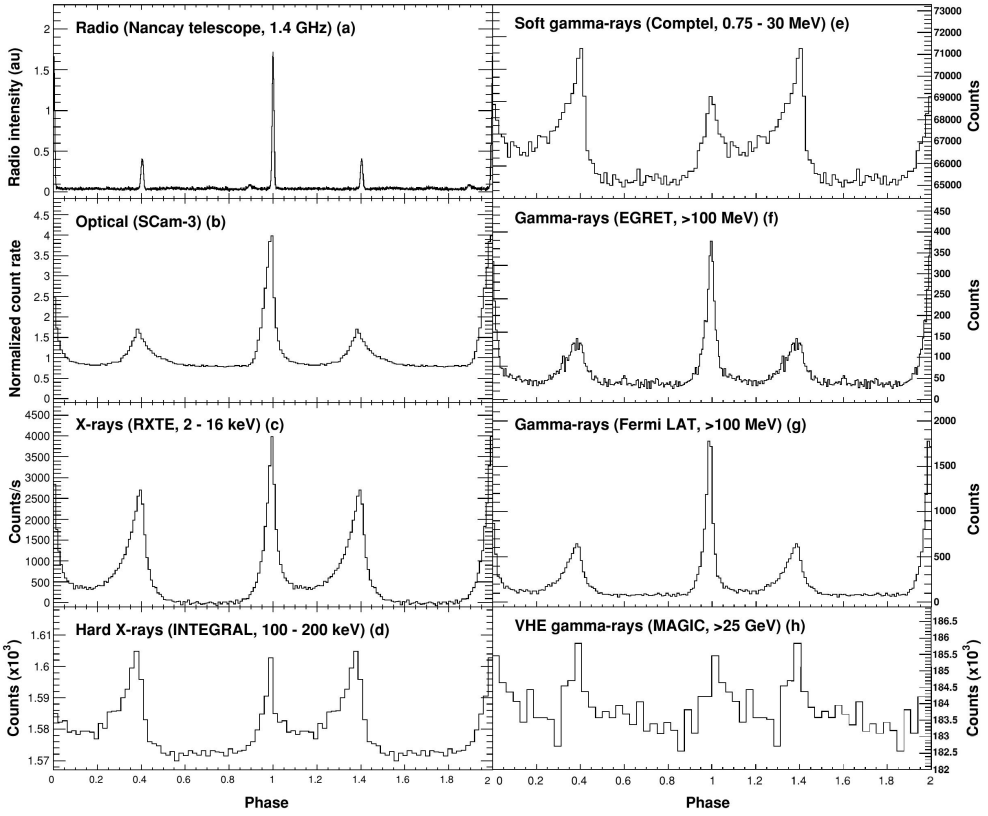

FIGURE 3.1: Light curves of the Crab pulsar at different wavelengths. References: (a) Nançay radio telescope; (b) Oosterbroek et al. [181]; (c) Rots et al. [182]; (d) Mineo et al. [183]; (e) Kuiper et al. [184]; (f) Kuiper et al. [184]; (g) Abdo et al. [10]; (h) Aliu et al. [112]. (Image taken from [10]).

VHE observations of e.g. MAGIC [98] and VERITAS [99] proved the absence of the cut-off up to few TeV and ∼400 GeV, respectively.

Investigating the pulse profile of pulsars in different energy bands is important in order to fully understand the physical mechanisms responsible for accelerating particles to relativistic energies. The diverse of shapes of the Crab pulsar light curves in different energy bands is shown in Fig. 3.1. Several groups have studied the pulse profile of the Crab pulsar at different energies. The timing properties in the radio band were investigated with a number of radio telescopes, including the Nançay French telescope [185] and the Jodrell Bank Observatory [186]. Some of the most accurate optical observations of the Crab pulsar, with time resolutions of hundreds of picoseconds, were recently carried out with the Copernico Telescope in Asiago [187] and the New Technology Telescope in La Silla [188]. Detailed X-ray pulse profiles were obtained with the Rossi X-ray Timing Explorer (RXTE) [182] as well as with *Suzaku* [189], *Swift* [190] and *XMM-Newton* [191]. Hard X-ray (100–200 keV) and soft gamma-ray (0.75–30 MeV) observations were carried out with INTEGRAL [183] and COMPTEL [184], respectively. Gamma-ray (>100 MeV) observations were performed by AGILE [192] and the *Fermi*-LAT [10]. Finally, recent

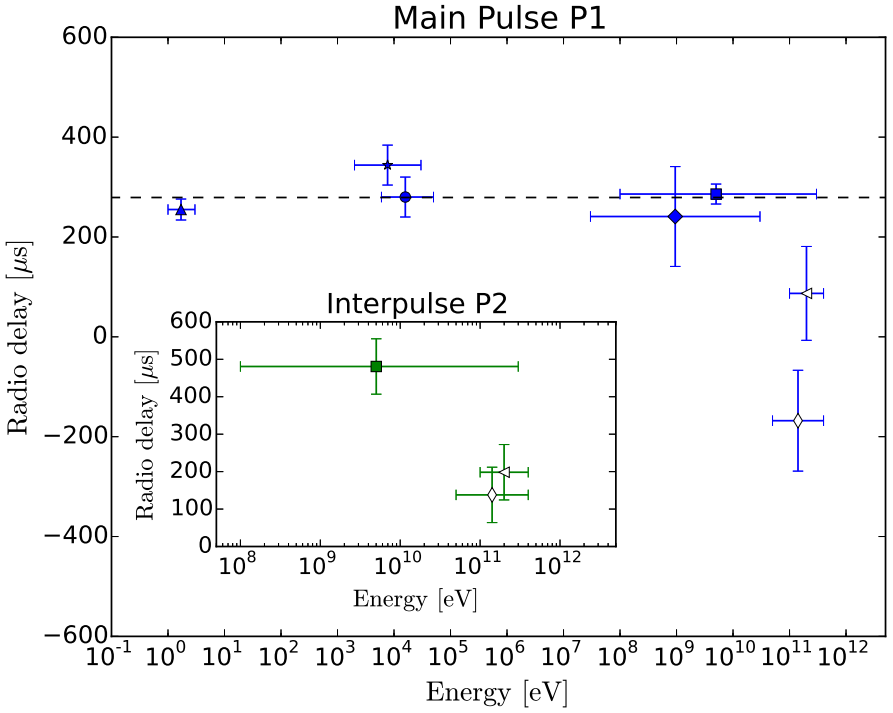

FIGURE 3.2: Time shift (radio delay in μs) between the main pulse (P1) and interpulse (P2, inset) of the Crab pulsar light curve at radio wavelengths and at higher energies. Markers correspond to the observations performed in different energy ranges (triangles – optical [181], stars – X-rays (RXTE [182]), circles – X-rays (INTEGRAL [193]), diamonds – gamma rays (EGRET [193]), squares – gamma rays (*Fermi*-LAT [10]), thin diamonds – VHE gamma rays (MAGIC [96]), rotated triangles – VHE gamma rays (VERITAS [99]). Horizontal error-bars correspond to the energy range of an observation. Dashed line is the radio delay averaged over the optical, X-ray and gamma-ray measurements, without considering the two VHE gamma-ray observations. (Image taken from [194]).

observations with ground based Cherenkov telescopes, such as MAGIC [96, 97, 118] and VERITAS [99], have obtained pulse profiles of the Crab pulsar in VHE gamma rays.

MAGIC and VERITAS observations show that the amplitude of the main pulse of the Crab pulsar is lower than the amplitude of the interpulse contrary to what is observed at lower energies with the *Fermi*-LAT. There are also some peculiarities of timing properties of the Crab pulsar at VHE. As it is shown in Fig. 3.2, the radio pulses arrive to the observer with some delay as compared to those in higher energy ranges (optical, X-ray, gamma-ray). The average value of this delay is about 280 μs (dashed line in Fig. 3.2), which is not consistent what found at VHE. Furthermore, the main pulse (P1) is leading the radio according to VERITAS [99], but lagging it according to MAGIC (most probably because of uncertainties caused by the low statistics of the main peak [96]). Analogous calculations performed for the interpulse (P2) also show a difference in phase shift for the *Fermi*-LAT and MAGIC/VERITAS observations (inserted in Fig. 3.2).

Although there is still no comprehensive theory that can describe the overall emission properties of the Crab pulsar, VHE observations with currently operating IACTs and particularly with the next-generation CTA facility can constrain significantly the parameters of emission models: e.g. a cut-off energy of the gamma-ray spectrum, a value of the radio delay at energies >100 GeV [8, 14].

The prospects for the spectral investigations of the Crab pulsar with CTA are reported in [120]. The unprecedented sensitivity achievable with this instrument prompted to perform a quantitative investigation of the pulse shape and timing of the Crab pulsar at VHE attainable with the CTA observatory. To estimate the impact of CTA, various simulations were performed for different array configurations and exposure times.

3.2 VHE Pulse Profile of the Crab Pulsar

The Crab pulsar region has been observed with several VHE telescopes (H.E.S.S., [20, 21]; HEGRA, [195]; Whipple, [1, 196]; CAT, [197]; MAGIC, [9, 96, 97]; VERITAS, [99]). For the sake of comparison, in the following I will consider as reference the observations carried out with the two MAGIC telescopes located in La Palma during the period between the winter season 2009/2010 and that of 2010/2011 [96]. The energy range is 50–400 GeV. A light curve was obtained by phase folding approximately 73 hours of observations and is shown in Fig. 3.3.

The light curve can be quite reasonably reproduced by the sum of Gaussian functions plus a constant. Two Gaussian components corresponded to the pulsar peaks (P1 and P2) provide rather accurate fit with a reduced χ^2 of 1.18 (see Fig 3.3A). An additional third Gaussian (with negative amplitude) gives a significant improvement of the fit in the off-pulse phase interval between 0.52 and 0.87. The adopted fitting function written as a function of phase ϕ is:

$$I(\phi) = \sum_{i=1}^{3} k_i G_{m_i,s_i}(\phi) + C\,, \tag{3.1}$$

where $G_{m_i,s_i}(\phi) = 1/(\sqrt{2\pi}s_i)\exp[-(\phi - m_i)^2/(2s_i^2)]$ is a Gaussian function with mean m_i, standard deviation s_i, and normalization k_i (Table 3.1), while the constant C accounts for the background. Taking m_i, s_i, k_i and C as free parameters, the MAGIC pulse profile is well fitted by Eq. (3.1) with a reduced χ^2 of 1.07. Hereafter, I fix the values of the parameters obtained from the fit and use them in the simulations of pulse profile of the Crab pulsar as would be observed with CTA.

TABLE 3.1: Parameters of the fitting function I, given by the sum of three Gaussians and a constant. The mean, standard deviation and normalization of the Gaussians are reported in the first, second and third column, respectively. The value of C is listed in the forth row.

i	m_i	s_i	k_i
1	0.389 ± 0.002	0.012 ± 0.002	14 ± 2
2	1.01 ± 0.02	0.04 ± 0.02	12 ± 7
3	0.76 ± 0.09	0.16 ± 0.13	-23 ± 22
$C = (2.24 \pm 0.01) \times 10^3$			

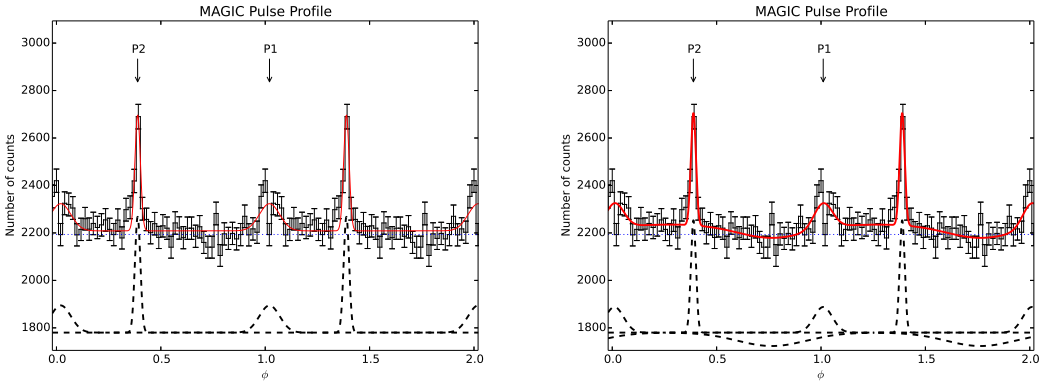

(A) (B)

FIGURE 3.3: MAGIC 50–400 GeV pulse profile of the Crab pulsar [96], along with the 2-Gaussian (A) and 3-Gaussian (B) fitting functions (red solid lines). The black dashed lines represent the Gaussian components of I, while the blue dotted line is the background level. P1 and P2 are the main pulse and interpulse, respectively. The adopted number of bins per period is 51.

To simulate the pulse profile observed with a CTA-like instrument I calculate the background level $I_{\rm BG}^{\rm M}$ of the MAGIC data in the off-pulse region from phase 0.52 to 0.87 and subtract it from the fitted profile I. Then, the profile I is rescaled according to the different effective area $A_{\rm eff}$ of the CTA configurations and to the different observation durations $t_{\rm obs}$. I also assume that the pulse shape does not strongly depend on energy between 0.01 TeV and ∼100 TeV, which allows us to rescale the profile with the number of counts in different spectral bands. Although there is some evidence of evolution of the pulse shape in gamma rays (see e.g. [97]), this appears to be in the direction of increasing the significance of the interpulse (with respect to the main pulse). Thus, the actual detection of the interpulse with CTA, which will be considered below, may in fact be more significant, and estimates presented here can then be regarded as conservative. To determine the rescaling factor, an estimate of the energy spectrum in the CTA energy range is clearly needed. This introduces the major source of uncertainty in the present calculation.

Assuming that $F(E)$ is an appropriate representation of the actual phase-averaged pulsar

spectrum in the CTA energy range, the pulse shape can then be rescaled according to the following expression:

$$I^{'} = I \times \frac{\int_{E_{\rm min}}^{E_{\rm max}} F(E)\, A_{\rm eff}(E)\, t_{\rm obs}\, {\rm d}E}{\int_{E_{\rm min}^{\rm M}}^{E_{\rm max}^{\rm M}} F_{\rm M}(E)\, A_{\rm eff}^{\rm M}(E)\, t_{\rm obs}^{\rm M}\, {\rm d}E}, \tag{3.2}$$

where $F(E)$ ($F_{\rm M}(E)$) is the CTA (MAGIC) spectrum, $E_{\rm min}$ ($E_{\rm min}^{\rm M}$) and $E_{\rm max}$ ($E_{\rm max}^{\rm M}$) bracket the corresponding energy range, $A_{\rm eff}$ ($A_{\rm eff}^{\rm M}$) and $t_{\rm obs}$ ($t_{\rm obs}^{\rm M} = 72.78$ hours) are the effective area and corresponding observing time in the CTA (MAGIC) configuration. The rescaling factor (the ratio of the two integrals) is determined by comparing the number of counts of the simulated configuration with that of MAGIC. The calculation is done adopting effective areas for similar zenith angles (20° for CTA and VERITAS, averaged below 30° for MAGIC).

For $F(E)$ a power law is assumed:

$$F(E) = \frac{{\rm d}N}{{\rm d}E} = N_0 \times \left(\frac{E}{0.1\ {\rm TeV}}\right)^{-\Gamma}, \tag{3.3}$$

where N_0 and Γ are the normalization and spectral index, respectively. The values of N_0 and Γ are taken from Aleksić et al. [96]: $N_0 = (13.0 \pm 1.6) \times 10^{-11}$ TeV^{-1} cm^{-2} s^{-1} and $\Gamma = 3.57 \pm 0.27$[1]. I do not use values from the more recent work by MAGIC Collaboration et al. [118] because I need phase-averaged spectral parameters, while their analysis refers only to the peak emission.

Another parameter required to estimate the actual light curve observed with CTA is the background emission, which is generally dominated by the Crab Nebula rather than by backgrounds particles (hadrons, electrons and diffuse gamma rays). I determine it by adopting a simplified approach, similar to that outlined above for rescaling the source counts since, at CTA resolution, both the pulsar and surrounding nebula can be considered as point-sources. Assuming that the VHE emission from the Crab Nebula dominates over the cosmic-ray background up to the ∼100 TeV, the background is obtained by re-normalizing the counts of the Nebula spectrum in the different energy ranges (similar to Eq. (3.2)):

$$I_{\rm BG} = I_{\rm BG}^{\rm M} \times \frac{\int_{E_{\rm min}}^{E_{\rm max}} F_{\rm BG}(E)\, A_{\rm eff}(E)\, t_{\rm obs}\, {\rm d}E}{\int_{E_{\rm min}^{\rm M}}^{E_{\rm max}^{\rm M}} F_{\rm BG}(E)\, A_{\rm eff}^{\rm M}(E)\, t_{\rm obs}^{\rm M}\, {\rm d}E}, \tag{3.4}$$

where $I_{\rm BG}^{\rm M}$ is the MAGIC background, measured in the off-pulse region from phase 0.52 to 0.87 (blue dotted line in Fig. 3.3B; [96]). For the nebular spectrum $F_{\rm BG}(E)$, I used

[1] Only statistical errors are quoted.

the log-parabola approximation from [9]:

$$F_{\rm BG}(E) = (3.23 \pm 0.03) \times 10^{-11} \times \\ \times \left(\frac{E}{1\,\mathrm{TeV}}\right)^{-(2.47\pm0.01)-(0.24\pm0.01)\log(E/1\,\mathrm{TeV})} \mathrm{TeV}^{-1}\mathrm{cm}^{-2}\mathrm{s}^{-1}\,. \quad (3.5)$$

The instrumental noise is not taken into account because it is much lower than the emission from the nebula.

Summarizing, I generate the simulated pulse profile I_s detected by CTA using the following procedure:

1. I approximate the pulse profile of the Crab pulsar with the fitting function I (Eq. (3.1) and Fig. 3.3B).
2. I then calculate the MAGIC background level $I_{\rm BG}^{\rm M}$ in the off-pulse region from phase 0.52 to 0.87 and subtract it from the pulse profile I. With this value the rescaled pulse shape $I^{'}$ is computed from Eq. (3.2).
3. I calculate the CTA background level $I_{\rm BG}$ from Eq. (3.4) and add it to the pulse profile $I^{'}$.
4. Stochastic properties are added to the pulse shape $I^{'}$ to produce the final simulated signal I_s. The simulated pulse profile in the i-th bin, $I_{s,i}$, is considered to be a random value following a Gaussian distribution with mean value equal to $I^{'}$ and standard deviation equal to $\sqrt{I^{'}}$. The error in each bin is the square root of the number of counts in that bin, $\sqrt{I_{s,i}}$. An example of the final simulated pulse profile is shown in Fig. 3.4.

3.3 CTA and the ASTRI Mini-array Configurations

Simulated pulse profiles of the Crab pulsar were computed for different CTA arrays. Here I consider standard sub-arrays, which consist of telescopes of different size (LSTs, MSTs and SSTs) distributed according to the conservative MC-Prod1 configurations (from [151]) and to the recent second-generation MC-Prod2 configurations.

MC-Prod1 Confs. NA and NB refer to the possible configurations of the northern CTA installation, whereas Confs. A through K correspond to those of CTA-South.

In addition, sub-arrays of Conf. I with identical types of telescopes, such as Large Size Telescopes (Conf. I-LST), Medium Size Telescopes (Conf. I-MST) and Small Size

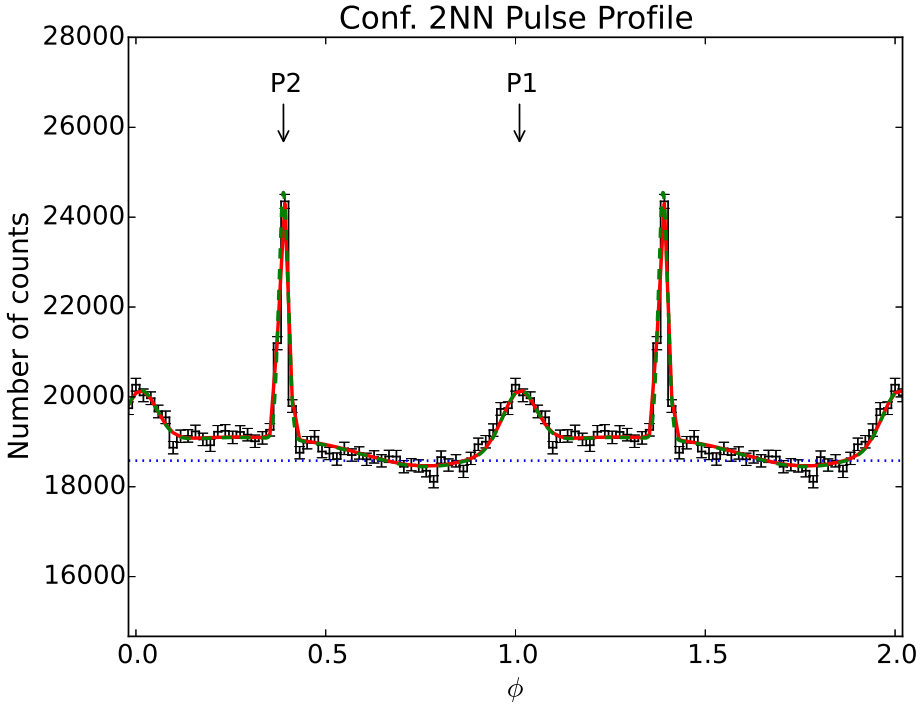

FIGURE 3.4: Simulated (I_s, black histogram) and assumed CTA pulse profile ($I^{'}$, red line) of the Crab pulsar detected by Conf. 2NN during an observation with duration $t^{\mathrm{M}}_{\mathrm{obs}} = 72.78$ hours and using 51 bins per period. The green dashed line is a best fit with three Gaussians of the simulated pulse profile. The blue dotted line is the background level. P1 and P2 represent the main pulse and interpulse, respectively.

Telescopes (Conf. I-SST) are of great interest and are then also included. SSTs of 7-meter diameter are used in all MC-Prod1 arrays. The adopted configurations and their properties are listed in Table 3.2.

Within the framework of the MC-Prod2 package[2], I consider Confs. 2NN, 2Nb, 2Nc, 2Nd, 2Ne and 2Nf as representatives of the northern CTA installation. The sub-arrays of Conf. 2NN with identical types of telescopes are also included: Confs. 2NN-LST (or LST-array) and 2NN-MST (or MST-array). In addition, I perform simulations for possible configurations of the CTA-South installation such as Confs. 2b, 2c and 2e. SSTs of 4-meter dishes are used in all these MC-Prod2 configurations. Finally, I use Conf. s9-4-257m – a distribution of 9 identical 4-meter SSTs with a separation of 257 meters – as an appropriate representation of the ASTRI mini-array. The properties of corresponding MC-Prod2 arrays as well as those of MAGIC and VERITAS are listed in Table 3.3.

The effective areas $A_{\mathrm{eff}}(E)$ and energy ranges (E_{min}, E_{max}) needed for the convolution with the source and background spectra (Eqs. (3.2) and (3.4)) are inferred from the

[2]Monte Carlo Prod2 DESY (Sep 2014) package for the cite "Leoncito++" available at http://www.cta-observatory.org/ctawpcwiki/index.php/WP_MC#Interface_to_WP_PHYS.

TABLE 3.2: Configurations of MAGIC, VERITAS and MC-Prod1 sub-arrays of CTA.

Name	Telescopes	Energy range (TeV)	E_{thr} (TeV)	$\langle A_{\mathrm{eff}} \rangle_{\mathrm{sp}}$ [$10^5 \times \mathrm{m}^2$]
MAGIC	2×17 m	0.05–0.4	0.072	0.07
VERITAS	4×12 m	0.1–0.4	0.136	0.28
Conf. I-LST	3 LST	0.02–118	0.033	0.04
Conf. I-MST	18 MST	0.06–269	0.131	0.15
Conf. I-SST	56 SST	0.15–272	0.327	0.51
Conf. A	3 LST 41 MST	0.02–126	0.050	0.05
Conf. B	5 LST 37 MST	0.02–126	0.032	0.06
Conf. C	29 MST 26 SST	0.05–126	0.126	0.15
Conf. D	41 MST 16 SST	0.05–126	0.126	0.34
Conf. E	4 LST 23 MST 32 SST	0.02–126	0.032	0.06
Conf. F	6 LST 29 MST	0.02–126	0.032	0.06
Conf. G	6 LST 9 MST 16 SST	0.02–126	0.032	0.06
Conf. H	25 MST 48 SST	0.05–126	0.079	0.19
Conf. I	3 LST 18 MST 56 SST	0.02–126	0.032	0.05
Conf. J	3 LST 30 MST 16 SST	0.02–126	0.032	0.05
Conf. K	5 LST 72 SST	0.02–126	0.032	0.07
Conf. NA	4 LST 17 MST	0.02–126	0.032	0.06
Conf. NB	3 LST 17 MST 8 SST	0.02–126	0.032	0.04

For all CTA configurations the number of telescopes is taken from [151]. LST: Large Size Telescope with diameter 24 m. MST: Medium Size Telescope with diameter 12.3 m. SST: Small Size Telescope with diameter 7 m. The energy ranges for all these configurations are taken from the corresponding IRFs, while those of MAGIC and VERITAS correspond to the energies, at which the Crab pulsar spectrum was measured (see [96, 99]). E_{thr} is the energy threshold, while $\langle A_{\mathrm{eff}} \rangle_{\mathrm{sp}}$ is the spectrum-weighted effective area of each configuration.

TABLE 3.3: Configurations of MAGIC, VERITAS and MC-Prod2 sub-arrays of CTA, including the ASTRI mini-array.

Name	Telescopes	Energy range (TeV)	$E_{\rm thr}$ (TeV)	$\langle A_{\rm eff}\rangle_{\rm sp}$ [$10^5 \times {\rm m}^2$]
MAGIC	2×17 m	0.05–0.4	0.072	0.07
VERITAS	4×12 m	0.1–0.4	0.136	0.28
LST-array	4 LST	0.04–158	0.040	0.49
MST-array	14 MST	0.1–158	0.158	0.71
Mini-array	9 SST	1.6–158	3.981	0.71
Conf. 2NN	4 LST 14 MST	0.04–158	0.040	0.53
Conf. 2Nb	4 LST 14 MST	0.04–100	0.040	0.53
Conf. 2Nc	4 LST 10 MST 10 SST	0.04–158	0.040	0.53
Conf. 2Nd	3 LST 12 MST	0.03–100	0.040	0.53
Conf. 2Ne	3 LST 12 MST	0.04–100	0.040	0.53
Conf. 2Nf	4 LST 10 MST	0.04–100	0.040	0.53
Conf. 2b	3 LST 18 MST 72 SST	0.04–158	0.040	0.24
Conf. 2c	3 LST 32 MST 38 SST	0.04–158	0.040	0.26
Conf. 2e	4 LST 24 MST 72 SST	0.04–158	0.040	0.50

Confs. 2NN, 2Nc, 2Ne, 2Nb, 2Nd, 2Nf are representatives of the northern CTA installation. Confs. 2b, 2c and 2e refer to CTA-South. All these arrays are taken from the MC-Prod2 DESY simulation package (http://www.cta-observatory.org/ctawpcwiki/index.php/WP_MC#Interface_to_WP_PHYS). LST: Large Size Telescope with diameter 23 m. MST: Medium Size Telescope with diameter 12 m. SST: Small Size Telescope with diameter 4 m. As the best representation for the ASTRI mini-array (Mini-array), I consider a configuration of 9 SST from the same MC-Prod2 simulations (Conf. s9-4-257m). The energy ranges for all these configurations are taken from the corresponding IRFs, while those of MAGIC and VERITAS correspond to the energies at which the Crab pulsar spectrum was measured (see [96, 99]). $E_{\rm thr}$ is the energy threshold, while $\langle A_{\rm eff}\rangle_{\rm sp}$ is the spectrum-weighted effective area of each configuration.

IRFs[3] and are reported in Tables 3.2 and 3.3. They are calculated from the simulations of 50-hour observations of a 1 Crab Unit[4] source at a 20° zenith angle and with a sensitivity averaged over north and south pointings (latter – for MC-Prod2 simulations). For the effective areas of MAGIC ($A_{\rm eff}^{\rm M}(E)$) and VERITAS ($A_{\rm eff}^{\rm V}(E)$) I adopt published values from [135] and [198], while for the corresponding energy ranges, in which the Crab pulsar spectra were measured, I refer to [96] and [99].

In Tables 3.2 and 3.3 I report also the threshold energy $E_{\rm thr}$ and the spectrum-weighted effective areas $\langle A_{\rm eff}\rangle_{\rm sp}$ for each configuration. The former is the energy at which the product of the effective area by the source spectrum $F(E)$ peaks, while the latter is defined as:

$$\langle A_{\rm eff}\rangle_{\rm sp} = \frac{\int_{E_{\rm min}}^{E_{\rm max}} A_{\rm eff}(E)F(E){\rm d}E}{\int_{E_{\rm min}}^{E_{\rm max}} F(E){\rm d}E}\,. \tag{3.6}$$

The values of $E_{\rm thr}$ for MAGIC and VERITAS are consistent with the corresponding after-cuts values reported in [135] and [99], respectively.

3.4 Results

Simulated pulse profiles for each CTA array configuration are computed as described in Sect. 3.2 and are then fitted with the model function in Eq. (3.1). An example of such a calculation is shown in Fig. 3.4 for CTA Conf. 2NN.

An important quantity to constrain the parameters (e.g. the height and location of the emission region) of pulsar models is the difference in the time of arrival of the peaks in different energy bands (e.g. [8, 181]). At optical wavelengths (see [199, 200]) it was found a radio delay between the time of arrival of the optical and radio peaks of the order of 100 μs with an uncertainty of a few tens of microseconds, whereas no delay (-60 ± 50 μs) was reported in [201]. While a secular change of this delay may be possible, within measurement uncertainties present observations appear to give delays consistently of the order of ∼150-250 μs, with the optical leading the radio (e.g. [181, 188]).

Measuring an accurate time differences at VHE requires not only a precise time stamp (in CTA it will be of the order of ns), but also a good signal to noise ratio, or in other words good sensitivity. To check how well CTA can measure the peak positions with different observing times, I determined the position of the interpulse P2 and its error (Δ_2) for the different CTA sub-arrays considered here. The value of the uncertainty

[3] IRFs of MC-Prod1 configurations are taken from http://www.mpi-hd.mpg.de/hfm/CTA/MC/performance-20deg/. Those of MC-Prod2 – from http://www.cta-observatory.org/ctawpcwiki/index.php/WP_MC#Interface_to_WP_PHYS

[4] 1 Crab Unit = $2.79 \times 10^{-11} \times (E/1\ {\rm TeV})^{-2.57}$ cm^{-2} s^{-1} TeV^{-1}.

Δ_2 clearly affects the accuracy with which it will be possible to perform this type of measurement.

3.4.1 CTA MC-Prod1 Configurations

Results for MC-Prod1 are shown in Fig. 3.5. For each configuration I repeated the simulations several times and then computed the average Δ_2 and its statistical uncertainty (standard deviation). As it can be seen from Fig. 3.5, the accuracy of the pulse shape attainable with the full-energy-range Conf. I, which contains all three types of telescopes, is such that even rather short observations (several hours; triangles) are sufficient to measure the position of the interpulse rather accurately. As a consistency check, I also simulated the MAGIC and VERITAS pulse profiles using the VHE spectra from [96] and [99], respectively. The simulated 73-hour MAGIC observations give results consistent with those of the real 73-hour observation ($\Delta_2 = 60 \pm 9$ μs versus $\sim$50 μs). Similar conclusions are reached for the simulations of the 110-hour VERITAS observations ($\Delta_2 = 90 \pm 20$ μs versus $\sim$70 μs).

It was also found that observations of short-duration with VERITAS ($0.1 \times t^{\mathrm{M}}_{\mathrm{obs}}$), Conf. C ($0.1 \times t^{\mathrm{M}}_{\mathrm{obs}}$), the Conf. I-MST ($0.1 \times t^{\mathrm{M}}_{\mathrm{obs}}$) and the Conf. I-SST ($0.1 \times t^{\mathrm{M}}_{\mathrm{obs}}$, $0.3 \times t^{\mathrm{M}}_{\mathrm{obs}}$, $1 \times t^{\mathrm{M}}_{\mathrm{obs}}$) are not sufficient to detect significant pulsations. Indeed, in all these cases the energy threshold is much higher than that of MAGIC.

3.4.2 CTA MC-Prod2 Configurations

MC-Prod2 results obtained for Conf. 2NN, the LST-array, the MST-array and Conf. 2e are shown in Fig. 3.6. As mentioned in Sect. 3.4.1, for each configuration I computed the average Δ_2 and its statistical uncertainty. The accuracy of the pulse shape attainable with CTA-North Confs. 2NN or CTA-South Conf. 2e (triangles in Fig. 3.6) is comparable to that of MC-Prod1 Conf. I.

In addition to the array configurations listed above, I repeated the simulations for different energy ranges of Conf. 2NN and also for other CTA configurations, such as Confs. 2Nc, 2Ne, 2Nb, 2Nd, 2Nf – representatives of the northern CTA installation –, and Confs. 2b, 2c – possible layouts of CTA-South. Results are reported in Fig. 3.7.

Similarly to the MC-Prod1 simulations, the observations of short-duration with VERITAS ($0.1 \times t^{\mathrm{M}}_{\mathrm{obs}}$), the MST-array ($0.1 \times t^{\mathrm{M}}_{\mathrm{obs}}$) and Conf. 2NN in the 1–10 TeV energy range ($0.1 \times t^{\mathrm{M}}_{\mathrm{obs}}$, $0.3 \times t^{\mathrm{M}}_{\mathrm{obs}}$, $1 \times t^{\mathrm{M}}_{\mathrm{obs}}$, $1.5 \times t^{\mathrm{M}}_{\mathrm{obs}}$, $3 \times t^{\mathrm{M}}_{\mathrm{obs}}$) are not sufficient to detect significant pulsations. Simulations performed for the high-energy-range arrays containing only

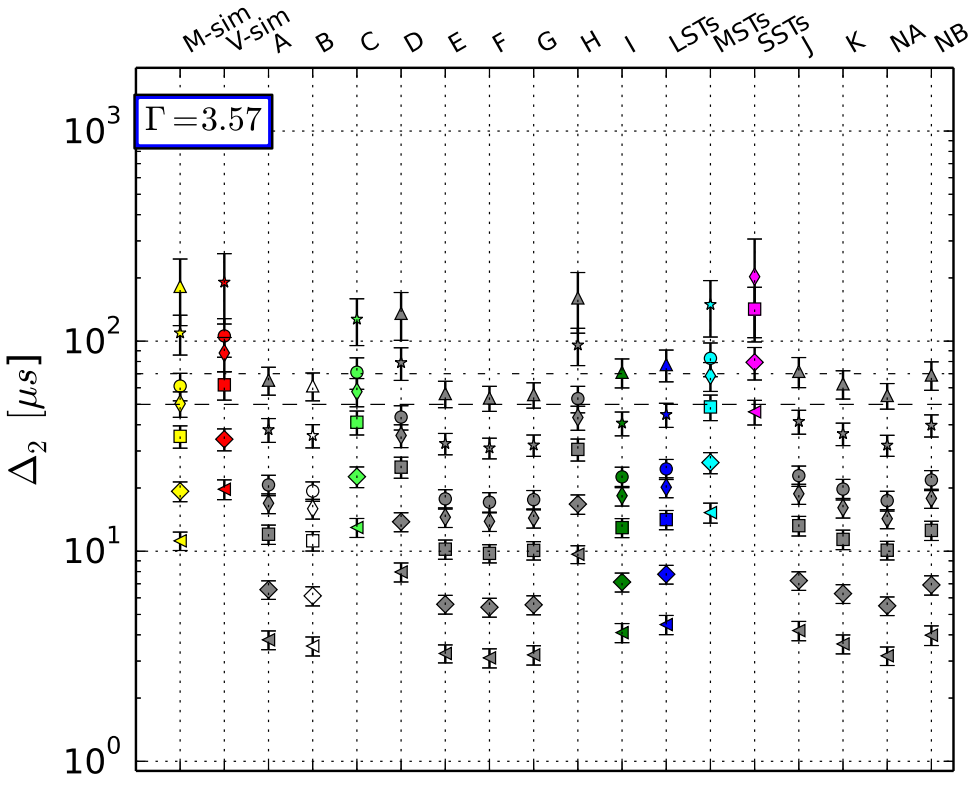

FIGURE 3.5: Uncertainty in the position of the interpulse P2 (Δ_2) of the VHE profile of the Crab pulsar, simulated for several CTA MC-Prod1 configurations. The spectral index of the Crab pulsar spectrum used in these simulations is Γ=3.57 (see Sect. 3.2). Results for MAGIC (yellow, M-sim), VERITAS (red, V-sim) and different CTA MC-Prod1 instrumental configurations (blue Conf. I-LST (LSTs), cyan Conf. I-MST (MSTs), white Conf. B, magenta Conf. I-SST (SSTs), green Conf. I, light green Conf. C and grey other sub-arrays) are shown. Different markers correspond to observations of different durations in units of the MAGIC observing time ($t^{\rm M}_{\rm obs}$ = 72.78 hours): 0.1 (triangles), 0.3 (stars), 1 (circles), 1.5 (thin diamonds), 3 (squares), 10 (diamonds), 30 (rotated triangles). Error-bars represent the standard deviation calculated from a set of simulations. The dashed and dotted-dashed lines show the uncertainties of the MAGIC ($\Delta_2 = 50$ μs [96]) and VERITAS ($\Delta_2 = 70$ μs [99]) observations, respectively.

4-meter SSTs (e.g. ASTRI mini-array) with $E_{\rm thr} > 1$ TeV yield no detection of pulsations even for very long observing times ($30 \times t^{\rm M}_{\rm obs}$) and, therefore, are not shown in Fig. 3.6. For the ASTRI mini-array significant pulsations are detected only for unrealistically long observing times of more than $\sim 10^6$ hours.

I investigated the possibility of measuring an energy dependent shift in the position of the interpulse with different CTA sub-arrays. In particular, I study whether it would be possible to measure phase shifts in the pulse profile among arrays made entirely by different types of telescopes (LSTs, MSTs, SSTs), which are most sensitive in the different energy ranges. This measurement is feasible in ∼73 hours with the LSTs and MSTs, but not with the SSTs (because of the larger amount of time required for such array to detect pulsations, see Sect. 3.5 for details). The uncertainty in measuring the

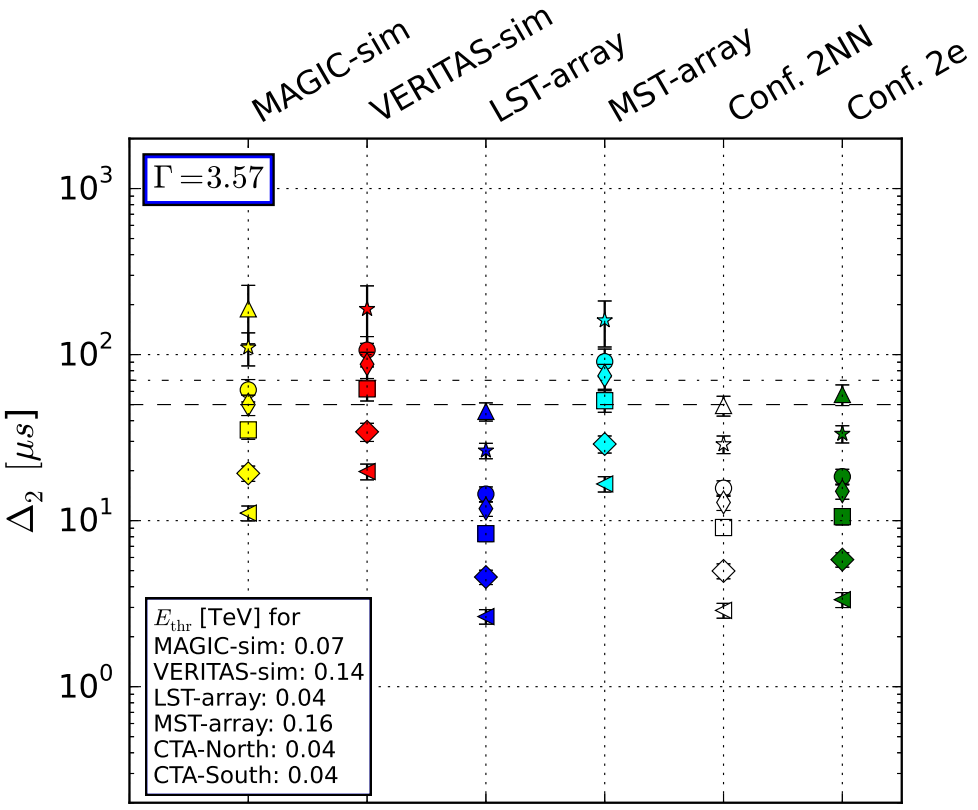

FIGURE 3.6: Uncertainty in the position of the interpulse P2 (Δ_2) of the VHE profile of the Crab pulsar, simulated for MC-Prod2 Conf. 2NN (white) and for Conf. 2e (green). Results for MAGIC (yellow), VERITAS (red) and the CTA LST-array (blue) and MST-array are also shown. The spectral index of the Crab pulsar spectrum used in these simulations is Γ=3.57 (see Sect. 3.2). Different markers correspond to observations of different durations in units of the MAGIC observing time ($t^{\rm M}_{\rm obs}$ = 72.78 hours): 0.1 (triangles), 0.3 (stars), 1 (circles), 1.5 (thin diamonds), 3 (squares), 10 (diamonds), 30 (rotated triangles). Error-bars represent the standard deviation calculated from a set of simulations. The dashed and dotted-dashed lines show the uncertainties of the MAGIC ($\Delta_2 = 50$ μs [96]) and VERITAS ($\Delta_2 = 70$ μs [99]) observations, respectively.

position of the peak of the pulse profile with the LST- and MST- arrays is $\Delta_2 \sim 14$ μs and $\Delta_2 \sim 90$ μs, respectively (blue and cyan circles in Fig. 3.6). Therefore, the error on the measurement of the shift between the time of arrival of the LST and MST interpulses is about $\sqrt{14^2 + 90^2} \approx 90$ μs. Any potential phase shift larger than 3×90 μs (=270 μs) between the pulses measured at ∼40 GeV with the LSTs and at ∼100 GeV with the MSTs would be measurable in 73 hours at 3σ confidence level.

The Δ_2 values for both the MC-Prod1 and MC-Prod2 CTA configurations together with those simulated for MAGIC and VERITAS are shown in Table 3.4.

I also performed similar simulations for MC-Prod2 Confs. 2NN and 2e using different values of the spectral index Γ (3.0, 3.2, 3.5, 3.8) of the Crab pulsar. For each Γ I calculate the normalization factor N_0, stating that the flux in the energy range from 0.05 to 0.4

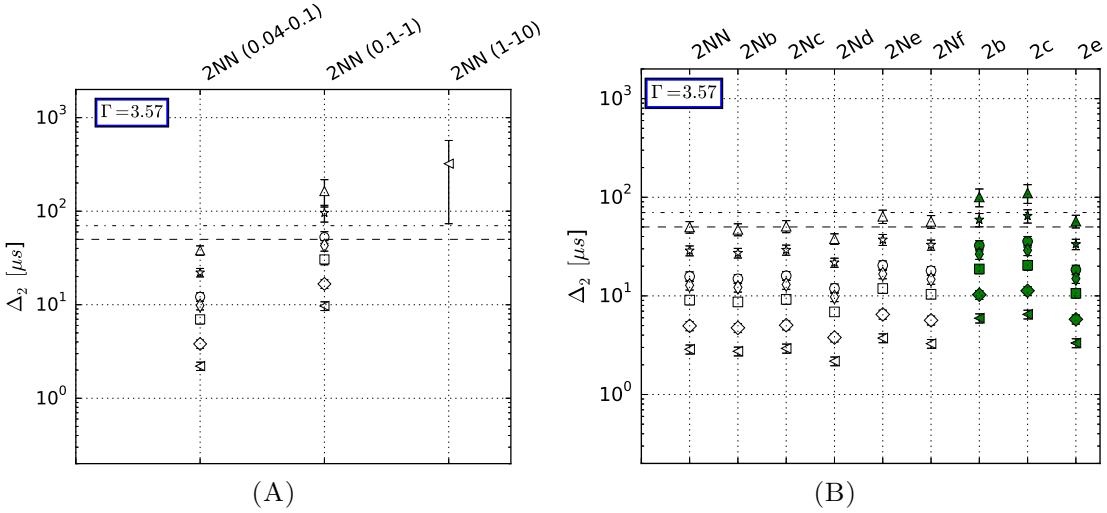

FIGURE 3.7: Same as Fig. 3.6 for different energy ranges of Conf. 2NN (A) and for other possible layouts of the MC-Prod2 CTA-North (Confs. 2NN, 2Nc, 2Ne, 2Nb, 2Nd and 2Nf in white) and CTA-South (Confs. 2b, 2c and 2e in green) installations (B).

TABLE 3.4: Uncertainty in the position of the interpulse P2 (Δ_2 μs) of the simulated VHE profile of the Crab pulsar, calculated for MAGIC, VERITAS and the different CTA instrumental configurations (both MC-Prod1 and MC-Prod2) shown in Figs. 3.5, 3.6 and 3.7. Columns refer to different observing times in units of the MAGIC observing time ($t^{\rm M}_{\rm obs}$ = 73 hours). The spectral index of the Crab pulsar spectrum used in the simulations is Γ=3.57 [96]. Error-bars represent the standard deviation calculated from a set of simulations. The results for the ASTRI mini-array are not shown because the time required for a significant detection is more than $30 \times t^{\rm M}_{\rm obs}$.

Name	$0.1 \times t^{\rm M}_{\rm obs}$	$0.3 \times t^{\rm M}_{\rm obs}$	$1 \times t^{\rm M}_{\rm obs}$	$1.5 \times t^{\rm M}_{\rm obs}$	$3 \times t^{\rm M}_{\rm obs}$	$10 \times t^{\rm M}_{\rm obs}$	$30 \times t^{\rm M}_{\rm obs}$
MAGIC-sim	190 ± 60	110 ± 20	60 ± 9	50 ± 7	35 ± 4	19 ± 2	11 ± 1
VERITAS-sim	-	190 ± 70	110 ± 20	90 ± 20	62 ± 10	34 ± 4	20 ± 2
Conf. I-LST	77 ± 13	45 ± 6	25 ± 3	20 ± 2	14 ± 1	7.8 ± 0.8	4.5 ± 0.5
Conf. I-MST	-	150 ± 40	80 ± 20	68 ± 11	49 ± 7	26 ± 3	15 ± 2
Conf. I-SST	-	-	-	200 ± 100	140 ± 40	79 ± 14	46 ± 6
Conf. A	65 ± 10	38 ± 5	21 ± 2	17 ± 2	12 ± 1	6.6 ± 0.7	3.8 ± 0.4
Conf. B	61 ± 9	36 ± 5	19 ± 2	16 ± 2	11 ± 1	6.1 ± 0.6	3.5 ± 0.4
Conf. C	-	130 ± 30	71 ± 12	58 ± 9	41 ± 5	23 ± 3	13 ± 1
Conf. D	140 ± 30	80 ± 10	44 ± 6	36 ± 4	25 ± 3	14 ± 1	8.0 ± 0.8
Conf. E	56 ± 8	33 ± 4	18 ± 2	15 ± 2	10 ± 1	5.6 ± 0.6	3.3 ± 0.3
Conf. F	54 ± 7	31 ± 3	17 ± 2	14 ± 1	9.8 ± 1.0	5.4 ± 0.6	3.1 ± 0.3
Conf. G	56 ± 8	32 ± 4	18 ± 2	14 ± 1	10 ± 1	5.6 ± 0.6	3.2 ± 0.3
Conf. H	160 ± 50	100 ± 20	53 ± 8	43 ± 6	31 ± 4	17 ± 2	9.7 ± 0.9
Conf. I	71 ± 11	40 ± 5	23 ± 3	18 ± 2	13 ± 1	7.1 ± 0.7	4.1 ± 0.4
Conf. J	72 ± 12	41 ± 5	23 ± 3	19 ± 2	13 ± 1	7.2 ± 0.7	4.2 ± 0.4
Conf. K	63 ± 10	36 ± 4	20 ± 2	16 ± 2	11 ± 1	6.3 ± 0.6	3.6 ± 0.4
Conf. NA	55 ± 8	32 ± 4	17 ± 2	14 ± 1	10 ± 1	5.5 ± 0.6	3.2 ± 0.3
Conf. NB	70 ± 10	40 ± 5	22 ± 2	18 ± 2	13 ± 1	6.9 ± 0.7	4.0 ± 0.4
LST-array	45 ± 6	26 ± 3	14.5 ± 1.5	12 ± 1	8.3 ± 0.9	4.6 ± 0.5	2.6 ± 0.3
MST-array	-	160 ± 50	90 ± 20	75 ± 12	53 ± 8	59 ± 3	17 ± 2
Conf. 2NN	49 ± 7	30 ± 4	16 ± 2	13 ± 1	9.1 ± 0.9	5.0 ± 0.5	2.9 ± 0.3
- (0.04–0.1 TeV)	38 ± 4	22 ± 2	12 ± 1	9.8 ± 1.0	7.0 ± 0.7	3.8 ± 0.4	2.2 ± 0.2
- (0.1–1 TeV)	160 ± 50	100 ± 20	53 ± 8	43 ± 6	30 ± 4	17 ± 2	10 ± 1
- (1–10 TeV)	-	-	-	-	-	-	320 ± 250
Conf. 2Nb	47 ± 7	27 ± 3	15 ± 2	12 ± 1.2	8.6 ± 0.9	4.7 ± 0.5	2.7 ± 0.3
Conf. 2Nc	51 ± 7	29 ± 3	16 ± 2	13.0 ± 1.4	9.2 ± 1.0	5.0 ± 0.5	2.9 ± 0.3
Conf. 2Nd	38 ± 5	22 ± 2	11.9 ± 1.3	9.8 ± 1.0	6.9 ± 0.7	3.8 ± 0.4	2.2 ± 0.2
Conf. 2Ne	64 ± 10	37 ± 5	20 ± 2	17 ± 2	11.9 ± 1.2	6.5 ± 0.7	3.7 ± 0.4
Conf. 2Nf	57 ± 8	33 ± 4	18 ± 2	14.7 ± 1.7	10.4 ± 1.0	5.7 ± 0.6	3.3 ± 0.3
2b	100 ± 20	59 ± 9	32 ± 4	27 ± 3	19 ± 2	10.3 ± 1.1	5.9 ± 0.6
2c	110 ± 20	65 ± 10	36 ± 4	29 ± 3	20 ± 2	11.3 ± 1.2	6.5 ± 0.7
2e	58 ± 8	33 ± 4	18 ± 2	15.0 ± 1.6	11 ± 1	5.8 ± 0.6	3.3 ± 0.3

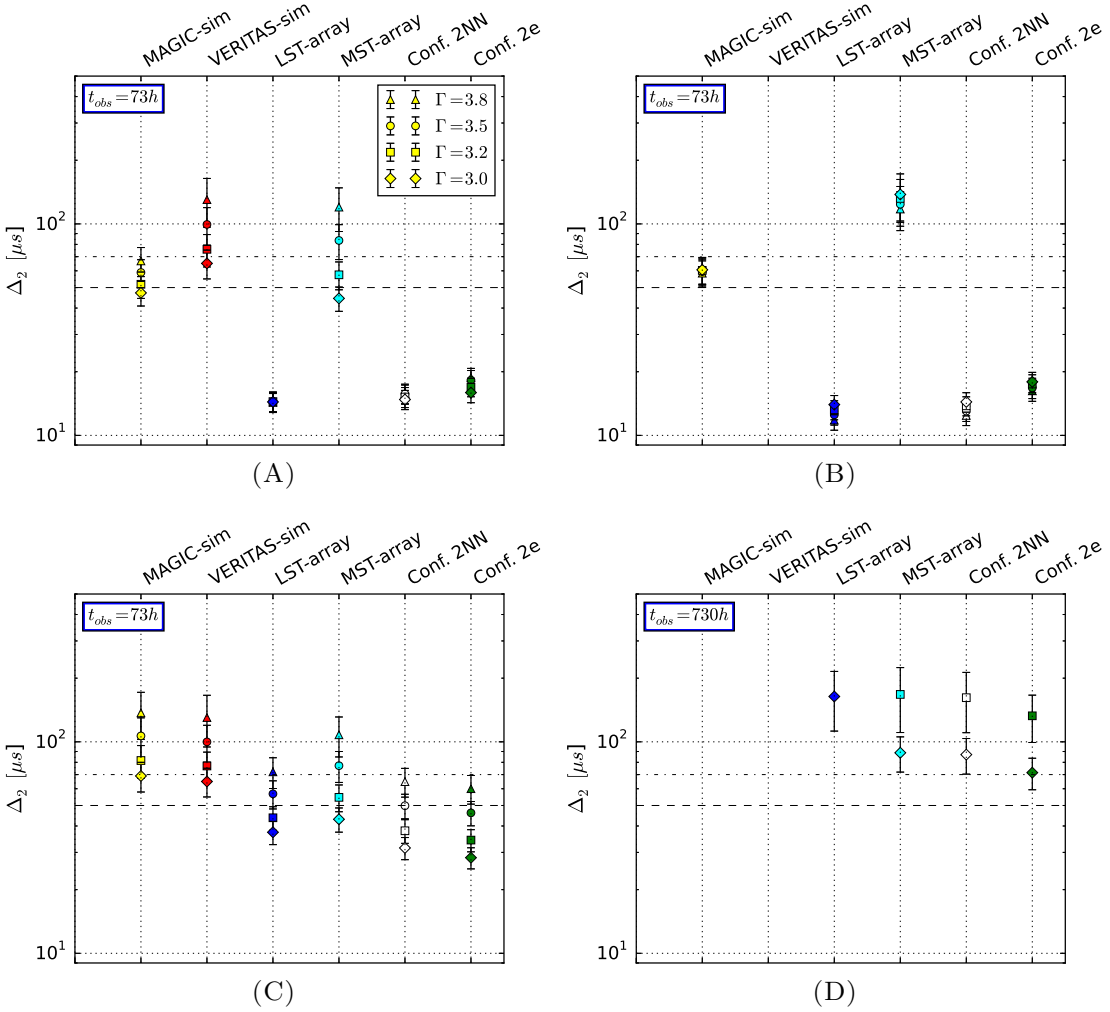

FIGURE 3.8: Uncertainty in the position of the interpulse P2 (Δ_2) of the VHE profile of the Crab pulsar for different values of the spectral index Γ: 3.8 (triangles), 3.5 (circles), 3.2 (squares), 3.0 (diamonds). Results for MAGIC (yellow), VERITAS (red), the LST-array (blue), the MST-array (cyan), Conf. 2NN (white) and Conf. 2e (green) are shown. The first 3 panels refer to simulations of 73-hour observations in the full energy range (A), in the low energy range (0.04–0.1 TeV, B) and in the mid energy range (0.1–1 TeV, C). The last panel (D) shows the results of simulations of 730-hour observations in the high energy range (1–10 TeV). Error-bars represent the standard deviation calculated from a set of simulations. The dashed and dotted-dashed lines show the uncertainties of the MAGIC (Δ_2 = 50 μs [96]) and VERITAS (Δ_2 = 70 μs [99]) observations, respectively.

TeV is equal to that obtained with MAGIC in the same energy interval [96]. The values of Δ_2 resulting from the simulations of 73-hour observations for all configurations from Table 3.3 and for simulations in the low (0.04–0.1 TeV) and mid (0.1–1 TeV) energy ranges are shown in Figs. 3.8A, 3.8B and 3.8C, respectively. The results of the 730-hour observations at energies from 1 to 10 TeV are reported in Fig. 3.8D.

TABLE 3.5: Parameters of the parabolic fit of the phase drift. The first line shows the assumed spin-down law, while the second and third lines contain the best fitting values of the parameters obtained from a fit of the simulated spin-down for two different observing intervals (2 nights and 3 nights; see text for details).

	ϕ_0	a (10^{-5} s^{-1})	b (10^{-10} s^{-2})
ψ	0.394	1.0	-1.85
ψ_{2d}	0.386±0.004	1.05 ± 0.06	-1.90±0.06
ψ_{3d}	0.390±0.002	0.995 ± 0.006	-1.847±0.003

3.4.3 VHE Timing Analysis

The quality of the pulse shape obtained with the LST-array suggests that a VHE timing analysis of the Crab pulsar, similar to that performed at lower energies (radio/optical/X-ray/low-energy gamma-ray bands), is possible with CTA. I attempted to perform such an analysis of the simulated pulse profile using an approach similar to that discussed in [187] and [188].

The time required for the LST-array to achieve statistically significant detection of the pulsar period and the pulse shape is ∼1 hour. From the period derivative of the Crab pulsar, one can estimate the phase drift during time Δt as $\Delta\phi_{\rm drift} \approx \dot{\nu}\Delta t^2/2$. Assuming $\dot{\nu} \approx -3.7 \times 10^{-10}$ s^{-2} (see e.g. [188]) and $\Delta t = 3$ hours, I find $|\Delta\phi_{\rm drift}| \approx 0.02$, value comparable to the bin size adopted here ($1/N_{\rm bins}$). Therefore, no more than three consecutive 1-hour observations can be performed without a significant phase drift of the Crab pulsar pulse profile.

I investigated the phase drift of the interpulse P2 (more prominent at VHE than the main pulse), measured with short LSTs observations during a number of consecutive nights. Such measurements require an accurate initial estimate of the Crab pulsar period. For each night, I simulate three 1-hour observations assuming a parabolic law for the phase drift:

$$\psi(t) = \phi_0 + a(t - t_0) + b(t - t_0)^2 \,, \tag{3.7}$$

where ϕ_0 is the pulsar phase at t_0, $a = (\nu_0 - \nu_{\rm init})$ is the difference between the rotational frequency of the pulsar ν_0 at t_0 and a reference frequency $\nu_{\rm init}$. b is equal to $\dot{\nu_0}/2$, where ν_0 is the rotational frequency first derivative at t_0. $\nu_{\rm init}$ is the reference frequency used to fold the data. In this analysis I assume that the difference between ν_0 and $\nu_{\rm init}$ is of the order of 10^{-5} s^{-1} and that $\dot{\nu_0} \simeq -3.7 \times 10^{-10}$ s^{-2} (see e.g. [187] or [188]). The adopted values of ϕ_0, a and b are reported in the first line of Table 3.5. In order to accurately fold real data, it will require changing reference frequency each night (see [188]). It is possible to reduce the phase measurements to a single reference frequency using the method described in Zampieri et al. [188].

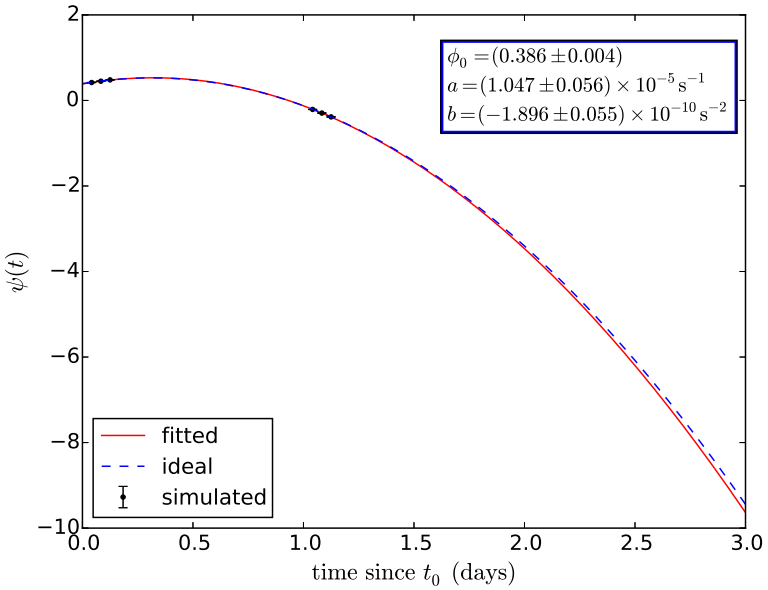

FIGURE 3.9: Simulated phase drift of the VHE interpulse of the Crab pulsar observed with the LST-array over 2 nights. The blue dashed line is the assumed spin-down law. The red solid line is the best-fit parabola. Black dots are the simulated data.

Following the procedure described in Sect. 3.2, for each observation I simulated the pulse profile detected with the LST-array[5] and obtained the phase drift ψ_i and error σ_i of the interpulse in the i-th observation. Typically, $\sigma_i \sim 120$ μs. I then simulated 2 and 3 nights of observations of the Crab pulsar (see Figs. 3.9 and 3.10). The positions of the interpulse, derived from the simulated observations and reduced to the same reference frequency, were then fitted with the parabolic law in Eq. (3.7). Best fit coefficients and corresponding errors are reported in Table 3.5 (second and third lines). From these values it is possible to estimate the accuracy in determining the time of arrival of the interpulse, which is ~ 140 μs after 2 nights and ~ 80 μs after 3 nights (assuming $P(t_0) = 0.03362$ s, which is the approximate rotational period of the Crab pulsar at t_0 [188]). Increasing the number of observing nights does not improve significantly the accuracy of the fitting parameters (e.g. the accuracy in determining the position of the interpulse is ~ 65 μs after 7 nights).

For the MSTs and SSTs this type of measurements of the phase drift of the interpulse is not feasible because detecting a pulse profile requires more than one observing night.

[5]For these simulations I assume a power-law spectrum for the Crab pulsar with $N_0 = 13.0 \times 10^{-11}$ TeV^{-1} cm^{-2} s^{-1} and $\Gamma = 3.57$.

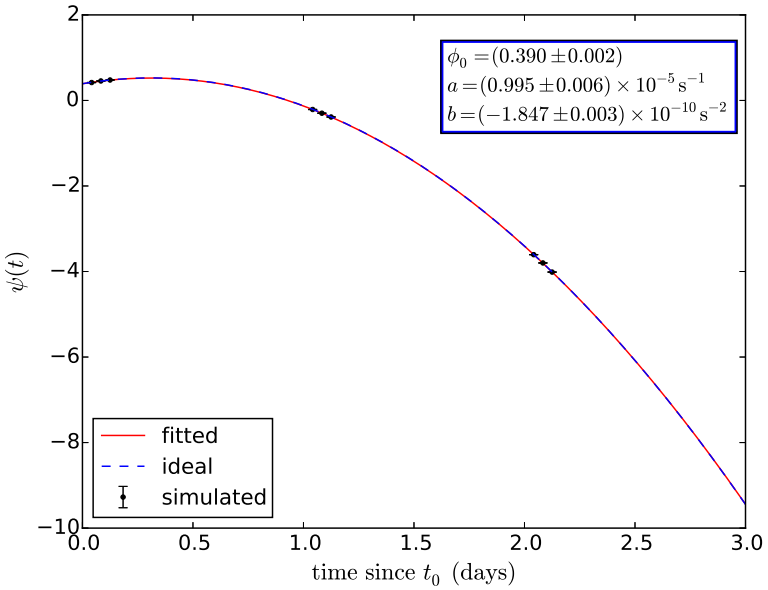

FIGURE 3.10: Same as Fig. 3.9 for observations covering 3 nights.

3.5 Discussion

I performed simulations of the VHE gamma-ray pulse profile of the Crab pulsar for different configurations of CTA and the ASTRI mini-array, therefore in intrinsically different energy ranges and with different observing times. The LSTs, MSTs and SSTs will probe different spectral regions (from a few tens of GeV up to several tens of TeV) with different sensitivities [151]. For all simulated pulse profiles I determined the uncertainty Δ_2 in the position of the interpulse.

As simulations of the pulse profiles of the Crab pulsar for the MC-Prod1 and MC-Prod2 configurations give comparable values of Δ_2, in this section I will discuss the results obtained using the more recent MC-Prod2 layouts of CTA.

As shown in Fig. 3.6, the LST-array (Conf. 2NN-LST) reaches the same accuracy as MAGIC ($\Delta_2 \sim 50$ μs) but in a much shorter observation time ($0.1 \times t_{\mathrm{obs}}^{\mathrm{M}}$). 73 hours of observations with the same configuration lead to an uncertainty in the peak position of 14 μs. Observations with the northern configuration Conf. 2NN give an improvement by a factor $\sim$3 in accuracy as compared to MAGIC (with 73 hours of observing time; see again Fig. 3.6). Similar values of Δ_2 are obtained for the full-energy-range configurations Conf. 2e. These results are slightly worse than that attainable with the LST-array because of the lower background contamination and larger effective area of the latter configuration in the energy range below a few hundred GeV, where the Crab pulsar is easier to detect due to its steep spectrum.

The quality of the measured pulse shape decreases significantly above 1 TeV again because of the steeply falling spectrum. In spite of the increase in the effective area with energy, the value of Δ_2 for the MST-array (Conf. 2NN-MST) measured above 100 GeV is nearly the same as that of MAGIC above 50 GeV. This is even more the case for the high-energy-range array of SSTs. I estimated that, only with a 10^4 times longer observing time, will an array of 72 SSTs return a value of Δ_2 (above a few TeV) comparable with that of VERITAS above 100 GeV. Similar conclusions can be drawn for the ASTRI mini-array, which contains only nine SSTs. Pure detection of the pulsed emission in this case would require $\sim 10^6$ hours and is thus not achievable.

It should be noted that all estimates depend on the values of the effective area and energy threshold. Modifications of the telescopes design and arrays configurations can affect them and, therefore, change the results presented here.

Clearly, these results are very sensitive also to the VHE spectral index Γ of the Crab pulsar. I performed similar simulations assuming different values of Γ (3.0, 3.2, 3.5, 3.8) in the full (0.04–160 TeV), low (0.04–0.1 TeV), mid (0.1–1 TeV) and high (1–10 TeV) energy ranges (see Figs. 3.8A–3.8D). Below 100 GeV the best Δ_2 is provided by the LST-array. In the energy range 0.1–1 TeV the most accurate values of Δ_2 are obtained with Conf. 2NN – the northern CTA installation, which contains both LSTs and MSTs –, and with Conf. 2e, which comprises all three types of telescopes (LSTs, MSTs, SSTs). Even if the spectrum of the Crab pulsar is rather steep ($\Gamma = 3.8$) in this energy range, CTA will be able to reach an accuracy $\Delta_2 \sim 60$ μs in 73 hours (see green triangle in Fig. 3.8C). However, above 1 TeV only with 10 times longer observations (730 hours) and assuming a hard spectrum for the Crab pulsar ($\Gamma = 3.0$), will Conf. 2e perform an accurate measurement of the position of the interpulse P2 ($\Delta_2 = 70$ μs).

Theoretical models predict different spectra of isolated pulsars at VHE. Lyutikov et al. [14] showed that ultraviolet and X-ray photons produced in the inner magnetosphere can be up-scattered up to VHE in the outer magnetosphere. Assuming that the accelerating electric field is 100 times lower than the magnetic field of the neutron star and that the curvature radius of the emitting particles is of the order of the light cylinder radius $R_{\rm L}$, they concluded that the tail of the emitted spectrum would extend up to $\sim$15 TeV. Another model predicts that IC scattering on a relativistic electron-positron pair plasma accelerated in annular or core gap regions can produce a VHE gamma-ray spectrum extending up to 400 GeV [117]. A mechanism of VHE gamma rays production through inverse Compton (IC) scattering of X-ray photons on relativistic electrons, accelerated in a region located beyond the light cylinder of a neutron star[6], is reported in [8]. According

[6]The acceleration region is assumed to be located at a distance from $20R_{\rm L}$ to $50R_{\rm L}$, where $R_{\rm L}$ is a light-cylinder radius.

to this model, the cut-off energy of the gamma-ray spectrum should be around 500 GeV. Taking into account the relative orientation of the IC scattering region with respect to the observer, this model also predicts a shift between the time of arriving of X-ray and VHE gamma-ray pulses, which amounts to $\sim 54-134$ μs for $R_{\rm w} \div 20R_{\rm L} - 50R_{\rm L}$ (gamma rays leading). This values is not consistent with present VHE observations obtained with MAGIC [96] and VERITAS [99], which show that VHE gamma rays lag behind X-ray photons (see Sect. 3.1 and Fig. 3.2). CTA observations are needed to gather the data of better quality and probe the predictions of theoretical models.

In order to determine the VHE folded profiles needed for the present analysis, an accurate knowledge of the Crab pulsar ephemerids is required. This can be obtained from simultaneous observations at lower energies (e.g. radio, optical). However, I also investigated the possibility of performing an independent phase timing analysis at VHE only with CTA, using observations spread over several nights. The strategy is similar to that adopted in [187] and [188]. I simulated 2- and 3-night observations with the LST-array (three 1-hour exposures each night). The accuracy on the time of arrival of the interpulse is ∼140 μs and ∼80 μs for observations covering 2 or 3 nights, respectively. Resulting values are worse than those derived from a fit of the pulse profile obtained folding together all observations (using known ephemerides). Thus, although an independent VHE timing analysis based on short repeated observations appears to be feasible with the LSTs, for the sake of measuring Δ_2 the obtained results are less accurate.

3.5.1 Testing Lorentz Invariance Violation with the VHE Emission from the Crab Pulsar Detected with CTA

Another possible application of Crab-pulsar timing is testing LIV (see Sect. 1.1.6). Measuring precise phases of the main pulse and interpulse of the Crab pulse profile in different energy ranges allows to estimate the shift between the time of arrival of high- and low- energy photons. Assuming that this time delay is due to the propagation effects only, I estimated the constraints that observations of the Crab pulsar with CTA can place on $E_{\rm LIV}$[7].

I compared the accuracy attained on the measurement of the position of the interpulse (P2) using the *Fermi*-LAT data above 100 MeV [10] and CTA simulations of 110-hour observations with the MST-array. The rotational period of the Crab pulsar is assumed to be 33.62 ms. The uncertainties are:

- *Fermi*-LAT (>100 MeV): $\delta_1 = 74$ μs (from [10]),

[7] $E_{\rm LIV}$ is the energy at which the LIV effects become significant.

- MST-array (>158 GeV): $\delta_2 = 75$ μs (see Table 3.4).

In order to derive an upper limit to LIV effects, I assume that no intrinsic and light travel time delay are present between the *Fermi*-LAT and CTA energy bands. Any possible delay is caused by LIV and is smaller than the measured uncertainty on the peak arrival times. In these assumptions, one can calculate an upper limit (at the 95% confidence level) to the difference between the time of arrival of the interpulse (P2) at energies >100 MeV and >158 GeV.

$$\Delta t < 1.645 \sqrt{\delta_1^2 + \delta_2^2} \approx 170 \ \mu\text{s}\,. \tag{3.8}$$

Using this limit and Eqs. (1.4) and (1.5), I obtained the following constraints on the linear (Eq. (3.9)) and quadratic (Eq. (3.10)) terms of $E_{\rm LIV}$:

$$E_{\rm LIV} = \frac{d}{c_0} \frac{E_{\rm high} - E_{\rm low}}{\Delta t} > 1.9 \times 10^{17} \ \text{GeV}\,, \tag{3.9}$$

$$E_{\rm LIV} = \sqrt{\frac{3d}{2c_0} \frac{E_{\rm high}^2 - E_{\rm low}^2}{\Delta t}} > 6.7 \times 10^{9} \ \text{GeV}\,, \tag{3.10}$$

where d is the distance to the Crab pulsar (assumed to be 2 kiloparsecs).

These results are similar to those obtained from the analysis of the VERITAS observations of the Crab pulsar [83], in which the uncertainty was averaged over both peaks (main pulse P1 and interpulse P2). This shows that, most probably, observations with LSTs and MSTs of CTA will not improve dramatically the LIV constraints. The SSTs will not be sensitive enough for this type of timing analysis during a 110-hour observation, because of decline of the pulsar spectrum at SST energies. On the other hand, CTA can possibly detect other more distant pulsars and/or fast rotating MSPs with harder spectra (e.g. PSR J0614−3329). Such observations, especially at TeV energies, will provide valuable data for more stringent LIV tests.

3.6 Conclusions

The energy spectrum and pulse profile at VHE are crucial ingredients for any comprehensive theory of pulsar emission. Different mechanisms for particle acceleration and VHE gamma-ray emission have been proposed (see [8, 14, 202]). Some models (e.g. [116]) can predict the shape of the pulse profile and yield different time shifts between the position of the peaks at VHE and in the radio band. Because of its better sensitivity and wider energy range CTA will provide crucial input for the theory. Together with the full CTA, the LSTs- and MSTs-arrays will provide an accurate measurement of the time

of arrival of the peaks at VHE, and will then allow us to determine its shift with respect to simultaneous measurements in other energy bands (radio, optical, X-rays, low-energy gamma rays [10]). In this respect, it would be important that presently on-going monitoring programs of the Crab pulsar at different wavelengths (e.g. that of Jodrell Bank in the radio) continue to operate.

Configurations containing LSTs/MSTs (with threshold energy $E_{\rm thr}$ equal to 0.04/0.16 TeV) will be able to measure more detailed features in the VHE pulse profile, which will further constrain the emission region and emission mechanism of pulsars. Any potential phase shift between the LST- and MST-arrays significantly larger than $\sim$270 μs will also be detectable. On the other hand, extrapolating the power-law spectral shape inferred at lower-energies, an accurate determination of the pulse profile of the Crab pulsar with the high-energy SSTs ($E_{\rm thr}$ = 1 TeV) is not possible for observing times of less than $\sim 7 \times 10^5$ hours.

Chapter 4

Imaging the Vela X Region with the Cherenkov Telescope Array and the ASTRI Mini-array

The Vela X is a bright source in the VHE gamma-ray sky. It is associated with a PWN and a rotation-powered neutron star, PSR J0835−4510 (Vela pulsar). A large number of studies of this region has been carried out so far at different wavelengths. However, a comprehensive picture explaining the nature of the extended emission from this source is still missing. Recent observations of the Vela X region carried out with IACTs (e.g. H.E.S.S.) provided a detailed spectral and morphological description of its VHE gamma-ray emission.

In this chapter I present a detailed analysis of the VHE gamma-ray Vela X diffuse emission and simulate observations of the Vela X region with CTA. The final goal is to accurately estimate the significance of the Vela pulsar detection with CTA, using the latest VHE results from H.E.S.S. observations [25].

I also discuss the resolving capabilities of CTA and the ASTRI mini-array, which can improve our knowledge of the Vela X morphology in the TeV energy band and help us to solve the problem of the origin of the VHE gamma rays inside the Vela PWN. Simulations are performed using two different softwares: *ctools* and *Astrisim*. The results obtained with the two software packages are cross-checked for consistency.

4.1 Broadband Emission of Vela X

Vela X is a relatively old PWN (age $\gtrsim 10^4$ years) in the Vela constellation, powered by PSR J0835−4510 (Vela pulsar) [203].

The Vela pulsar was first discovered in the radio band [204]. Johnson et al. [205] constrained the size of its emission region, using data obtained with the Green Bank Telescope. The optical polarimetry [206] and spectral properties [207] of this pulsar have been studied in detail, along with its pulsed emission in X-rays and gamma rays (e.g. [208] and [161], respectively). The first IACT detection of the Vela pulsar at energies <100 GeV was obtained out with H.E.S.S.[1]

The diffuse emission of Vela X has also been studied at all wavelengths. It was discovered in the radio band [209]. ROSAT X-ray observations [210] showed its central filamentary structure, called cocoon and associated with the jet from the pulsar. A number of filaments and arcs (including the central cocoon) have been observed along the whole PWN in radio (e.g. [211, 212]). The first 16-hour VHE gamma-ray observations of the Vela X region with the H.E.S.S. telescope at energies up to 65 TeV found diffuse emission consistent with the X-ray cocoon [213]. de Jager et al. [214] proposed a theoretical model for Vela X which requires two populations of leptons emitting in two different regions: (i) the central cocoon observed in both the X-ray and VHE bands, and (ii) the extended area corresponded to the radio emission. Alternative models assume the contribution of hadrons to the VHE gamma-ray emission, produced through neutral pion decay (see e.g. [215]). Later *Fermi*-LAT observations [168] showed that the emission from Vela X at energies >800 MeV is coincident with the radio morphology rather than with that in X-rays or VHE gamma rays. Analyzing the spectrum of the diffuse gamma-ray emission, Abdo et al. [168] concluded that the two-population leptonic scenario is consistent with the *Fermi*-LAT data more than hadronic models. In this interpretation the first population of electrons is responsible only for the extended IC emission at GeV energies and for the radio synchrotron emission. The second population of more energetic leptons produces the VHE gamma-ray and X-ray cocoon photons via IC scattering and synchrotron emission, respectively. However, it should be noted that the gamma-ray emission from Vela X detected with AGILE in the 100 MeV – 3 GeV energy range [216], is not positionally coincident with the corresponding *Fermi*-LAT emission region. In addition, AGILE data yield on harder spectrum than to that obtained from the *Fermi* analysis.

Recently, the Vela X PWN was re-observed in the VHE gamma-ray band (up to 70 TeV) with the H.E.S.S. instrument [25]. The longer observing time (53.1 hours) allowed

[1] http://www.mpg.de/8287998/velar-pulsar

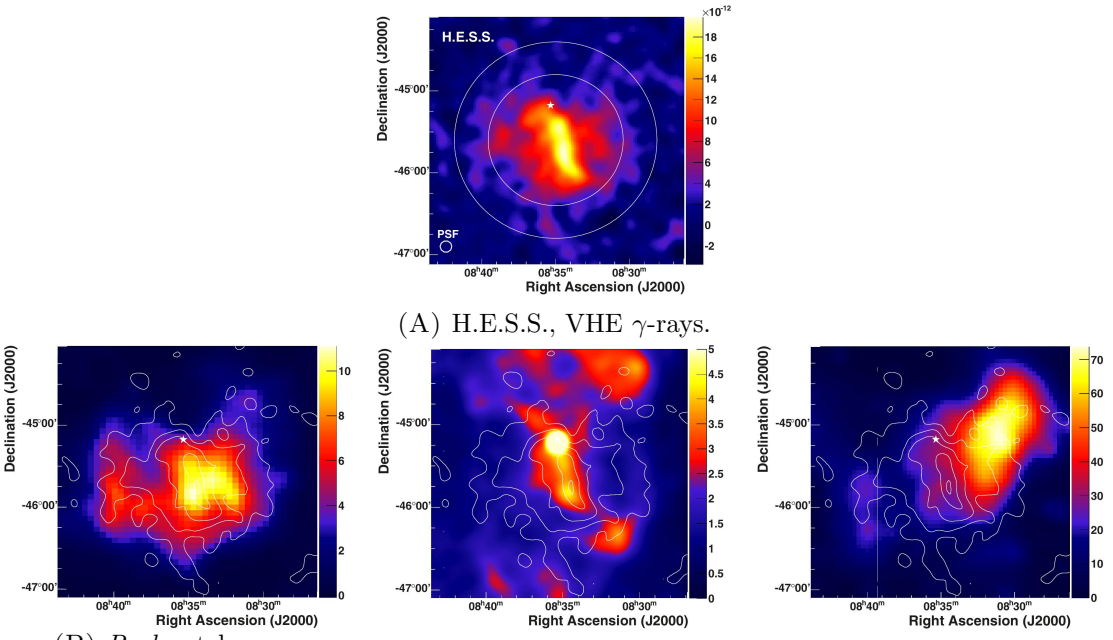

(A) H.E.S.S., VHE γ-rays.

(B) *Parkes* telescope, radio band.

(C) ROSAT, X-rays.

(D) *Fermi*-LAT, γ-rays.

FIGURE 4.1: Vela X region at different wavelengths. (A) H.E.S.S. surface brightness map (cm^{-2} s^{-1} deg^{-2}) at (0.75–70) TeV, smoothed at 0.07°. (B) Sky-map (Jy/Beam) obtained with the *Parkes* radio telescopes at 2.4 GHz with 0.17° of half-power beam width (HPBW). (C) ROSAT X-ray sky-map (kcounts deg^{-2}) at energies >1.3 keV, smoothed at 0.07°. (D) *Fermi*-LAT gamma-ray Test Statistic (TS) map at energies >800 MeV with angular resolution of 0.6° (68% of PSF at 1 GeV). The white star marks the position of the Vela pulsar. White circles in Fig. 4.1A correspond to 0.8° and 1.2° radii, whereas white contours in Figs. 4.1B, 4.1C and 4.1D indicate VHE surface brightness levels of 0.3, 0.6, 1, 1.6 and 1.9 × 10^{-11} cm^{-2} s^{-1} deg^{-2}. (Images taken from [25]).

to perform more detailed morphological[2] and spectral analyses of different parts of the diffuse emission. In contrast to previous studies [213], significant extended emission out of the cocoon region ("wings") was found (see Fig. 4.1A). This challenged the theoretical two-population scenario from de Jager et al. [214], which was used for the interpretation of the *Fermi*-LAT data [168] (as discussed above). Abramowski et al. [25] compared the VHE morphology with that at other wavelengths (Fig. 4.1). They used archival data obtained with the *Parkes* telescope during the radio Galactic Plane survey at 2.4 GHz [217] (Fig. 4.1B), with the ROSAT X-ray telescope in the ROSAT All Sky Survey (RASS) at energies >1.3 keV [218] (Fig. 4.1C) and with the *Fermi*-LAT at energies >800 MeV [168] (Fig. 4.1D).

The VHE morphology of the Vela X diffuse emission is intermediate between that at radio wavelengths and that in the X-rays: the central inner part of the TeV emission region coincides with the X-ray cocoon, whereas the VHE extended "wings" (along the right ascension, x-axis) are consistent with the radio morphology (Fig. 4.1). One of the

[2]The angular resolution of H.E.S.S. is ∼0.07°.

possible explanations for the VHE emission is that it originates through IC scattering on an energetic population of electrons with morphology intermediate between those in the X-ray and radio bands. Another possible interpretation is that the two populations of leptons produced the radio and X-ray emission emit also at VHE. In this hypothesis Abramowski et al. [25] showed that the VHE gamma-ray morphology of the Vela X region can be accounted for by a "radio-like" component emitting 65% of the flux and by an "X-ray-like" component emitting the remaining 35% of the flux.

4.2 Modeling the VHE Emission from the Vela X Region

In Chapter 2, the significance of the Vela pulsar was calculated using the *Fermi*-LAT model of the Vela X PWN (from 2FGL). Since the *Fermi*-LAT and H.E.S.S. observations of this PWN indicate different morphologies at GeV and TeV energies, I perform accurate simulations of the Vela X region at VHE, in order to provide more realistic estimates of the Vela pulsar detection significance during CTA observations.

In addition, I discuss perspectives for the CTA and ASTRI mini-array observations of the Vela X extended source. Since CTA is planed to have better sensitivity and angular resolution compared to the current generation of IACTs (see e.g. [151]), such observations will help to solve the problem of the origin of the VHE gamma-ray emission from the Vela PWN. Preliminary investigations of this object will already be possible with the ASTRI mini-array – the possible precursor of the CTA-South installation [155].

In order to simulate the VHE emission from the Vela X region it is necessary to define the spatial and spectral models of all sources in this area of the sky: i.e. the Vela pulsar, the Vela X diffuse emission and both the isotropic and Galactic backgrounds.

Following Abramowski et al. [25], I assumed that the VHE morphology of the Vela X diffuse emission can be approximated by the superposition of the radio (65% of the flux) and X-ray (35% of the flux) spatial maps. I created radio and X-ray templates adopting archival observations. For the VHE spectrum I used the PLEC models from the analysis of the H.E.S.S. data in the 0.75-70 TeV energy range [25].

4.2.1 X-ray Template of the Vela X Diffuse Emission

For the X-ray template, I use archival observations obtained with the ROSAT satellite during the RASS. This survey covered almost all sky on the 0.1–2.4 keV energy range with an angular resolution of $\sim$1 arcmin (0.0167°, half-power radius[3]). More than 10^5

[3]The half-power radius corresponds to an encircled energy of about 50%.

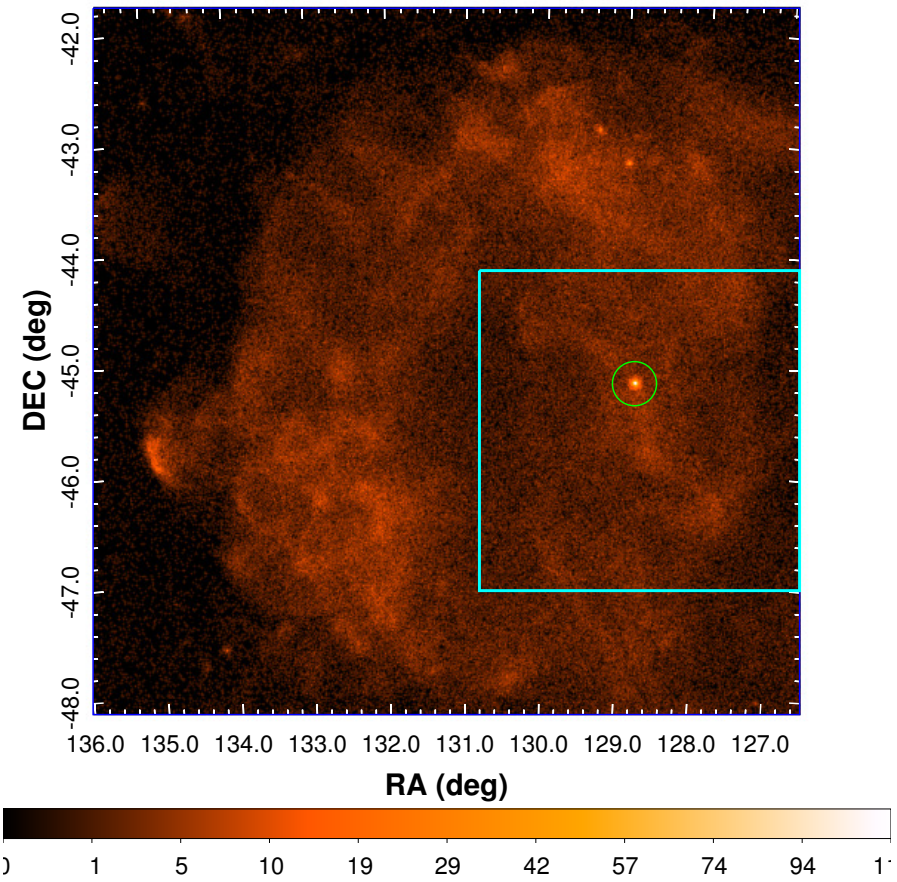

FIGURE 4.2: X-ray ROSAT All Sky Survey image of the Vela region observed in the 0.4–2.4 keV energy range. x-, y- axes are the right ascension (RA) and declination (DEC) in degrees, respectively. The color bar represents the number of counts per pixel in square root scale. The cyan frame shows to the area selected for the template and the green circle marks the position of the Vela pulsar.

X-ray sources were detected with ROSAT and included in the Faint and Bright Source Catalogs [219]. For the VHE studies I adopt the ROSAT high-resolution X-ray sky-map, using a methodology developed for the *Fermi* Science Tools[4].

I use a ROSAT count map of Vela X. This was extracted from a Position Sensitive Proportional Counters (PSPC) pointing of this region taken in the 0.4–2.4 keV energy range and lasting ∼25.6 ks[5]. The adopted count map is shown in Fig. 4.2. In this map I selected a 2.9° × 2.9° ROI, centered on the coordinates $\alpha_0 = 128.75°$ and $\delta_0 = -45.6°$ (J2000).

Several steps are required to convert the adopted template to a format appropriate for the VHE simulations. First of all, I exclude the diffuse X-ray background, unrelated to

[4] http://fermi.gsfc.nasa.gov/ssc/data/analysis/scitools/extended/extended.html

[5] File "rs932518n00_im2.fits" downloaded from http://www.xray.mpe.mpg.de/cgi-bin/rosat/rosat-survey.

the Vela X extended source. To this purpose, I define three $0.3° \times 0.3°$ regions around the central structure (BG1, BG2 and BG3 in Fig. 4.3A) and determine the background level taking the average value of counts per pixel among them. The position of the centers of these regions are the following:

- $(\alpha, \delta)_{\rm BG1} = (130.5°, -46°)$;
- $(\alpha, \delta)_{\rm BG2} = (12°7, -45°)$;
- $(\alpha, \delta)_{\rm BG3} = (127°, -46.7°)$.

Since only non-zero pixels can be used for the simulation, I set to zero the contribution of those pixels, which are 3 times fainter than the average background level of regions BG1, BG2 and BG3 (Fig. 4.3B). This threshold is chosen in order to avoid the contamination from the X-ray background in the gamma-ray simulations.

In addition, I removed also the point-like contribution of PSR J0835−4510 ($\alpha_* = 128.83°$, $\delta_* = -45.18°$). I considered a circle PS1 around the Vela pulsar and set the number of counts in this region equal to the average intensity of the neighboring annulus R1 (see Fig. 4.3B). The radius of PS1 ($R_{\rm PS1}$) is 0.063°, ∼4 times larger than the ROSAT angular resolution (0.0167°). The ring R1 is centered on the Vela pulsar position and its inner and outer radii are equal to $3R_{\rm PS1}$ and $5R_{\rm PS1}$, respectively. The R1-region is rather close to the central point source but at the same time it is not affected by the emission from the Vela pulsar. Therefore, almost no X-ray photons ($\lesssim$5%) from PSR J0835−4510 will be included in the VHE simulations. The resulting template is shown in Fig. 4.3C.

Abramowski et al. [25] determined the spectral parameters of the Vela X emission at VHE in two regions both centered at (α_0, δ_0), in a circle with radius of 0.8° and in a ring with inner and outer radii of 0.8° and 1.2°, respectively. Selecting the same regions in the X-ray template, I adopted the spectra reported in [25] for each of them. Then I normalized the total flux of each of these templates to 1:

$$N_0 = \sum_i N_i \Delta^2_{\rm pix} \, (\pi/180°)^2 \, , \tag{4.1}$$

where N_i is the number of counts in i-th pixel and $\Delta^2_{\rm pix}$ is the size of a single pixel in deg^2.

The final circular and ring- X-ray templates of the Vela X diffuse emission used in the analysis are reported in Figs. 4.3D and 4.3E.

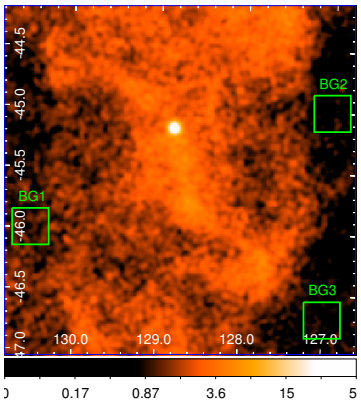

(A) ROSAT PSPC image of Vela X.

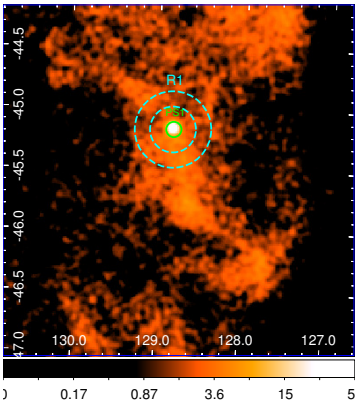

(B) Background subtracted X-ray image.

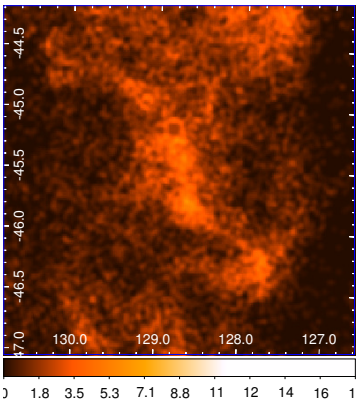

(C) X-ray image after background and point source subtraction.

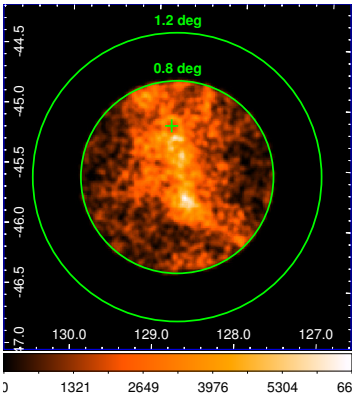

(D) Final normalized X-ray template (circle region).

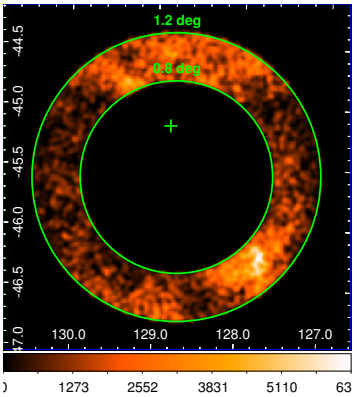

(E) Final normalized X-ray template (ring).

FIGURE 4.3: X-ray templates of the Vela X diffuse emission. (A) ROSAT PSPC image with the three regions selected for the background subtraction. (B) Background subtracted X-ray image with region PS1 (green circle) having $R_{\rm PS1} = 0.063°$ and the annulus R1 (cyan ring) having inner and outer radii $3R_{\rm PS1}$ and $5R_{\rm PS1}$ used for subtraction of the point source emission. (C) X-ray image of Vela X cleaned from the contribution of the background and pulsar (point source) emission. (D),(E) Final (normalized) X-ray templates of the Vela X diffuse emission. x-, y- axes represent the right ascension and declination in degrees, respectively. In Figs. 4.3A and 4.3B color bars are the number of counts per pixel in logarithmic scale, while those of Figs. 4.3C and 4.3D/4.3E are in linear scale. Circles in Figs. 4.3D and 4.3E have radii of 0.8° and 1.2°, respectively. The cross marks the Vela pulsar position.

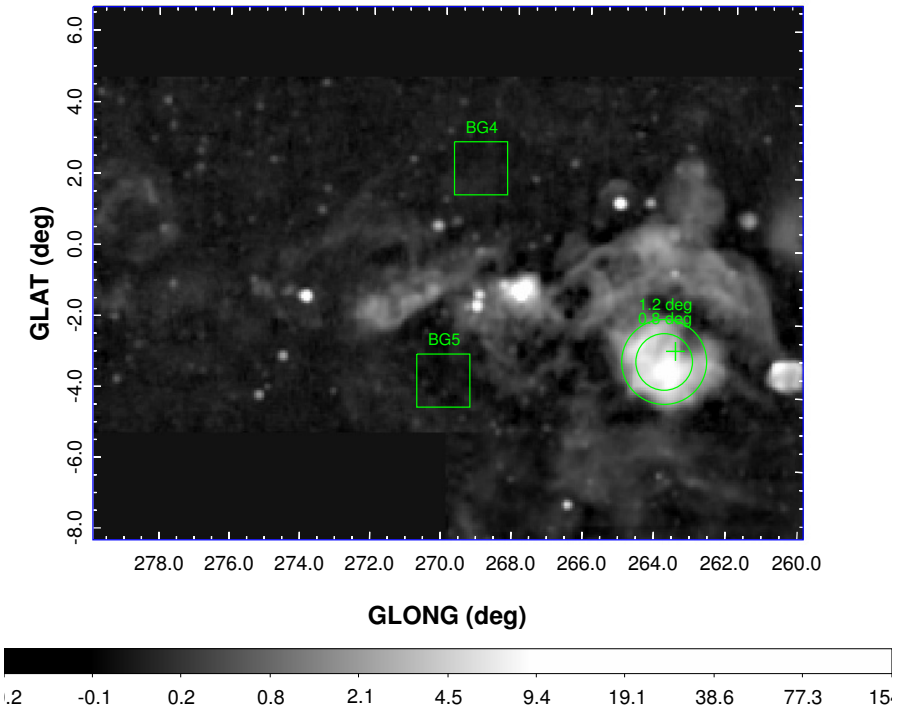

FIGURE 4.4: Radio power-map ("block 5") containing the Vela X region, obtained from the *Parkes* 2.4 GHz Survey of the southern Galactic Plane. x-, y- axes are the Galactic longitude (GLONG) and latitude (GLAT) in degrees, respectively. The color bar represents the intensity (Jy/Beam) in logarithmic scale. BG4 and BG5 are the background extraction regions. The two circles have radii of 0.8° and 1.2°, respectively. The cross marks the Vela pulsar position.

4.2.2 Radio Templates of the Vela X Diffuse Emission

The radio templates are obtained from the *Parkes* 2.4 GHz Survey of the southern Galactic Plane [217]. The angular resolution of these observations is the half-power beam width (HPBW) equaled to about 0.17°. I use the radio power-map "block 5" of the *Parkes* Survey[6], which covers the galactic longitudes $260° < l < 280°$ and includes the Vela region (see Fig. 4.4). The observation epoch of the map was converted from B1950.0 to J2000.0. I define the average background intensity (Jy/Beam) in regions BG4 and BG5 shown in Fig. 4.4 (following the procedure described in Sect. 4.2.1). The size of each region is 1.5° and their coordinates are $(l, b)_{\rm BG4} = (269°, 2.2°)$ and $(l, b)_{\rm BG5} = (270°, -3.75°)$. All pixels, which are 3 times fainter than the average background level, are set to zero. I then extract circular and ring- radio templates from the initial *Parkes* radio map and normalized them according to Eq. (4.1). Resulting templates are reported in Figs. 4.5A and 4.5B.

[6]File "`tp_small_5_v2.fits`" downloaded from `http://www.atnf.csiro.au/research/surveys/2.4Gh_Southern/block5.html`

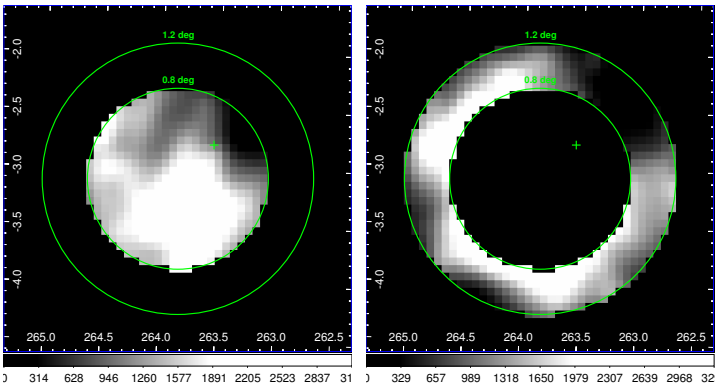

(A) Final normalized *Parkes* radio circular template.

(B) Final normalized *Parkes* radio ring-template.

FIGURE 4.5: *Parkes* radio templates of the Vela X diffuse emission: (A) circular template, (B) ring-template. x-, y- axes are the Galactic longitude (GLONG) and latitude (GLAT) in degrees, respectively. The color bar represents the normalized intensity. Circles have radii of 0.8° and 1.2°, respectively. The cross marks the Vela pulsar position.

The angular resolution of the *Parkes* telescope (0.17° at HPBW) is slightly broader than that of H.E.S.S. (0.07° at 1 TeV). Therefore, the VHE simulations carried out with the *Parkes* radio templates can be used for comparison with [25], where the *Parkes* radio data were adopted for morphological studies. However, to simulate more detailed VHE count maps, I used data with better spatial resolution for the Vela X templates.

To obtain high-resolution radio templates, I used the data from the second Molongo Galactic Plane Survey (MGPS-2) at 843 MHz, taken with the MOST radio telescope [220]. This survey consists of 629 images with an angular size of 4.3° and covers the following area on the sky: $245° < l < 365°$ and $|b| < 10°$, with angular resolution of about 0.0167°. Two fields of view contain the Vela X region[7] (see Figs. 4.6). In order to build the MOST radio templates, I stacked the fields of view vertically, defined an average background intensity level (Jy/Beam) in regions BG6 and BG7 (see Fig. 4.6) and set again to zero all pixels which are 3 times fainter than this level. The size BG6 and BG7 regions is 0.3° and their coordinates are $(\alpha, \delta)_{\rm BG6} = (129.8°, -43.9°)$ and $(\alpha, \delta)_{\rm BG7} = (130°, -47.6°)$. Then, I removed the contribution of all bright point sources (including the Vela pulsar), defining for each of them a circular region PS2 with a radius $R_{\rm PS2} = 0.04°$ (≈2.4 times the MOST HPBW[8]) and a ring R2 with inner/outer radius equal to $3R_{\rm PS2}/5R_{\rm PS2}$. All pixels within the PS2-regions are set equal to the average value of the surrounding ring R2. In Fig. 4.6A the PS2- and R2- regions around two bright point sources are shown as an example. Coordinates of all masked point

[7] Files "`J0840M44.FITS`" (upper part of the Vela X) and "`J0840M48.FITS`" (lower part of the Vela X), downloaded from `http://www.physics.usyd.edu.au/sifa/Main/MGPS2`.

[8] Almost all photons (≳80%) from the radio point source are assumed to come from within a radius of 0.04°.

TABLE 4.1: Coordinates of the bright point sources masked in the top and bottom fields of view of the MGPS-2. Right ascensions (RA) and declinations (DEC) are in decimal degrees.

RA (deg)	DEC (deg)	FoV	RA (deg)	DEC (deg)	FoV
127.31	-46.02	top	128.26	-46.26	bottom
127.85	-45.08	top	128.43	-45.26	bottom
128.23	-46.58	top	128.60	-45.33	bottom
128.29	-46.69	top	128.66	-46.12	bottom
128.34	-44.84	top	128.67	-46.06	bottom
128.41	-44.74	top	128.72	-46.12	bottom
128.42	-46.41	top	128.73	-46.04	bottom
128.42	-46.45	top	128.95	-46.11	bottom
128.50	-46.64	top	128.96	-46.19	bottom
128.57	-46.62	top	129.08	-45.48	bottom
128.60	-46.40	top	129.34	-45.78	bottom
128.84	-45.17	top	129.36	-45.25	bottom
128.88	-44.44	top	129.40	-44.88	bottom
129.37	-46.38	top	129.47	-44.75	bottom
129.70	-45.15	top	129.49	-45.46	bottom
130.12	-45.69	top	129.66	-45.80	bottom
127.23	-45.78	bottom	129.67	-44.91	bottom
127.58	-45.09	bottom	129.75	-44.53	bottom
127.92	-46.37	bottom	129.86	-46.40	bottom

sources are listed in Table 4.1. The high-resolution MOST radio templates for the Vela X extended source with normalized intensities are shown in Fig. 4.7.

As mentioned above, the VHE spectra of the inner and outer parts of the diffuse emission from Vela X are modeled using a PLEC component with spectral parameters taken from [25] and extrapolated to the CTA energy range (0.04–160 TeV, see Table 4.2).

4.2.3 Spectral and Spatial Models of Other Components

The Vela pulsar is modeled as a point source with a power-law model with spectral parameters obtained fitting the high-energy *Fermi*-LAT data (>10 GeV) extrapolated up to ∼160 TeV (see Table 2.2 in Chapter 2). I also include the GDB emission assuming a uniform spatial model and a power-law spectrum with parameters from Chapter 2 (see Table 2.3). The spatial distribution of the isotropic VHE gamma-ray background is taken to be a Gaussian function radial profile of the pointing offset angle with a dispersion of 3 deg^2, whereas the corresponding VHE spectrum is modeled through Monte Carlo simulations of the CTA layout, as explained in the next section. The parameters of all components of the Vela X region are listed in Table 4.2.

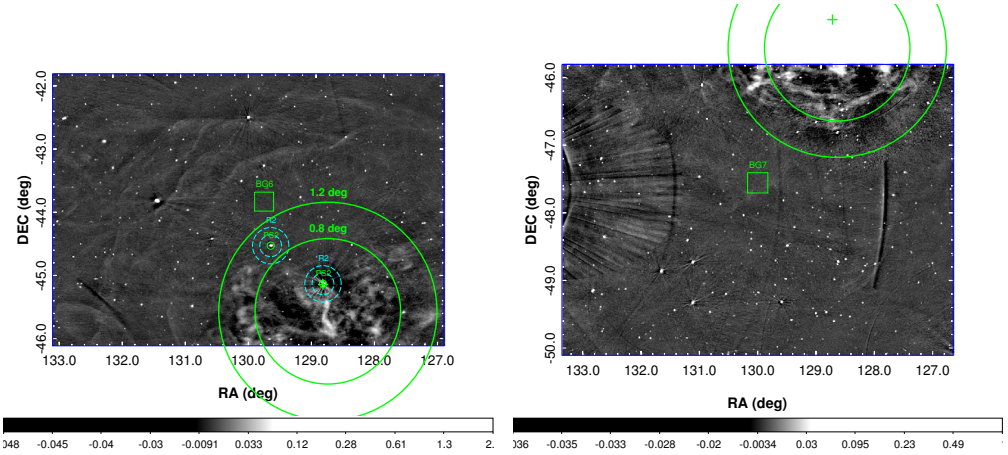

(A) Field of view with a northern part of the Vela PWN (`J0840M44.FITS`).

(B) Field of view with a southern part of the Vela PWN (`J0840M48.FITS`).

FIGURE 4.6: Radio power-maps of the Vela X region obtained from the second MOST Molongo Galactic Plane Survey (MGPS-2) at 843 MHz. Two fields of view, which contain the northern and southern parts of the Vela PWN, are shown in panels (A) and (B), respectively. x-, y- axes are the right ascension (RA) and declination (DEC) in degrees. The color bar represents the intensity (Jy/Beam). BG6 and BG7 are the background extraction regions. Circles have radii of 0.8° and 1.2°, respectively. The cross marks the Vela pulsar position. In Fig. 4.6A I also show the regions (inner circle PS2 and outer ring R2) used to mask the emission from two point sources (one is the Vela pulsar). See text for details.

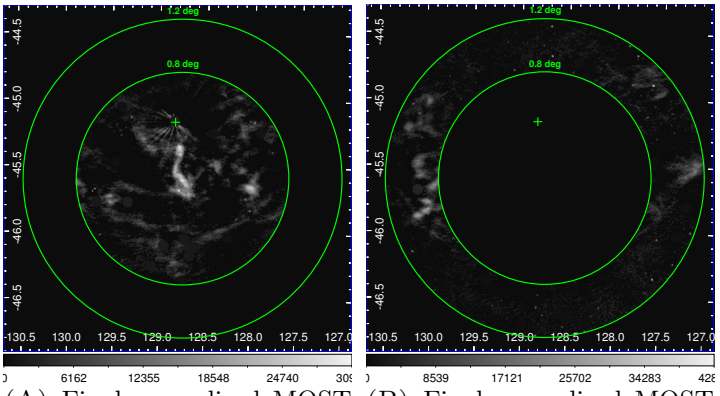

(A) Final normalized MOST radio circular template.

(B) Final normalized MOST radio ring-template.

FIGURE 4.7: MOST high-resolution radio templates of the Vela X diffuse emission after subtraction of the background and the emission of field sources. (A) Circular template, (B) ring-template. x-, y- axes are the right ascension (RA) and declination (DEC) in degrees, respectively. The color bar represents the normalized intensity. Circles have radii of 0.8° and 1.2°, respectively. The cross marks the Vela pulsar position.

TABLE 4.2: Parameters of the components contributing to the VHE gamma-ray spectrum from the Vela X region.

Component	Spatial model	Type of the spectrum	Spectral parameters
J0835−4510	point source: $\alpha_* = 128.83°$, $\delta_* = -45.18°$	power law	$N_{\rm PS} = 18.4 \pm 0.8$ $\gamma = 4.38 \pm 0.08$ $E_0 = 20$ GeV
Vela X circular region (<0.8°)	diffuse source: spatial map	PLEC	$N_{\rm X1} = 11.6 \pm 0.6$ $\gamma = 1.36 \pm 0.06$ $E_c = 13.9 \pm 1.6$ TeV $E_0 = 1$ TeV
Vela X ring (0.8° − 1.2°)	diffuse source: spatial map	PLEC	$N_{\rm X2} = 3.3 \pm 0.6$ $\gamma = 1.14 \pm 0.2$ $E_c = 9.5 \pm 2.7$ TeV $E_0 = 1$ TeV
Galactic background (GDB)	diffuse source: constant value	power law	$N_{\rm GDB} = 0.1 \pm 0.02$ $\gamma = 3.0 \pm 0.4$ $E_0 = 20$ GeV
Isotropic background	Gaussian radial profile	spectrum is defined in MC-Prod2 simulations	

$N_{\rm PS}$ in units of 10^{-14} cm^{-2} s^{-1} MeV^{-1}; $N_{\rm X1}$, $N_{\rm X2}$ in units of 10^{-12} cm^{-2} s^{-1} TeV^{-1}; $N_{\rm GDB}$ in units of 10^{-14} cm^{-2} s^{-1} MeV^{-1} sr^{-1}. γ is the spectral index. E_c and E_0 are the cut-off and scale energies, respectively (see Eqs. (2.1) and (2.2)). Errors include only statistical uncertainties.

4.3 Simulation of the VHE Observations with CTA

The VHE simulations of the Vela X region are performed with *ctools* software package [178] for the southern CTA installation[9] (CTA-South) and for Conf. s9-4-257m[10]. I use the tool `ctobssim` to perform the simulations and obtain the event lists of the observations, whereas the tool `ctbin` – to convert them into count maps. The CTA-South configuration contains 4 LSTs, 24 MSTs and 72 SSTs. Conf. s9-4-257m is an array of 9 SSTs, which represents the ASTRI mini-array. The IRF and the spectrum of the isotropic background from charged cosmic-ray particles are calculated for both configurations using MC-Prod2 simulations of a 50-hour observation of a point source with a flux of 1 Crab Unit, located at 20° zenith angle and at the center of the field of view. It is assumed that the CTA performance is not changing significantly at off-axis angles <2°.

[9] Public available files "CTA-Performance-South-20150511" on https://portal.cta-observatory.org/Pages/CTA-Performance.aspx.

[10] Conf. s9-4-257m is provided within the framework of the Sep 2014 Monte Carlo Prod2 DESY package, site "Leoncito++", available at http://www.cta-observatory.org/ctawpcwiki/index.php/WP_MC#Interface_to_WP_PHYS.

The simulated field of view covers an area of $4^\circ \times 4^\circ$, centered at (α_0, δ_0). The observing time is 53.1 hours, equal to that of the real H.E.S.S. observations reported in [25]. The input spectral model containing the various components discussed in Sect. 4.2. The diffuse Vela X emission is included as a superposition of the X-ray and radio (*Parkes*/MOST) templates. I examine three different ratios between "radio-like" and "X-ray-like" morphologies of the VHE gamma-ray surface brightness: 65%-radio plus 35%-X-ray (as discussed above), 100%-radio and 100%-X-ray.

The emission from the Vela X region observed with CTA-South is investigated in different energy ranges: 0.04–160 TeV, >0.25 TeV and >1 TeV. For comparison, I perform additional simulations with CTA-South in the spectral range 0.75–70 TeV, which corresponds to the H.E.S.S. observations [25]. The simulations for Conf. s9-4-257m (ASTRI mini-array) correspond to a slightly higher energy range: 1.6–160 TeV.

I fit the simulated data and estimate the significance of the Vela pulsar detection with the `ctlike` tool in unbinned mode. The event list obtained from `ctobssim` and the spectral model used in simulations (see Table 4.2) are the inputs for this tool. `ctlike` calculates the TS of each source in the model, performing a maximum likelihood analysis of the simulated CTA data.

4.3.1 *Astrisim* Simulations

I perform similar simulations of the Vela X region using the alternative software *Astrisim*[11], developed by the ASTRI Collaboration for simulations of VHE observations with the ASTRI mini-array. The latter can cover relatively large area on the sky because of the $\sim 10^\circ$ field of view of each dual-mirror ASTRI SST-2M telescope (see e.g. [155]). Initially, *Astrisim* was used to simulate only point-like VHE gamma-ray sources.

I adopted this software for simulations of extended sources and reproduced a 53.1-hour Vela X observations with the ASTRI mini-array (Conf. s9-4-257m) in the 1.6–160 TeV energy range, with a ROI of $15^\circ \times 15^\circ$. As an input, *Astrisim* requires a `MapCube`[12] for each source, except for the isotropic background which is simulated automatically. The Vela pulsar and GDB models are as reported in Table 4.2, while that of the Vela X diffuse emission is determined from the superposition of the MOST radio (by 65%) and X-ray (by 35%) templates.

I carried out similar simulations of the Vela X region also with *ctools* and then compared results of these two softwares. The *ctools* input model is similar to that used in *Astrisim*, except for the isotropic background, whose spatial distribution was modified to be in

[11] http://www.iasf-milano.inaf.it/~giuliani/astrisim/

[12] `MapCube` defines the spatial and spectral properties of the source in a format of the `fits`-file.

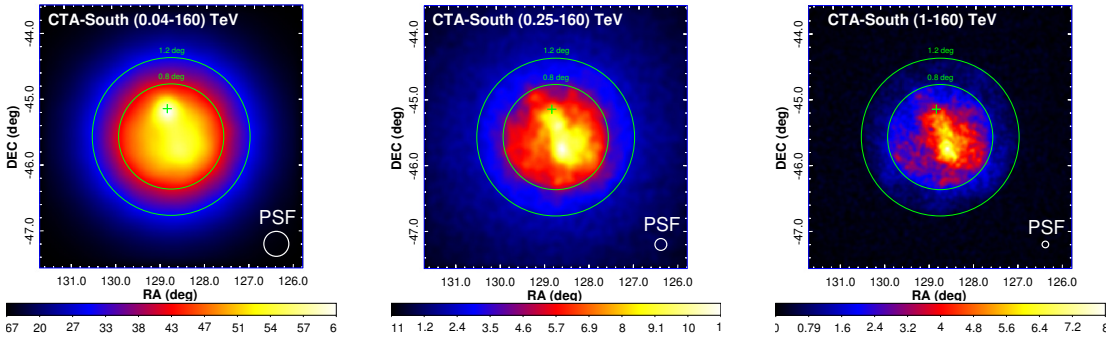

(A) $E > 0.04$ TeV (B) $E > 0.25$ TeV (C) $E > 1$ TeV

FIGURE 4.8: VHE Vela X count maps simulated with *ctools* assuming 65%-contribution from the radio *Parkes* template and 35%-contribution from the X-ray template. The CTA-South IRF is used. The exposure time is 53.1 hours. Energy ranges are (A) 0.04–160 TeV; (B) 0.25–160 TeV; (C) 1–160 TeV. x-, y- axes are the right ascension (RA) and declination (DEC) in degrees. The $4° \times 4°$ field of view is centered at $\alpha_0 = 128.75°$ and $\delta_0 = -45.6°$. The color bars in Figs. 4.8A and 4.8B/4.8C represent the number of counts in squared and linear scales, respectively. All count maps are smoothed according to the size of the corresponding PSF (white circles). See text for details. Green circles have radii of 0.8° and 1.2°, respectively. The green cross marks to the the Vela pulsar position.

agreement with that for the ASTRI SST-2M field of view. Thus, the sigma-parameter of the Gaussian spatial distribution of the background of Conf. s9-4-257m is taken to be 10.24 deg^2 (the same value also adopted in *Astrisim*).

4.4 Results

I obtained VHE count maps of Vela X using simulations performed with *ctools* and *Astrisim*. I simulated a 53.1-hour observation of the Vela X region with the CTA-South array, assuming 65%/35% relative contribution of the radio/X-ray populations of emitters to the very high energy gamma-ray diffuse morphology of the Vela PWN. Resulting VHE count maps obtained from the *Parkes* and MOST radio templates are shown in Figs. 4.8 and 4.9, respectively. I also examined cases in which the VHE Vela X surface brightness is modeled entirely with the X-ray (Fig. 4.10) or radio (Figs. 4.11 and 4.12) templates. In Fig 4.13 the H.E.S.S. surface brightness map from [25] is compared with the simulated CTA-South and the ASTRI mini-array 53.1-hour observations.

Since the resolving capability of a typical IACT improves with energy, in Figs. 4.8-4.15 I smoothed count maps according to the different angular resolutions of the corresponding

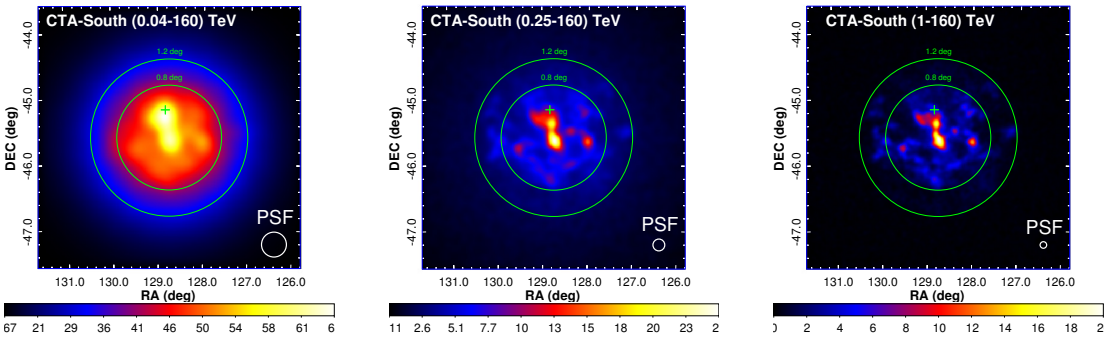

(A) $E > 0.04$ TeV (B) $E > 0.25$ TeV (C) $E > 1$ TeV

FIGURE 4.9: Same as Fig. 4.8 for the high-resolution MOST radio template.

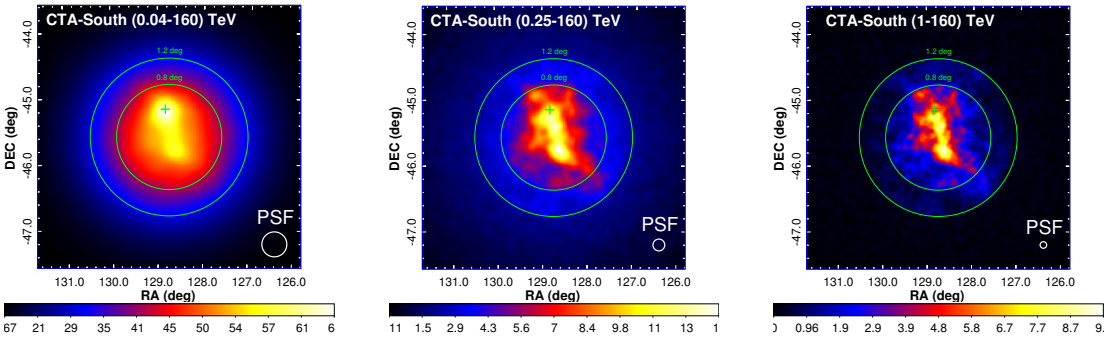

(A) $E > 0.04$ TeV (B) $E > 0.25$ TeV (C) $E > 1$ TeV

FIGURE 4.10: Same as Fig. 4.8 adopting only the X-ray template to describe the diffuse emission.

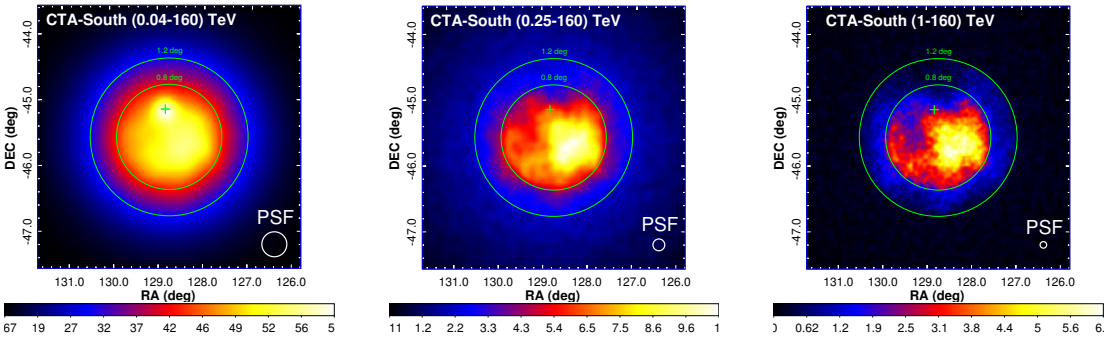

(A) $E > 0.04$ TeV (B) $E > 0.25$ TeV (C) $E > 1$ TeV

FIGURE 4.11: Same as Fig. 4.8 adopting only the *Parkes* radio template to describe the diffuse emission.

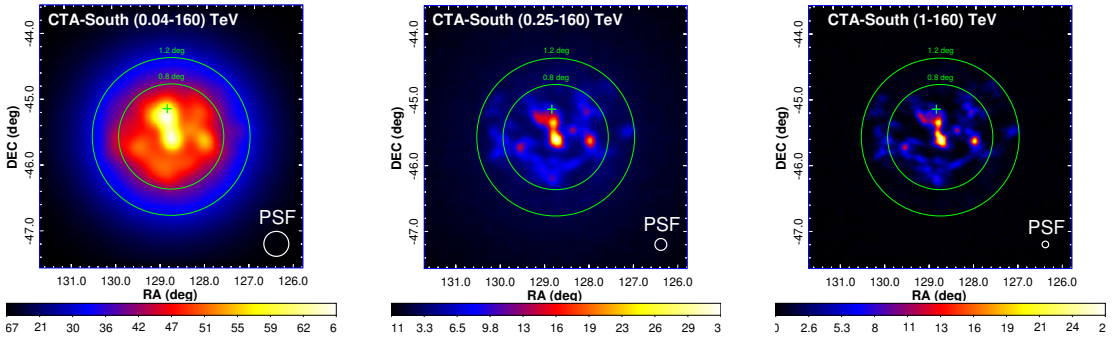

(A) $E > 0.04$ TeV (B) $E > 0.25$ TeV (C) $E > 1$ TeV

FIGURE 4.12: Same as Fig. 4.8 adopting only the MOST radio template to describe the diffuse emission.

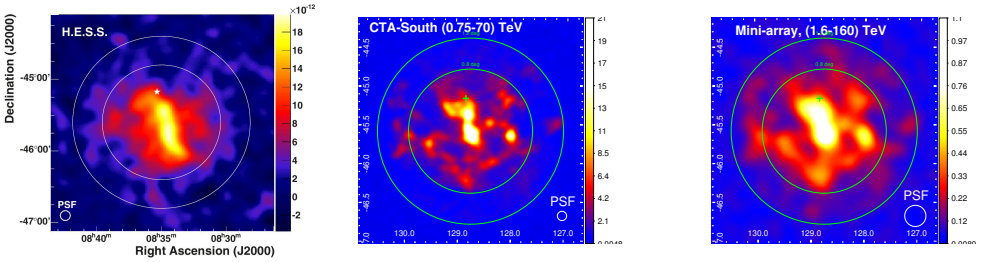

(A) (B) (C)

FIGURE 4.13: Comparison of *ctools* simulations with H.E.S.S. observations. (A) Sky-map of the H.E.S.S. observations taken from [25], smoothed with 0.07°. The color bar shows the surface brightness in cm^{-2} s^{-1} deg^{-2}. (B)/(C) Simulated count maps for the CTA-South/ASTRI mini-array (Conf. s9-4-257m, Mini-array) configurations. The exposure time is 53.1 hours. x-, y- axes are the right ascension (RA) and declination (DEC). The color bars represent the number of counts. All count maps are smoothed according to the size of the corresponding PSF (white circles). See text for details. Circles have radii of 0.8° and 1.2°, respectively. The cross/star marks to the the Vela pulsar position.

instruments. Smoothing radii adopted here are equal to the 68% of the containment radii (r_{68}) of the gamma-ray PSFs at the lower limit of the corresponding energy ranges[13].

The resulting significances S of the Vela pulsar detection with CTA-South and the ASTRI mini-array during a 53.1-hour exposure are listed in Table 4.3.

Astrisim and *ctools* simulations of Vela X are shown in Figs. 4.14 and 4.15. For both count maps, I calculated intensity profiles along an horizontal ($13° \times 0.5°$) and a vertical ($0.5° \times 13°$) strip containing the entire central cocoon[14]. Resulting profiles are compared in Fig. 4.16.

[13]For the CTA-South $r_{68} = 0.19°$ at 0.04 TeV, $r_{68} = 0.09°$ at 0.25 TeV, $r_{68} = 0.06°$ at 0.75 TeV and $r_{68} = 0.05°$ at 1 TeV. For the ASTRI mini-array $r_{68} = 0.14°$ at 1.6 TeV.

[14]These horizontal and vertical regions are marked in Figs. 4.14 and 4.15 as magenta "prof1" and green "prof2" regions, respectively.

TABLE 4.3: Significance S of the Vela pulsar detection with CTA-South and the ASTRI mini-array (Conf. s9-4-257m, Mini-array) in different energy ranges. Duration of observation is 53.1 hours.

Array	Energy range	Significance $S \sim \sqrt{\text{TS}}$
CTA-South:		
	0.04–160 TeV	39.1
	0.25–160 TeV	4.5
	0.75-70 TeV	not signif.
	1–160 TeV	not signif.
Mini-array:		
s9-4-257m	1.6–160 TeV	not signif.

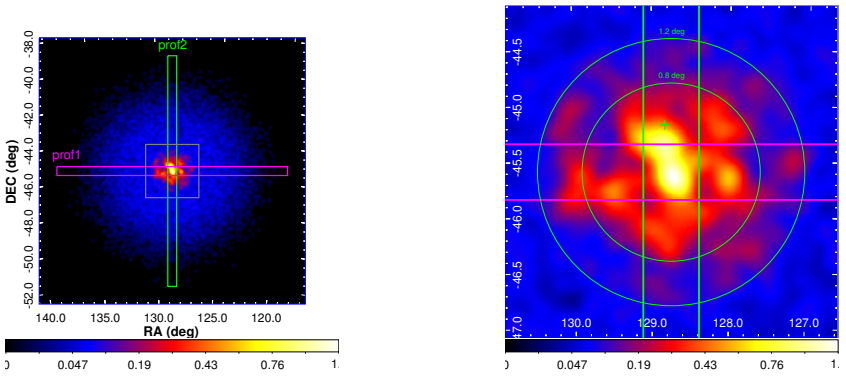

FIGURE 4.14: *Astrisim* simulations of Vela X with the ASTRI mini-array (Conf. s9-4-257m): (A) the whole $15° \times 15°$ count map, centered at $\alpha_0 = 128.75°$ and $\delta_0 = -45.6°$; (B) zoom in of the central part (grey box in panel (A)). The exposure time is 53.1 hours. x-, y- axes are the right ascension (RA) and declination (DEC) in degrees, respectively. The color bars represent the number of counts in the square root scale. Count maps are smoothed according to the size of the corresponding PSF (white circles). See text for details. The intensity profiles shown in Fig. 4.16 are calculated along the strips bound by the magenta and green lines (regions "prof1" and "prof2", respectively). Circles have radii of 0.8° and 1.2°, respectively. The cross marks the Vela pulsar position.

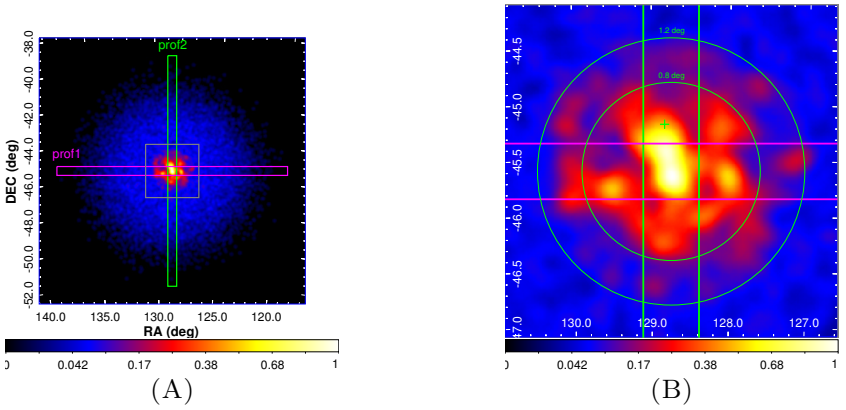

FIGURE 4.15: Same as Fig. 4.14 for *ctools* simulations.

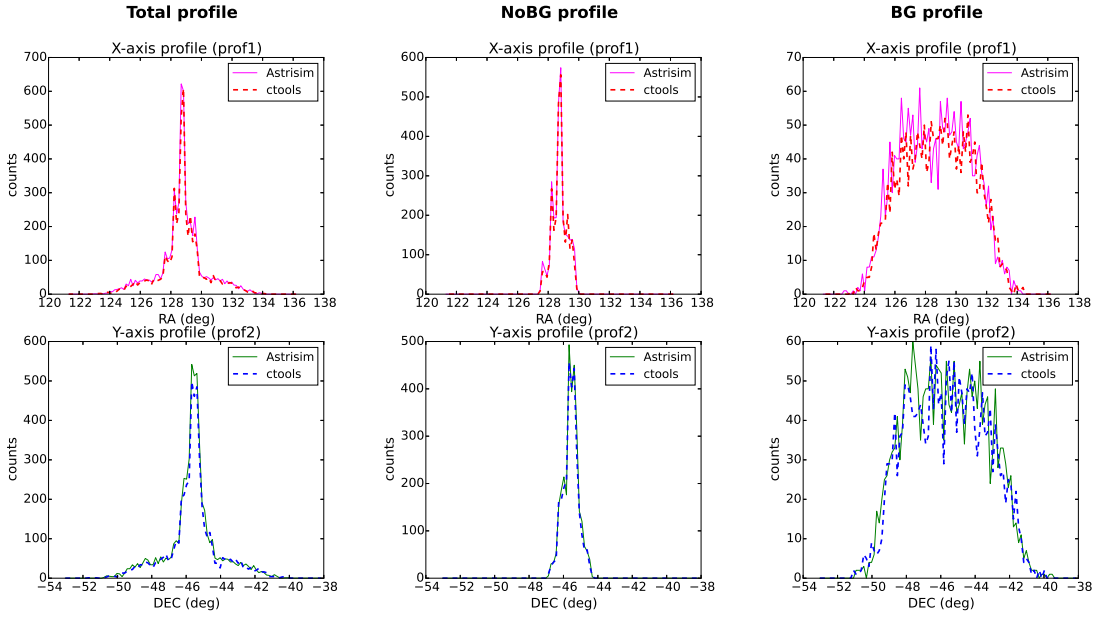

(A) (B) (C)

FIGURE 4.16: *Astrisim* and *ctools* spatial profiles of the Vela X count maps for the total emission (A), the background subtracted emission (B) and only the background emission (C). The x-axis corresponds to the coordinate (in degrees), along which a profile is calculated. the y-axis represents the number of counts. Top panels show horizontal profiles, whereas bottom panels vertical profiles. The solid/dashed line is the *Astrisim*/*ctools* profile, measured along regions shown in Fig. 4.15.A.

4.5 Discussion

I presented simulations of the VHE gamma-ray emission from the Vela X region, which were carried out under different assumptions concerning the morphology of the diffuse emission from the Vela X PWN.

4.5.1 Detection of the Vela Pulsar

In Chapter 2, I used a uniform disk template from the *Fermi* Science Tools, as a spatial model and a power law, obtained from the *Fermi*-analysis at energies >10 GeV and extrapolated to VHE, as a spectral model of the extended Vela X source. Here, I adopted spatially resolved Vela X models and the H.E.S.S. TeV spectra to perform more accurate VHE gamma-ray simulations of the Vela X region and to calculate the detection significance of the Vela pulsar with CTA. I found that PSR J0835−4510 will be significantly detected ($\sim 39\sigma$) with CTA-South in 53.1 hours at energies >0.04 TeV (see Table 4.3). However, there is no prominent point-like signal on the top of the diffuse emission in the TeV energy band.

In order to compare the results from this analysis with those from Chapter 2, I simulated 25-hour observations with CTA-South at energies >0.04 and obtained a detection significance of $\sim 27\sigma$ for the Vela pulsar. This value is consistent with that resulting from the general analysis of HE *Fermi* pulsars[15], described in Chapter 2.

4.5.2 Investigation of the Vela PWN morphology

In addition to the the Vela pulsar, the high sensitivity and angular resolution of CTA will allow us to perform detailed studies of the Vela X diffuse emission. Assuming that the VHE gamma-ray Vela X morphology is intermediate between those at radio and X-ray wavelengths, I adopted high-resolution radio (MOST) and X-ray (ROSAT) observations as spatial templates to model it. The contribution of the radio and X-ray populations to the emitted flux of the Vela PWN are 65% and 35%, respectively [25]. Although at a few tens of GeV the CTA angular resolution is relatively poor ($\sim 0.2^\circ$), above 1 TeV it is better than $\sim 0.05^\circ$. Therefore, as shown in Fig. 4.13, a CTA-South observation of 53.1 hours at energies >0.75 TeV will provide a much detailed sky-map of the Vela X region as compared to the H.E.S.S. results [25]. The PSF of the ASTRI mini-array at 1.6 TeV (0.14°) is slightly broader than that of H.E.S.S. at 1 TeV (0.07°). Nevertheless, it will be sensitive enough to carry out detailed high-energy observations of the this region (Fig. 4.13C). The ASTRI mini-array will be capable to detect the central/outer part of Vela X at significance of $\sim 5\sigma$ within 0.5/2 hours, and at significance of $\sim 10\sigma$ in 2/10 hours. The full CTA-South array will detect the Vela X diffuse emission with a significance $S = 5$ in several minutes.

I performed simulations also with the radio templates obtained from the *Parkes* radio observations, used in the morphological studies of Abramowski et al. [25]. The angular resolution of the radio sky-map is about 0.17° (HPBW), broader than the typical PSF of IACTs. A comparison of these simulations with the H.E.S.S. observations and other higher resolution simulations (Figs. 4.8, 4.9 and 4.11) shows the importance of an accurate modeling of the spatial maps to reveal the capabilities of future IACTs.

High-resolution CTA sky-maps will help in understanding the nature of the Vela X extended emission through the detailed comparison of its VHE morphology with those at other wavelengths. Following [25], here I assumed that the Vela X diffuse comes from two populations of leptons: the first population produces the radio and VHE photons, and the second population emits in the X-ray and VHE gamma-ray bands. If the X-ray and radio populations provide a relative contribution to the very high energy flux of 35% and 65%, respectively, CTA will observe the Vela X region as in Fig. 4.9. In case

[15]The analysis of the *Fermi*-LAT data shows significant detection ($S = 28.2$) of the Vela pulsar with CTA-South at energies >0.04 TeV during 25-hour observations (see Table 2.4).

the VHE emission is dominated by the X-ray population of the central cocoon or by the radio population of the extended "wings", the count maps will be similar to those shown in Figs. 4.10 and 4.12, respectively. The quality of the CTA data will be such that high-resolution observations can also confirm whether the TeV gamma-ray emission from Vela X follows the radio filaments- and arcs- structure seen at 843 MHz by MOST [212, 220]. If the two-population leptonic model assumed here is the right one, the high-resolution CTA data will help to determine the contributions of the radio and X-ray populations to the VHE gamma-ray morphology with an accuracy of a few percent.

To check this, I performed a number of similar simulations assuming different contributions of the radio and X-ray populations to the VHE emission from the Vela PWN. To determine to what extent the contributions from these leptonic populations are distinguishable with CTA, I fitted the simulated data with a two-component spectral model (radio and X-ray)[16] of the diffuse Vela X emission with free normalization factors and spectral parameters and obtained the significance of the detection for each of them. The test statistic values of radio and X-ray components of the Vela PWN spectral model obtained in a selection of these simulations are shown in Table 4.4. As can be seen, the significance of the detection of the two populations is very high. In addition, I fitted the data with a single-population spectral model with again free normalization factors and spectral parameters, which contains only the X-ray or radio component of Vela X. I then checked if the quality (log likelihood) of the two-component fit is better than that of the single-component model. For example, simulating observations for a model with 35% of the Vela PWN emission from the X-ray and 65% of the emission from the radio populations at energies >40 GeV, I obtained that the value of log likelihood for the spectral fit with a two-population model equals to -21934552. This value is significantly larger than the values obtained from the spectral fitting with a single-population radio or X-ray model, for which the log likelihoods are -21943075 and -21954956, respectively. I found that two-component models provide a better description of the data for all the models reported in Table 4.4.

I then determined the minimum fractional contribution to the VHE gamma-ray emission from the radio or X-ray populations that can be constrained with CTA. I did it performing simulations varying the fractional contribution of the two populations and fitting them with a two- or one-component spectral model. Detectable fractions are determined imposing that both populations are significantly detected in the spectral fits and that the two-population model provides a better log likelihood than the single-population (radio or X-ray) one. At low energies (>40 GeV) CTA will distinguish[17]

[16] Each component is a superposition of a circular and ring template (see Sect. 4.2).

[17] Emission from two leptonic populations is considered to be distinguishable if both of them are detected with a significance $S > 5$.

TABLE 4.4: Test statistic values of radio (TS_R) and X-ray (TS_X) components of the Vela PWN spectral model for two populations of emitting particles. Energy ranges of simulated data are in the first column. The second column lists the fractional contribution of the radio and X-ray populations to the VHE gamma-ray emission from the Vela PWN.

Energy range	Radio-X-ray fractional contribution	TS_R	TS_X
0.04–160 TeV:			
	R90-X10	240493	372
	R13-X87	369	204079
0.25–160 TeV:			
	R96-X04	293782	429
	R03-X97	190	261532
1–160 TeV:			
	R89-X11	204195	2576
	R13-X87	2445	186473

TS values represent the sum of the test statistics of the spectral components corresponding to the circular and ring regions of Vela X (see Sect. 4.2).

VHE emission from the X-ray and radio spectral component, if the contribution from the X-ray population is more than 10% of the total VHE flux of Vela X and that from the radio population is >13%. At higher energies (>250 GeV), where the background contamination is low and the angular resolution of CTA is rather good (∼5 arcmin), it will be possible to disentangle the emission from the radio and X-ray population, if one of them contributes more than 4% of the VHE flux of Vela X. At energies above 1 TeV, where the number of detected events is low, the populations will be distinguishable with CTA, if their contribution is more than 13%.

I also obtained that the significance of the Vela pulsar detection with CTA at energies >40 GeV does not change dramatically in all these cases (e.g. $S \sim 39$).

It should be noted that at present a number of questions challenges the two-population leptonic scenario. According to this model, it is reasonable to expect differences in the VHE spectra between the inner (circular area) and outer (ring) parts of the Vela X diffuse emission. However, no such spectral variations have been observed in [25]. Furthermore, the extended TeV emission ("wings") from Vela X can not be explained by present two-leptonic theoretical models (e.g. [214]). Therefore, future CTA investigations are very important for extending the multiwavelength study of the Vela PWN emission up to ∼300 TeV and for improving our understanding of this source.

Finally, in this analysis I compared also *ctools* and *Astrisim*, simulations of the Vela X region and found that the intensity profiles built from the sky-maps produced by these

two softwares are consistent with each other (see Fig. 4.16).

4.6 Conclusions

Investigations of the Vela X region with CTA will allow us to detect the Vela pulsar in the energy range from several tens of GeV up to a few hundreds of TeV. Such observations will certainly boots our understanding concerning the nature of the gamma-ray emission from relatively old PWNe, as the Vela PWN. The high-resolution data achieved with CTA will be very important to carry out morphological studies of such sources and also for understanding the origin of the VHE gamma-ray emission in them.

I found also that preliminary investigations of the Vela X diffuse emission will be possible with the precursors of the CTA southern installation, like the ASTRI mini-array. A pure detection of the extended morphology will be possible in several hours, whereas in 50 hours such an array will provide a detailed image of the Vela X region in the broad energy range from 1 to 160 TeV.

Chapter 5

Conclusions and Future Work

5.1 Conclusions

In this Thesis I studied the prospects for investigations of gamma-ray pulsars with the next-generation Cherenkov facility – CTA. I performed a number of different simulations in order to estimate how many isolated neutron stars can be detected with CTA at VHE and what type of detailed studies of the brightest pulsars will be possible.

Pulsars are unique laboratories in our Galaxy and are investigated in different energy bands. The processes originating in the vicinity of these objects occur under conditions unachievable on Earth. The activity of pulsars affects also the circumstellar environment creating a bright nebula (PWN). A significant improvement in understanding the gamma-ray emission from such sources occurred after the detection of a large sample of pulsars ($\sim$150) with the currently operating gamma-ray telescopes as *Fermi* and AGILE. However, so far only the Crab pulsar has been detected at VHE (>100 GeV). This rises new questions concerning the mechanism of the VHE gamma-ray emission. Detection of other gamma-ray pulsars at VHE is required to compare their characteristics and to test different theoretical models. Observations of a sample of pulsars in the energy range from 100 GeV up to several TeV will help us to clarify whether the VHE emission is intrinsic to all gamma-ray pulsars or specific only to the Crab pulsar. CTA is the best future instrument for such investigations. It is designed to perform observations with a quality better than that of any presently operating IACT.

We started our investigations analyzing the VHE light curve and timing properties of the Crab pulsar. This pulsar is sufficiently bright at VHE for an accurate measurement of its pulse profile. In comparison with lower energy bands, VHE gamma-ray observations with current IACTs (MAGIC, VERITAS) yielded rather uncertain measurements of

the positions of both the main pulse and interpulse. Using the results obtained with MAGIC, we simulated the light curve of the Crab pulsar with different configurations of CTA (including the ASTRI mini-array) and varying the VHE spectral index of the Crab pulsar. With the improved sensitivity of CTA, it will be possible to obtain accurate measurements of the light curve, comparable with those at lower energies. This will expand the multiwavelength timing analysis of the Crab pulsar up to VHE. We also studied if an independent VHE timing analysis is feasible with CTA.

The detection of the Crab pulsar at energies >100 GeV excluded the existence of a steep exponential cut-off tail of its spectrum at GeV energies, as found at lower energies with the *Fermi*-LAT. In collaboration with Takayuki Saito we analyzed the most energetic gamma-ray pulsars detected with the *Fermi*-LAT. We simulated VHE observations of these sources with CTA, assuming a power-law spectrum above 10 GeV obtained from an extrapolation of the tail of the *Fermi* spectrum. Our aim was to determine which of them can be detected with CTA with a 50-hour exposure. We also checked whether some of them can be observed during the CTA KSPs.

We were also interested in analyzing another bright gamma-ray source, which is connected with pulsars activity, – the Vela X region. This object corresponds to the pulsar-PWN complex and has diffuse emission detected at different wavelengths. Adopting different spatial templates and the spectral model obtained with H.E.S.S., we simulated the VHE gamma-ray emission from the Vela PWN assuming that its morphology is intermediate between those in the radio and X-ray bands. Simulations were performed using different software packages (*ctools* and *Astrisim*). In addition, we obtained realistic estimates of the significance of the Vela pulsar detection with CTA. High-resolution on the extended Vela X emission in VHE gamma rays can shed light on the acceleration processes occurring inside the nebula and can allow us to disentangle the different populations of charged particles responsible for the emission from different regions of the Vela PWN. We used these simulations to estimate also the resolving capabilities of CTA and the ASTRI mini-array and to compare the performances of the *ctools* and *Astrisim* softwares.

Our main results can be summarized as follows:

- CTA will detect about 10 gamma-ray pulsars from the *Fermi* sample considered here in 50 hours. Some of them will be observed within the framework of the CTA KSPs with smaller exposure times, which can provide upper limits to the pulsars flux.
- The VHE timing properties of the Crab pulsar can be accurately measured with CTA. Conservatively assuming a spectral index Γ=3.57, with a 70-hour observation

it will be possible to achieve uncertainties in the position of the interpulse equal to $\sim$12 μs and $\sim$50 μs in the 0.04–0.1 TeV and 0.1–1 TeV energy ranges, respectively.

- An independent VHE timing analysis of the Crab pulsar is feasible with the LSTs. Three 1-hour long observations repeated 3 or 7 consecutive nights provide an accuracy in determining the time of arrival of the interpulse at the level of $\sim$80 μs and $\sim$65 μs, respectively.

- Detailed investigations of the Vela X region resulted in the detection of the Vela pulsar during a $\sim$50-hour CTA observation with significances of 39σ and 4.5σ at energies >40 GeV and >250 GeV, respectively.

- The diffuse emission from the Vela PWN can be significantly detected at a 5σ level with CTA/ASTRI mini-array in several minutes/hours. Detailed morphological studies of the Vela X region will be possible in a 50-hour observation.

- All simulations showed that SSTs will be not efficient for observations of gamma-ray pulsars at energies above few TeV.

In performing these simulations we made a number of assumptions. For the pulsars which are not detected at VHE, I obtained the spectra in the 10-100 GeV energy range analyzing the *Fermi*-LAT data and extrapolated them up to the $\sim$100 TeV. To investigate the VHE timing properties of the Crab pulsar, I adopted the MAGIC light curve and assumed that its shape does not change significantly with energy from 0.04 up to 160 TeV. Simulating the Vela X region, I modeled the morphology of the VHE gamma-ray diffuse emission as a superposition of the radio and the X-ray brightness maps.

Although pulsars are not among the brightest sources in the VHE gamma-ray sky, thanks mainly to the LSTs and MSTs, CTA will be sensitive enough to obtain a number of unprecedented results, as mentioned above.

5.2 Future Work

As a part of my future work, I am planning to improve simulations of the high-energy *Fermi* pulsars using all available *Fermi*-LAT data acquired during more than 7 years. After building a new timing solution valid over the whole 7-year time interval, it will be possible to fold the light curve of each pulsar and increase the statistics of the on- and off- pulse phase intervals. With this I will improve the spectral analysis at high energies (>10 GeV) and perform more realistic VHE simulations.

In collaboration with Diego Torres and Emma de Oña-Wilhelmi, I am currently investigating the gamma-ray emission from Galactic GCs. As mentioned in Chapter 1, unpulsed high-energy emission could probably be associated with a collective flux of gamma rays emitted by a population of MSPs inside the globular cluster. A dozen of GCs was detected with the *Fermi*-LAT to date. An analysis of their spectra using the new Pass 8 data can provide estimates of the size of the MSP population in each cluster. Extrapolating these spectra to the VHE energy range, it will be possible to make predictions concerning the detectability of GCs with CTA.

Bibliography

[1] T. C. Weekes, M. F. Cawley, D. J. Fegan, et al. Observation of TeV gamma rays from the Crab nebula using the atmospheric Cerenkov imaging technique. *ApJ*, 342:379–395, July 1989. doi: 10.1086/167599.

[2] S. P. Wakely and D. Horan. TeVCat: An online catalog for Very High Energy Gamma-Ray Astronomy. *International Cosmic Ray Conference*, 3:1341–1344, 2008.

[3] S. Carrigan, F. Brun, R. C. G. Chaves, et al. The H.E.S.S. Galactic Plane Survey - maps, source catalog and source population. *[arXiv:1307.4690]*, July 2013.

[4] H.E.S.S. Collaboration, A. Abramowski, F. Acero, et al. Discovery of gamma-ray emission from the extragalactic pulsar wind nebula N 157B with H.E.S.S. *A&A*, 545:L2, September 2012. doi: 10.1051/0004-6361/201219906.

[5] F. V. Coroniti. Magnetically striped relativistic magnetohydrodynamic winds - The Crab Nebula revisited. *ApJ*, 349:538–545, February 1990. doi: 10.1086/168340.

[6] C. F. Kennel and F. V. Coroniti. Magnetohydrodynamic model of Crab nebula radiation. *ApJ*, 283:710–730, August 1984. doi: 10.1086/162357.

[7] A. A. Abdo, M. Ackermann, M. Ajello, et al. Gamma-Ray Flares from the Crab Nebula. *Science*, 331:739–, February 2011. doi: 10.1126/science.1199705.

[8] F. A. Aharonian, S. V. Bogovalov, and D. Khangulyan. Abrupt acceleration of a 'cold' ultrarelativistic wind from the Crab pulsar. *Nature*, 482:507–509, February 2012. doi: 10.1038/nature10793.

[9] J. Aleksić, S. Ansoldi, L. A. Antonelli, et al. Measurement of the Crab Nebula spectrum over three decades in energy with the MAGIC telescopes. *Journal of High Energy Astrophysics*, 5:30–38, March 2015. doi: 10.1016/j.jheap.2015.01.002.

[10] A. A. Abdo, M. Ackermann, M. Ajello, et al. Fermi Large Area Telescope Observations of the Crab Pulsar And Nebula. *ApJ*, 708:1254–1267, January 2010. doi: 10.1088/0004-637X/708/2/1254.

[11] M. Tavani, A. Bulgarelli, V. Vittorini, et al. Discovery of Powerful Gamma-Ray Flares from the Crab Nebula. *Science*, 331:736–, February 2011. doi: 10.1126/science.1200083.

[12] R. Buehler, J. D. Scargle, R. D. Blandford, et al. Gamma-Ray Activity in the Crab Nebula: The Exceptional Flare of 2011 April. *ApJ*, 749:26, April 2012. doi: 10.1088/0004-637X/749/1/26.

[13] W. Bednarek and W. Idec. On the variability of the GeV and multi-TeV gamma-ray emission from the Crab nebula. *MNRAS*, 414:2229–2234, July 2011. doi: 10.1111/j.1365-2966.2011.18539.x.

[14] M. Lyutikov, N. Otte, and A. McCann. The Very High Energy Emission from Pulsars: A Case for Inverse Compton Scattering. *ApJ*, 754:33, July 2012. doi: 10.1088/0004-637X/754/1/33.

[15] D. A. Uzdensky, B. Cerutti, and M. C. Begelman. Reconnection-powered Linear Accelerator and Gamma-Ray Flares in the Crab Nebula. *ApJ*, 737:L40, August 2011. doi: 10.1088/2041-8205/737/2/L40.

[16] B. Cerutti, G. R. Werner, D. A. Uzdensky, and M. C. Begelman. Simulations of Particle Acceleration beyond the Classical Synchrotron Burnoff Limit in Magnetic Reconnection: An Explanation of the Crab Flares. *ApJ*, 770:147, June 2013. doi: 10.1088/0004-637X/770/2/147.

[17] A. P. Lobanov, D. Horns, and T. W. B. Muxlow. VLBI imaging of a flare in the Crab nebula: more than just a spot. *A&A*, 533:A10, September 2011. doi: 10.1051/0004-6361/201117082.

[18] M. Mariotti. No significant enhancement in the VHE gamma-ray flux of the Crab Nebula measured by MAGIC in September 2010. *The Astronomer's Telegram*, 2967:1, October 2010.

[19] E. Aliu, S. Archambault, T. Aune, et al. A Search for Enhanced Very High Energy Gamma-Ray Emission from the 2013 March Crab Nebula Flare. *ApJ*, 781:L11, January 2014. doi: 10.1088/2041-8205/781/1/L11.

[20] A. Abramowski, F. Aharonian, H. E. S. S. Collaboration, et al. H.E.S.S. observations of the Crab during its March 2013 GeV gamma-ray flare. *A&A*, 562:L4, February 2014. doi: 10.1051/0004-6361/201323013.

[21] F. Aharonian, A. G. Akhperjanian, A. R. Bazer-Bachi, et al. Observations of the Crab nebula with HESS. *A&A*, 457:899–915, October 2006. doi: 10.1051/0004-6361:20065351.

[22] Kevin Meagher for the VERITAS Collaboration. Six years of VERITAS observations of the Crab Nebula. *[arXiv:1508.06442]*, August 2015.

[23] F. Aharonian, A. G. Akhperjanian, K.-M. Aye, et al. A New Population of Very High Energy Gamma-Ray Sources in the Milky Way. *Science*, 307:1938–1942, March 2005. doi: 10.1126/science.1108643.

[24] S. Funk, J. A. Hinton, Y. Moriguchi, et al. XMM-Newton observations of HESS J1813-178 reveal a composite Supernova remnant. *A&A*, 470:249–257, July 2007. doi: 10.1051/0004-6361:20066779.

[25] A. Abramowski, F. Acero, F. Aharonian, et al. Probing the extent of the non-thermal emission from the Vela X region at TeV energies with H.E.S.S. *A&A*, 548: A38, December 2012. doi: 10.1051/0004-6361/201219919.

[26] F. Aharonian, A. G. Akhperjanian, A. R. Bazer-Bachi, et al. Energy dependent γ-ray morphology in the pulsar wind nebula HESS J1825-137. *A&A*, 460:365–374, December 2006. doi: 10.1051/0004-6361:20065546.

[27] J. M. Blondin, R. A. Chevalier, and D. M. Frierson. Pulsar Wind Nebulae in Evolved Supernova Remnants. *ApJ*, 563:806–815, December 2001. doi: 10.1086/324042.

[28] H.-T. Janka. Explosion Mechanisms of Core-Collapse Supernovae. *Annual Review of Nuclear and Particle Science*, 62:407–451, November 2012. doi: 10.1146/annurev-nucl-102711-094901.

[29] A. Burrows. Colloquium: Perspectives on core-collapse supernova theory. *Reviews of Modern Physics*, 85:245–261, January 2013. doi: 10.1103/RevModPhys.85.245.

[30] W. Hillebrandt and J. C. Niemeyer. Type IA Supernova Explosion Models. *ARA&A*, 38:191–230, 2000. doi: 10.1146/annurev.astro.38.1.191.

[31] D. Maoz and F. Mannucci. Type-Ia Supernova Rates and the Progenitor Problem: A Review. *PASA*, 29:447–465, January 2012. doi: 10.1071/AS11052.

[32] F. Aharonian, A. G. Akhperjanian, A. R. Bazer-Bachi, et al. A detailed spectral and morphological study of the gamma-ray supernova remnant RX J1713.7-3946 with HESS. *A&A*, 449:223–242, April 2006. doi: 10.1051/0004-6361:20054279.

[33] F. Aharonian, A. G. Akhperjanian, A. R. Bazer-Bachi, et al. H.E.S.S. Observations of the Supernova Remnant RX J0852.0-4622: Shell-Type Morphology and Spectrum of a Widely Extended Very High Energy Gamma-Ray Source. *ApJ*, 661: 236–249, May 2007. doi: 10.1086/512603.

[34] J. Albert, E. Aliu, H. Anderhub, et al. Observation of VHE γ-rays from Cassiopeia A with the MAGIC telescope. *A&A*, 474:937–940, November 2007. doi: 10.1051/0004-6361:20078168.

[35] V. A. Acciari, E. Aliu, T. Arlen, et al. Observations of the Shell-type Supernova Remnant Cassiopeia A at TeV Energies with VERITAS. *ApJ*, 714:163–169, May 2010. doi: 10.1088/0004-637X/714/1/163.

[36] V. A. Acciari, E. Aliu, T. Arlen, et al. Discovery of TeV Gamma-ray Emission from Tycho's Supernova Remnant. *ApJ*, 730:L20, April 2011. doi: 10.1088/2041-8205/730/2/L20.

[37] F. Acero, F. Aharonian, A. G. Akhperjanian, et al. First detection of VHE γ-rays from SN 1006 by HESS. *A&A*, 516:A62, June 2010. doi: 10.1051/0004-6361/200913916.

[38] A. R. Bell. The acceleration of cosmic rays in shock fronts. I. *MNRAS*, 182: 147–156, January 1978.

[39] L. Drury. On particle acceleration in supernova remnants. *Space Sci. Rev.*, 36: 57–60, September 1983. doi: 10.1007/BF00171901.

[40] K. Koyama, R. Petre, E. V. Gotthelf, et al. Evidence for shock acceleration of high-energy electrons in the supernova remnant SN1006. *Nature*, 378:255–258, November 1995. doi: 10.1038/378255a0.

[41] Y. Uchiyama, F. A. Aharonian, T. Tanaka, T. Takahashi, and Y. Maeda. Extremely fast acceleration of cosmic rays in a supernova remnant. *Nature*, 449: 576–578, October 2007. doi: 10.1038/nature06210.

[42] M. Ackermann, M. Ajello, A. Allafort, et al. Detection of the Characteristic Pion-Decay Signature in Supernova Remnants. *Science*, 339:807–811, February 2013. doi: 10.1126/science.1231160.

[43] T. Nakamori, H. Katagiri, H. Sano, et al. Simulating Cherenkov Telescope Array observation of RX J1713.7-3946. *[arXiv:1508.06052]*, August 2015.

[44] M. Casse and J. A. Paul. Local gamma rays and cosmic-ray acceleration by supersonic stellar winds. *ApJ*, 237:236–243, April 1980. doi: 10.1086/157863.

[45] E. Aliu, T. Aune, B. Behera, et al. Spatially Resolving the Very High Energy Emission from MGRO J2019+37 with VERITAS. *ApJ*, 788:78, June 2014. doi: 10.1088/0004-637X/788/1/78.

[46] A. Abramowski, F. Acero, F. Aharonian, et al. Discovery of extended VHE γ-ray emission from the vicinity of the young massive stellar cluster Westerlund 1. *A&A*, 537:A114, January 2012. doi: 10.1051/0004-6361/201117928.

[47] V. Bosch-Ramon. Multifrequency Behavior of Microquasars in the GeV-TeV era: A review . *Mem. Soc. Astron. Italiana*, 83:194, 2012.

[48] J. Zhang, B. Xu, and J. Lu. Origin of Multi-band Emission from the Microquasar Cygnus X-1. *ApJ*, 788:143, June 2014. doi: 10.1088/0004-637X/788/2/143.

[49] G. Dubus, A. Lamberts, and S. Fromang. Modelling the high-energy emission from gamma-ray binaries using numerical relativistic hydrodynamics. *A&A*, 581: A27, September 2015. doi: 10.1051/0004-6361/201425394.

[50] F. Aharonian, A. G. Akhperjanian, K.-M. Aye, et al. Discovery of the binary pulsar PSR B1259-63 in very-high-energy gamma rays around periastron with HESS. *A&A*, 442:1–10, October 2005. doi: 10.1051/0004-6361:20052983.

[51] F. A. Aharonian, A. G. Akhperjanian, A. R. Bazer-Bachi, et al. Discovery of a point-like very-high-energy γ-ray source in Monoceros. *A&A*, 469:L1–L4, July 2007. doi: 10.1051/0004-6361:20077299.

[52] F. Aharonian, A. G. Akhperjanian, A. R. Bazer-Bachi, et al. 3.9 day orbital modulation in the TeV γ-ray flux and spectrum from the X-ray binary LS 5039. *A&A*, 460:743–749, December 2006. doi: 10.1051/0004-6361:20065940.

[53] J. Albert, E. Aliu, H. Anderhub, et al. Periodic Very High Energy γ-Ray Emission from LS I +61°303 Observed with the MAGIC Telescope. *ApJ*, 693:303–310, March 2009. doi: 10.1088/0004-637X/693/1/303.

[54] V. A. Acciari, M. Beilicke, G. Blaylock, et al. VERITAS Observations of the γ-Ray Binary LS I +61 303. *ApJ*, 679:1427–1432, June 2008. doi: 10.1086/587736.

[55] J. Albert, E. Aliu, H. Anderhub, et al. Very High Energy Gamma-Ray Radiation from the Stellar Mass Black Hole Binary Cygnus X-1. *ApJ*, 665:L51–L54, August 2007. doi: 10.1086/521145.

[56] H.E.S.S. Collaboration, A. Abramowski, F. Aharonian, et al. The exceptionally powerful TeV γ-ray emitters in the Large Magellanic Cloud. *Science*, 347:406–412, January 2015. doi: 10.1126/science.1261313.

[57] R. P. van der Marel. The Large Magellanic Cloud: structure and kinematics. In M. Livio and T. M. Brown, editors, *The Local Group as an Astrophysical Laboratory*, pages 47–71, 2006.

[58] G. Pietrzyński, D. Graczyk, W. Gieren, et al. An eclipsing-binary distance to the Large Magellanic Cloud accurate to two per cent. *Nature*, 495:76–79, March 2013. doi: 10.1038/nature11878.

[59] C. Badenes, D. Maoz, and B. T. Draine. On the size distribution of supernova remnants in the Magellanic Clouds. *MNRAS*, 407:1301–1313, September 2010. doi: 10.1111/j.1365-2966.2010.17023.x.

[60] B. Lawton, K. D. Gordon, B. Babler, et al. Spitzer Analysis of H II Region Complexes in the Magellanic Clouds: Determining a Suitable Monochromatic Obscured Star Formation Indicator. *ApJ*, 716:453–473, June 2010. doi: 10.1088/0004-637X/716/1/453.

[61] B. C. Dunne, S. D. Points, and Y.-H. Chu. X-Rays from Superbubbles in the Large Magellanic Cloud. VI. A Sample of Thirteen Superbubbles. *ApJS*, 136:119–135, September 2001. doi: 10.1086/321794.

[62] S. Kim, M. A. Dopita, L. Staveley-Smith, and M. S. Bessell. H I Shells in the Large Magellanic Cloud. *AJ*, 118:2797–2823, December 1999. doi: 10.1086/301116.

[63] J. Aleksić, S. Ansoldi, L. A. Antonelli, et al. Black hole lightning due to particle acceleration at subhorizon scales. *Science*, 346:1080–1084, November 2014. doi: 10.1126/science.1256183.

[64] J. Holder. TeV gamma-ray astronomy: A summary. *Astroparticle Physics*, 39: 61–75, December 2012. doi: 10.1016/j.astropartphys.2012.02.014.

[65] F. M. Rieger, E. de Oña-Wilhelmi, and F. A. Aharonian. TeV astronomy. *Frontiers of Physics*, 8:714–747, December 2013. doi: 10.1007/s11467-013-0344-6.

[66] J. Biteau and D. A. Williams. The Extragalactic Background Light, the Hubble Constant, and Anomalies: Conclusions from 20 Years of TeV Gamma-Ray Observations. *ApJ*, 812:60, October 2015. doi: 10.1088/0004-637X/812/1/60.

[67] F. Tavecchio, G. Ghisellini, G. Bonnoli, and L. Foschini. Extreme TeV blazars and the intergalactic magnetic field. *MNRAS*, 414:3566–3576, July 2011. doi: 10.1111/j.1365-2966.2011.18657.x.

[68] VERITAS Collaboration, V. A. Acciari, E. Aliu, et al. A connection between star formation activity and cosmic rays in the starburst galaxy M82. *Nature*, 462: 770–772, December 2009. doi: 10.1038/nature08557.

[69] A. Abramowski, F. Acero, F. Aharonian, et al. Spectral Analysis and Interpretation of the γ-Ray Emission from the Starburst Galaxy NGC 253. *ApJ*, 757:158, October 2012. doi: 10.1088/0004-637X/757/2/158.

[70] P. Mészáros. Gamma-ray bursts. *Reports on Progress in Physics*, 69:2259–2321, August 2006. doi: 10.1088/0034-4885/69/8/R01.

[71] S. Inoue, J. Granot, P. T. O'Brien, et al. Gamma-ray burst science in the era of the Cherenkov Telescope Array. *Astroparticle Physics*, 43:252–275, March 2013. doi: 10.1016/j.astropartphys.2013.01.004.

[72] T. Bringmann and C. Weniger. Gamma ray signals from dark matter: Concepts, status and prospects. *Physics of the Dark Universe*, 1:194–217, November 2012. doi: 10.1016/j.dark.2012.10.005.

[73] J. Albert, E. Aliu, H. Anderhub, et al. Observation of Gamma Rays from the Galactic Center with the MAGIC Telescope. *ApJ*, 638:L101–L104, February 2006. doi: 10.1086/501164.

[74] A. Abramowski, F. Acero, F. Aharonian, et al. Search for a Dark Matter Annihilation Signal from the Galactic Center Halo with H.E.S.S. *Physical Review Letters*, 106(16):161301, April 2011. doi: 10.1103/PhysRevLett.106.161301.

[75] A. Archer, A. Barnacka, M. Beilicke, et al. Very-high Energy Observations of the Galactic Center Region by VERITAS in 2010-2012. *ApJ*, 790:149, August 2014. doi: 10.1088/0004-637X/790/2/149.

[76] J. Aleksić, L. A. Antonelli, P. Antoranz, et al. MAGIC Gamma-ray Telescope Observation of the Perseus Cluster of Galaxies: Implications for Cosmic Rays, Dark Matter, and NGC 1275. *ApJ*, 710:634–647, February 2010. doi: 10.1088/0004-637X/710/1/634.

[77] T. Arlen, T. Aune, M. Beilicke, et al. Constraints on Cosmic Rays, Magnetic Fields, and Dark Matter from Gamma-Ray Observations of the Coma Cluster of Galaxies with VERITAS and Fermi. *ApJ*, 757:123, October 2012. doi: 10.1088/0004-637X/757/2/123.

[78] A. Abramowski, F. Aharonian, F. Ait Benkhali, et al. Search for dark matter annihilation signatures in H.E.S.S. observations of dwarf spheroidal galaxies. *Phys. Rev. D*, 90(11):112012, December 2014. doi: 10.1103/PhysRevD.90.112012.

[79] J. E. Kim and G. Carosi. Axions and the strong CP problem. *Reviews of Modern Physics*, 82:557–601, January 2010. doi: 10.1103/RevModPhys.82.557.

[80] G. Galanti, M. Roncadelli, A. De Angelis, and G. F. Bignami. Advantages of axion-like particles for the description of very-high-energy blazar spectra. *[arXiv:1503.04436]*, March 2015.

[81] D. Mattingly. Modern Tests of Lorentz Invariance. *Living Reviews in Relativity*, 8:5, September 2005. doi: 10.12942/lrr-2005-5.

[82] J. Bolmont, V. Vasileiou, A. Jacholkowska, et al. Lorentz invariance violation: The latest Fermi results and the GRB/ AGN complementarity. *Nuclear Instruments and Methods in Physics Research A*, 742:165–168, April 2014. doi: 10.1016/j.nima.2013.10.088.

[83] N. OTTE. Prospects of performing Lorentz invariance tests with VHE emission from Pulsars. *International Cosmic Ray Conference*, 7:256, 2011. doi: 10.7529/ICRC2011/V07/1302.

[84] R. N. Manchester, G. B. Hobbs, A. Teoh, and M. Hobbs. The Australia Telescope National Facility Pulsar Catalogue. *AJ*, 129:1993–2006, April 2005. doi: 10.1086/428488.

[85] R. P. Mignani. Optical, ultraviolet, and infrared observations of isolated neutron stars. *Advances in Space Research*, 47:1281–1293, April 2011. doi: 10.1016/j.asr.2009.12.011.

[86] W. Becker and J. Truemper. The X-ray luminosity of rotation-powered neutron stars. *A&A*, 326:682–691, October 1997.

[87] A. A. Abdo, M. Ajello, A. Allafort, et al. The Second Fermi Large Area Telescope Catalog of Gamma-Ray Pulsars. *ApJS*, 208:17, October 2013. doi: 10.1088/0067-0049/208/2/17.

[88] S. Kisaka and Y. Kojima. Multi-wavelength Emission Region of γ-Ray Emitting Pulsars. *ApJ*, 739:14, September 2011. doi: 10.1088/0004-637X/739/1/14.

[89] J. Pétri. A unified polar cap/striped wind model for pulsed radio and gamma-ray emission in pulsars. *MNRAS*, 412:1870–1880, April 2011. doi: 10.1111/j.1365-2966.2010.18023.x.

[90] D. A. Kniffen, R. C. Hartman, D. J. Thompson, G. F. Bignami, and C. E. Fichtel. Gamma radiation from the Crab Nebula above 35 MeV. *Nature*, 251:397–399, October 1974. doi: 10.1038/251397a0.

[91] D. J. Thompson, C. E. Fichtel, D. A. Kniffen, and H. B. Ogelman. SAS-2 high-energy gamma-ray observations of the VELA pulsar. *ApJ*, 200:L79–L82, September 1975. doi: 10.1086/181902.

[92] M. Tavani, G. Barbiellini, A. Argan, et al. The AGILE Mission. *A&A*, 502: 995–1013, August 2009. doi: 10.1051/0004-6361/200810527.

[93] W. B. Atwood, A. A. Abdo, M. Ackermann, et al. The Large Area Telescope on the Fermi Gamma-Ray Space Telescope Mission. *ApJ*, 697:1071–1102, June 2009. doi: 10.1088/0004-637X/697/2/1071.

[94] F. Acero, M. Ackermann, M. Ajello, et al. Fermi Large Area Telescope Third Source Catalog. *ApJS*, 218:23, June 2015. doi: 10.1088/0067-0049/218/2/23.

[95] M. Ackermann, M. Ajello, A. Allafort, et al. The First Fermi-LAT Catalog of Sources above 10 GeV. *ApJS*, 209:34, December 2013. doi: 10.1088/0067-0049/209/2/34.

[96] J. Aleksić, E. A. Alvarez, L. A. Antonelli, et al. Phase-resolved energy spectra of the Crab pulsar in the range of 50-400 GeV measured with the MAGIC telescopes. *A&A*, 540:A69, April 2012. doi: 10.1051/0004-6361/201118166.

[97] J. Aleksić, S. Ansoldi, L. A. Antonelli, et al. Detection of bridge emission above 50 GeV from the Crab pulsar with the MAGIC telescopes. *A&A*, 565:L12, May 2014. doi: 10.1051/0004-6361/201423664.

[98] Aleksić et al. in preparation. *in preparation*, 2016.

[99] E. Aliu, for the VERITAS Collaboration, T. Arlen, et al. Detection of Pulsed Gamma Rays Above 100 GeV from the Crab Pulsar. *Science*, 334:69–, October 2011. doi: 10.1126/science.1208192.

[100] P. Goldreich and W. H. Julian. Pulsar Electrodynamics. *ApJ*, 157:869, August 1969. doi: 10.1086/150119.

[101] P. A. Sturrock. A Model of Pulsars. *ApJ*, 164:529, March 1971. doi: 10.1086/150865.

[102] M. A. Ruderman and P. G. Sutherland. Theory of pulsars - Polar caps, sparks, and coherent microwave radiation. *ApJ*, 196:51–72, February 1975. doi: 10.1086/153393.

[103] J. K. Daugherty and A. K. Harding. Electromagnetic cascades in pulsars. *ApJ*, 252:337–347, January 1982. doi: 10.1086/159561.

[104] J. K. Daugherty and A. K. Harding. Gamma-Ray Pulsars: Emission from Extended Polar CAP Cascades. *ApJ*, 458:278, February 1996. doi: 10.1086/176811.

[105] L. Oster and W. Sieber. Pulsar geometries. III - The hollow-cone model. *ApJ*, 210:220–229, November 1976. doi: 10.1086/154820.

[106] J. Arons and E. T. Scharlemann. Pair formation above pulsar polar caps - Structure of the low altitude acceleration zone. *ApJ*, 231:854–879, August 1979. doi: 10.1086/157250.

[107] J. Arons. Pair creation above pulsar polar caps - Geometrical structure and energetics of slot gaps. *ApJ*, 266:215–241, March 1983. doi: 10.1086/160771.

[108] A. G. Muslimov and A. K. Harding. Extended Acceleration in Slot Gaps and Pulsar High-Energy Emission. *ApJ*, 588:430–440, May 2003. doi: 10.1086/368162.

[109] K. S. Cheng, C. Ho, and M. Ruderman. Energetic radiation from rapidly spinning pulsars. I - Outer magnetosphere gaps. II - VELA and Crab. *ApJ*, 300:500–539, January 1986. doi: 10.1086/163829.

[110] R. W. Romani. Gamma-Ray Pulsars: Radiation Processes in the Outer Magnetosphere. *ApJ*, 470:469, October 1996. doi: 10.1086/177878.

[111] D. Viganò and D. F. Torres. Modelling of the γ-ray pulsed spectra of Geminga, Crab, and Vela with synchro-curvature radiation. *MNRAS*, 449:3755–3765, June 2015. doi: 10.1093/mnras/stv579.

[112] E. Aliu, H. Anderhub, L. A. Antonelli, et al. Observation of Pulsed γ-Rays Above 25 GeV from the Crab Pulsar with MAGIC. *Science*, 322:1221–, November 2008. doi: 10.1126/science.1164718.

[113] A. A. Abdo, M. Ackermann, M. Ajello, et al. The First Fermi Large Area Telescope Catalog of Gamma-ray Pulsars. *ApJS*, 187:460–494, April 2010. doi: 10.1088/0067-0049/187/2/460.

[114] A. K. Harding and J. K. Daugherty. Pulse profiles and spectra of gamma ray pulsars in the polar cap model. *Advances in Space Research*, 21:251–254, 1998. doi: 10.1016/S0273-1177(97)00811-9.

[115] X.-N. Bai and A. Spitkovsky. Uncertainties of Modeling Gamma-ray Pulsar Light Curves Using Vacuum Dipole Magnetic Field. *ApJ*, 715:1270–1281, June 2010. doi: 10.1088/0004-637X/715/2/1270.

[116] X.-N. Bai and A. Spitkovsky. Modeling of Gamma-ray Pulsar Light Curves Using the Force-free Magnetic Field. *ApJ*, 715:1282–1301, June 2010. doi: 10.1088/0004-637X/715/2/1282.

[117] Y. J. Du, G. J. Qiao, and W. Wang. Radio-to-TeV Phase-resolved Emission from the Crab Pulsar: The Annular Gap Model. *ApJ*, 748:84, April 2012. doi: 10.1088/0004-637X/748/2/84.

[118] MAGIC Collaboration, M. L. Ahnen, S. Ansoldi, et al. Teraelectronvolt pulsed emission from the Crab pulsar detected by MAGIC. *[arXiv:1510.07048]*, October 2015.

[119] W. Bednarek. On the origin of sub-TeV gamma-ray pulsed emission from rotating neutron stars. *MNRAS*, 424:2079–2085, August 2012. doi: 10.1111/j.1365-2966.2012.21354.x.

[120] E. de Oña-Wilhelmi, B. Rudak, J. A. Barrio, et al. Prospects for observations of pulsars and pulsar wind nebulae with CTA. *Astroparticle Physics*, 43:287–300, March 2013. doi: 10.1016/j.astropartphys.2012.08.009.

[121] M. A. Alpar, A. F. Cheng, M. A. Ruderman, and J. Shaham. A new class of radio pulsars. *Nature*, 300:728–730, December 1982. doi: 10.1038/300728a0.

[122] A. A. Abdo, M. Ackermann, M. Ajello, et al. A population of gamma-ray emitting globular clusters seen with the Fermi Large Area Telescope. *A&A*, 524:A75, December 2010. doi: 10.1051/0004-6361/201014458.

[123] P. C. C. Freire, A. A. Abdo, M. Ajello, et al. Fermi Detection of a Luminous γ-Ray Pulsar in a Globular Cluster. *Science*, 334:1107–, November 2011. doi: 10.1126/science.1207141.

[124] C. Venter, O. C. De Jager, and A.-C. Clapson. Predictions of Gamma-Ray Emission from Globular Cluster Millisecond Pulsars Above 100 MeV. *ApJ*, 696:L52–L55, May 2009. doi: 10.1088/0004-637X/696/1/L52.

[125] K. S. Cheng, D. O. Chernyshov, V. A. Dogiel, C. Y. Hui, and A. K. H. Kong. The Origin of Gamma Rays from Globular Clusters. *ApJ*, 723:1219–1230, November 2010. doi: 10.1088/0004-637X/723/2/1219.

[126] W. Bednarek and J. Sitarek. High-energy γ-rays from globular clusters. *MNRAS*, 377:920–930, May 2007. doi: 10.1111/j.1365-2966.2007.11664.x.

[127] H.E.S.S. Collaboration, A. Abramowski, F. Acero, et al. Search for very-high-energy γ-ray emission from Galactic globular clusters with H.E.S.S. *A&A*, 551:A26, March 2013. doi: 10.1051/0004-6361/201220719.

[128] H.E.S.S. Collaboration, A. Abramowski, F. Acero, et al. Very-high-energy gamma-ray emission from the direction of the Galactic globular cluster Terzan 5. *A&A*, 531:L18, July 2011. doi: 10.1051/0004-6361/201117171.

[129] D. A. Kniffen, R. C. Hartman, D. J. Thompson, and C. E. Fichtel. SAS-2 Observations of Gamma Rays from the Galactic Plane. *ApJ*, 186:L105, December 1973. doi: 10.1086/181368.

[130] G. F. Bignami, G. Boella, J. J. Burger, et al. The COS-B experiment for gamma-ray astronomy. *Space Science Instrumentation*, 1:245–268, August 1975.

[131] G. Kanbach, D. L. Bertsch, C. E. Fichtel, et al. The project EGRET (Energetic Gamma-Ray Experiment Telescope) on NASA's Gamma-Ray Observatory (GRO). *Space Sci. Rev.*, 49:69–84, 1988.

[132] P. M. S. Blackett. A possible contribution to the night sky from the Cerenkov radiation emitted by cosmic rays. In *The Emission Spectra of the Night Sky and Aurorae*, page 34, 1948.

[133] A. M. Hillas. Cerenkov light images of EAS produced by primary gamma. *International Cosmic Ray Conference*, 3:445–448, August 1985.

[134] K. Bernlöhr. Simulation of imaging atmospheric Cherenkov telescopes with CORSIKA and sim_telarray. *Astroparticle Physics*, 30:149–158, October 2008. doi: 10.1016/j.astropartphys.2008.07.009.

[135] J. Aleksić, E. A. Alvarez, L. A. Antonelli, et al. Performance of the MAGIC stereo system obtained with Crab Nebula data. *Astroparticle Physics*, 35:435–448, February 2012. doi: 10.1016/j.astropartphys.2011.11.007.

[136] A. Daum, G. Hermann, M. Heß, et al. First results on the performance of the HEGRA IACT array. *Astroparticle Physics*, 8:1–11, December 1997. doi: 10.1016/S0927-6505(97)00031-5.

[137] H. J. Völk and K. Bernlöhr. Imaging very high energy gamma-ray telescopes. *Experimental Astronomy*, 25:173–191, August 2009. doi: 10.1007/s10686-009-9151-z.

[138] G. Heinzelmann and HEGRA Collaboration. Highlights from 6 Years of TeV Gamma-Ray Astrophysics with the HEGRA Imaging Cherenkov Telescopes. *International Cosmic Ray Conference*, 5:2559, July 2003.

[139] A. Barrau, R. Bazer-Bachi, E. Beyer, et al. The CAT imaging telescope for very-high-energy gamma-ray astronomy. *Nuclear Instruments and Methods in Physics Research A*, 416:278–292, October 1998. doi: 10.1016/S0168-9002(98)00749-9.

[140] H. Kubo, A. Asahara, G. V. Bicknell, et al. Status of the CANGAROO-III project. *New A Rev.*, 48:323–329, April 2004. doi: 10.1016/j.newar.2003.12.002.

[141] J. Aleksić, S. Ansoldi, L. A. Antonelli, et al. The major upgrade of the MAGIC telescopes, Part II: A performance study using observations of the Crab Nebula. *Astroparticle Physics*, 72:76–94, January 2016. doi: 10.1016/j.astropartphys.2015.02.005.

[142] N. Park and for the VERITAS Collaboration. Performance of the VERITAS experiment. *[arXiv:1508.07070]*, August 2015.

[143] J. A. Hinton and the HESS Collaboration. The status of the HESS project. *New A Rev.*, 48:331–337, April 2004. doi: 10.1016/j.newar.2003.12.004.

[144] P. Hofverberg, R. Kankanyan, M. Panter, et al. Commissioning and initial performance of the H.E.S.S. II drive system. *[arXiv:1307.4550]*, July 2013.

[145] J. Aleksić, J. Rico, and M. Martinez. Optimized analysis method for indirect dark matter searches with imaging air Cherenkov telescopes. *J. Cosmology Astropart. Phys.*, 10:032, October 2012. doi: 10.1088/1475-7516/2012/10/032.

[146] H.E.S.S. Collaboration, A. Abramowski, F. Acero, et al. Search for Lorentz Invariance breaking with a likelihood fit of the PKS 2155-304 flare data taken on MJD 53944. *Astroparticle Physics*, 34:738–747, April 2011. doi: 10.1016/j.astropartphys.2011.01.007.

[147] B. Zitzer and for the VERITAS Collaboration. Lorentz Invariance Violation Limits from the Crab Pulsar using VERITAS. *[arXiv:1307.8382]*, July 2013.

[148] A. Abramowski, F. Acero, F. Aharonian, et al. Constraints on axionlike particles with H.E.S.S. from the irregularity of the PKS 2155-304 energy spectrum. *Phys. Rev. D*, 88(10):102003, November 2013. doi: 10.1103/PhysRevD.88.102003.

[149] M. Actis, G. Agnetta, F. Aharonian, et al. Design concepts for the Cherenkov Telescope Array CTA: an advanced facility for ground-based high-energy gamma-ray astronomy. *Experimental Astronomy*, 32:193–316, December 2011. doi: 10.1007/s10686-011-9247-0.

[150] B. S. Acharya, M. Actis, T. Aghajani, et al. Introducing the CTA concept. *Astroparticle Physics*, 43:3–18, March 2013. doi: 10.1016/j.astropartphys.2013.01.007.

[151] K. Bernlöhr, A. Barnacka, Y. Becherini, et al. Monte Carlo design studies for the Cherenkov Telescope Array. *Astroparticle Physics*, 43:171–188, March 2013. doi: 10.1016/j.astropartphys.2012.10.002.

[152] F. Acero, A. Bamba, S. Casanova, et al. Gamma-ray signatures of cosmic ray acceleration, propagation, and confinement in the era of CTA. *Astroparticle Physics*, 43:276–286, March 2013. doi: 10.1016/j.astropartphys.2012.05.024.

[153] N. La Palombara, P. Caraveo, M. Fiorini, et al. The INAF ASTRI Project in the framework of CTA. In S. Giani and et al., editors, *Astroparticle, Particle, Space*

Physics and Detectors for Physics Applications - Proceedings of the 14th ICATPP Conference, pages 754–758, June 2014. doi: 10.1142/9789814603164_0119.

[154] V. Vassiliev, S. Fegan, and P. Brousseau. Wide field aplanatic two-mirror telescopes for ground-based γ-ray astronomy. *Astroparticle Physics*, 28:10–27, September 2007. doi: 10.1016/j.astropartphys.2007.04.002.

[155] S. Vercellone, for The ASTRI Collaboration, and f. T. CTA Consortium. The ASTRI mini-array within the future Cherenkov Telescope Array. *[arXiv:1508.00799]*, August 2015.

[156] S. Vercellone, G. Agnetta, L. A. Antonelli, et al. The ASTRI Mini-Array Science Case. *[arXiv:1307.5671]*, July 2013.

[157] S. M. Ransom, P. S. Ray, F. Camilo, et al. Three Millisecond Pulsars in Fermi LAT Unassociated Bright Sources. *ApJ*, 727:L16, January 2011. doi: 10.1088/2041-8205/727/1/L16.

[158] A. A. Abdo, M. Ackermann, M. Ajello, et al. Fermi-LAT Observations of the Geminga Pulsar. *ApJ*, 720:272–283, September 2010. doi: 10.1088/0004-637X/720/1/272.

[159] A. A. Abdo, M. Ackermann, W. B. Atwood, et al. Discovery of Pulsed γ-Rays from the Young Radio Pulsar PSR J1028-5819 with the Fermi Large Area Telescope. *ApJ*, 695:L72–L77, April 2009. doi: 10.1088/0004-637X/695/1/L72.

[160] A. A. Abdo, M. Ackermann, M. Ajello, et al. Fermi Large Area Telescope Detection of Pulsed γ-rays from the Vela-like Pulsars PSR J1048-5832 and PSR J2229+6114. *ApJ*, 706:1331–1340, December 2009. doi: 10.1088/0004-637X/706/2/1331.

[161] A. A. Abdo, M. Ackermann, M. Ajello, et al. The Vela Pulsar: Results from the First Year of Fermi LAT Observations. *ApJ*, 713:154–165, April 2010. doi: 10.1088/0004-637X/713/1/154.

[162] G. C. K. Leung, J. Takata, C. W. Ng, et al. Fermi-LAT Detection of Pulsed Gamma-Rays above 50 GeV from the Vela Pulsar. *ApJ*, 797:L13, December 2014. doi: 10.1088/2041-8205/797/2/L13.

[163] A. A. Abdo, K. S. Wood, M. E. DeCesar, et al. PSR J0007+7303 in the CTA1 Supernova Remnant: New Gamma-Ray Results from Two Years of Fermi Large Area Telescope Observations. *ApJ*, 744:146, January 2012. doi: 10.1088/0004-637X/744/2/146.

[164] P. M. Saz Parkinson, M. Dormody, M. Ziegler, et al. Eight γ-ray Pulsars Discovered in Blind Frequency Searches of Fermi LAT Data. *ApJ*, 725:571–584, December 2010. doi: 10.1088/0004-637X/725/1/571.

[165] A. A. Abdo, M. Ackermann, M. Ajello, et al. Fermi Large Area Telescope Observations of PSR J1836+5925. *ApJ*, 712:1209–1218, April 2010. doi: 10.1088/0004-637X/712/2/1209.

[166] A. A. Abdo, M. Ackermann, M. Ajello, et al. Pulsed Gamma-rays from PSR J2021+3651 with the Fermi Large Area Telescope. *ApJ*, 700:1059–1066, August 2009. doi: 10.1088/0004-637X/700/2/1059.

[167] P. L. Nolan, A. A. Abdo, M. Ackermann, et al. Fermi Large Area Telescope Second Source Catalog. *ApJS*, 199:31, April 2012. doi: 10.1088/0067-0049/199/2/31.

[168] A. A. Abdo, M. Ackermann, M. Ajello, et al. Fermi Large Area Telescope Observations of the Vela-X Pulsar Wind Nebula. *ApJ*, 713:146–153, April 2010. doi: 10.1088/0004-637X/713/1/146.

[169] M.-H. Grondin, R. W. Romani, M. Lemoine-Goumard, et al. The Vela-X Pulsar Wind Nebula Revisited with Four Years of Fermi Large Area Telescope Observations. *ApJ*, 774:110, September 2013. doi: 10.1088/0004-637X/774/2/110.

[170] E. Aliu, S. Archambault, T. Arlen, et al. Discovery of TeV Gamma-Ray Emission from CTA 1 by VERITAS. *ApJ*, 764:38, February 2013. doi: 10.1088/0004-637X/764/1/38.

[171] A. Burtovoi and L. Zampieri. in preparation. *in preparation*, 2016.

[172] E. Aliu, S. Archambault, A. Archer, et al. A Search for Pulsations from Geminga Above 100 GeV with VERITAS. *[arXiv:1412.4734]*, December 2014.

[173] V. A. Acciari, E. Aliu, T. Arlen, et al. Detection of Extended VHE Gamma Ray Emission from G106.3+2.7 with Veritas. *ApJ*, 703:L6–L9, September 2009. doi: 10.1088/0004-637X/703/1/L6.

[174] G. B. Hobbs, R. T. Edwards, and R. N. Manchester. TEMPO2, a new pulsar-timing package - I. An overview. *MNRAS*, 369:655–672, June 2006. doi: 10.1111/j.1365-2966.2006.10302.x.

[175] M. Kerr, P. S. Ray, S. Johnston, R. M. Shannon, and F. Camilo. Timing Gamma-ray Pulsars with the Fermi Large Area Telescope: Timing Noise and Astrometry. *ApJ*, 814:128, December 2015. doi: 10.1088/0004-637X/814/2/128.

[176] J.T. Vanderplas, A.J. Connolly, Ž. Ivezić, and A. Gray. Introduction to astroml: Machine learning for astrophysics. In *Conference on Intelligent Data Understanding (CIDU)*, pages 47 –54, oct. 2012. doi: 10.1109/CIDU.2012.6382200.

[177] Ž. Ivezić, A.J. Connolly, J.T. Vanderplas, and A. Gray. *Statistics, Data Mining and Machine Learning in Astronomy.* Princeton University Press, 2014.

[178] J. Knödlseder, M. Mayer, C. Deil, et al. Towards a common analysis framework for gamma-ray astronomy. *[arXiv:1307.5560]*, July 2013.

[179] B. Bartoli, P. Bernardini, X. J. Bi, et al. Study of the Diffuse Gamma-Ray Emission from the Galactic Plane with ARGO-YBJ. *ApJ*, 806:20, June 2015. doi: 10.1088/0004-637X/806/1/20.

[180] J. Aleksić, E. A. Alvarez, L. A. Antonelli, et al. Observations of the Crab Pulsar between 25 and 100 GeV with the MAGIC I Telescope. *ApJ*, 742:43, November 2011. doi: 10.1088/0004-637X/742/1/43.

[181] T. Oosterbroek, I. Cognard, A. Golden, et al. Simultaneous absolute timing of the Crab pulsar at radio and optical wavelengths. *A&A*, 488:271–277, September 2008. doi: 10.1051/0004-6361:200809751.

[182] A. H. Rots, K. Jahoda, and A. G. Lyne. Absolute Timing of the Crab Pulsar with the Rossi X-Ray Timing Explorer. *ApJ*, 605:L129–L132, April 2004. doi: 10.1086/420842.

[183] T. Mineo, C. Ferrigno, L. Foschini, et al. INTEGRAL observations of the Crab pulsar. *A&A*, 450:617–623, May 2006. doi: 10.1051/0004-6361:20054305.

[184] L. Kuiper, W. Hermsen, G. Cusumano, et al. The Crab pulsar in the 0.75-30 MeV range as seen by CGRO COMPTEL. A coherent high-energy picture from soft X-rays up to high-energy gamma-rays. *A&A*, 378:918–935, November 2001. doi: 10.1051/0004-6361:20011256.

[185] G. Theureau, N. Coudreau, N. Hallet, et al. Kinematics of the local universe . XII. 21-cm line measurements of 586 galaxies with the new Nançay receiver. *A&A*, 430:373–383, January 2005. doi: 10.1051/0004-6361:20047152.

[186] G. Hobbs, A. G. Lyne, M. Kramer, C. E. Martin, and C. Jordan. Long-term timing observations of 374 pulsars. *MNRAS*, 353:1311–1344, October 2004. doi: 10.1111/j.1365-2966.2004.08157.x.

[187] C. Germanà, L. Zampieri, C. Barbieri, et al. Aqueye optical observations of the Crab Nebula pulsar. *A&A*, 548:A47, December 2012. doi: 10.1051/0004-6361/201118754.

[188] L. Zampieri, A. Čadež, C. Barbieri, et al. Optical phase coherent timing of the Crab nebula pulsar with Iqueye at the ESO New Technology Telescope. *MNRAS*, 439:2813–2821, April 2014. doi: 10.1093/mnras/stu136.

[189] Y. Terada, T. Enoto, R. Miyawaki, et al. In-Orbit Timing Calibration of the Hard X-Ray Detector on Board Suzaku. *PASJ*, 60:25, January 2008.

[190] G. Cusumano, V. La Parola, M. Capalbi, et al. Timing accuracy of the Swift X-Ray Telescope in WT mode. *A&A*, 548:A28, December 2012. doi: 10.1051/0004-6361/201219968.

[191] M. G. F. Kirsch, G. Schönherr, E. Kendziorra, et al. The XMM-Newton view of the Crab. *A&A*, 453:173–180, July 2006. doi: 10.1051/0004-6361:20054783.

[192] A. Pellizzoni, M. Pilia, A. Possenti, et al. High-Resolution Timing Observations of Spin-Powered Pulsars with the AGILE Gamma-Ray Telescope. *ApJ*, 691:1618–1633, February 2009. doi: 10.1088/0004-637X/691/2/1618.

[193] L. Kuiper, W. Hermsen, R. Walter, and L. Foschini. Absolute timing with IBIS, SPI and JEM-X aboard INTEGRAL. Crab main-pulse arrival times in radio, X-rays and high-energy gamma -rays. *A&A*, 411:L31–L36, November 2003. doi: 10.1051/0004-6361:20031353.

[194] L. Zampieri. in preparation.

[195] F. Aharonian, A. Akhperjanian, M. Beilicke, et al. The Crab Nebula and Pulsar between 500 GeV and 80 TeV: Observations with the HEGRA Stereoscopic Air Cerenkov Telescopes. *ApJ*, 614:897–913, October 2004. doi: 10.1086/423931.

[196] J. Grube. Observations of the Crab Nebula with the Whipple 10 m Telescope. *International Cosmic Ray Conference*, 2:691–694, 2008.

[197] C. Masterson and CAT Collaboration. Observations of the Crab Nebula with the CAT Imaging Atmospheric Čerenkov Telescope. In F. A. Aharonian and H. J. Völk, editors, *American Institute of Physics Conference Series*, volume 558 of *American Institute of Physics Conference Series*, page 753, April 2001.

[198] Kieda D. B. for the VERITAS Collaboration. The Gamma Ray Detection sensitivity of the upgraded VERITAS Observatory. *[arXiv:1308.4849]*, August 2013.

[199] A. Shearer, B. Stappers, P. O'Connor, et al. Enhanced Optical Emission During Crab Giant Radio Pulses. *Science*, 301:493–495, July 2003. doi: 10.1126/science.1084919.

[200] J. Hinton, G. Hermann, P. Krötz, and S. Funk. Precision measurement of optical pulsation using a Cherenkov telescope. *Astroparticle Physics*, 26:22–27, August 2006. doi: 10.1016/j.astropartphys.2006.04.008.

[201] A. Golden, A. Shearer, R. M. Redfern, et al. High speed phase-resolved 2-d UBV photometry of the Crab pulsar. *A&A*, 363:617–628, November 2000.

[202] I. Mochol and J. Pétri. Very high energy emission as a probe of relativistic magnetic reconnection in pulsar winds. *MNRAS*, 449:L51–L55, April 2015. doi: 10.1093/mnrasl/slv018.

[203] K. W. Weiler and N. Panagia. VELA X and the evolution of Plerions. *A&A*, 90: 269–282, October 1980.

[204] M. I. Large, A. E. Vaughan, and B. Y. Mills. A Pulsar Supernova Association? *Nature*, 220:340–341, October 1968. doi: 10.1038/220340a0.

[205] M. D. Johnson, C. R. Gwinn, and P. Demorest. Constraining the Vela Pulsar's Radio Emission Region Using Nyquist-limited Scintillation Statistics. *ApJ*, 758:8, October 2012. doi: 10.1088/0004-637X/758/1/8.

[206] P. Moran, R. P. Mignani, and A. Shearer. HST optical polarimetry of the Vela pulsar and nebula. *MNRAS*, 445:835–844, November 2014. doi: 10.1093/mnras/stu1791.

[207] R. P. Mignani, S. Zharikov, and P. A. Caraveo. The optical spectrum of the Vela pulsar. *A&A*, 473:891–896, October 2007. doi: 10.1051/0004-6361:20077774.

[208] D. Sanwal, G. G. Pavlov, O. Y. Kargaltsev, et al. X-ray Spectrum and Pulsations of the Vela Pulsar. In P. O. Slane and B. M. Gaensler, editors, *Neutron Stars in Supernova Remnants*, volume 271 of *Astronomical Society of the Pacific Conference Series*, page 353, 2002.

[209] H. Rishbeth. Radio Emission from the Vela-Puppis Region. *Australian Journal of Physics*, 11:550, December 1958. doi: 10.1071/PH580550.

[210] C. B. Markwardt and H. Ögelman. An X-ray jet from the Vela pulsar. *Nature*, 375:40–42, May 1995. doi: 10.1038/375040a0.

[211] D. A. Frail, M. F. Bietenholz, and C. B. Markwardt. A Radio/X-Ray Comparison of the Vela X Region. *ApJ*, 475:224–230, January 1997.

[212] D. C.-J. Bock, A. J. Turtle, and A. J. Green. A High-Resolution Radio Survey of the VELA Supernova Remnant. *AJ*, 116:1886–1896, October 1998. doi: 10.1086/300563.

[213] F. Aharonian, A. G. Akhperjanian, A. R. Bazer-Bachi, et al. First detection of a VHE gamma-ray spectral maximum from a cosmic source: HESS discovery of the Vela X nebula. *A&A*, 448:L43–L47, March 2006. doi: 10.1051/0004-6361:200600014.

[214] O. C. de Jager, P. O. Slane, and S. LaMassa. Probing the Radio to X-Ray Connection of the Vela X Pulsar Wind Nebula with Fermi LAT and H.E.S.S. *ApJ*, 689:L125–L128, December 2008. doi: 10.1086/595959.

[215] D. Horns, F. Aharonian, A. Santangelo, A. I. D. Hoffmann, and C. Masterson. Nucleonic gamma-ray production in ¡ASTROBJ¿Vela X¡/ASTROBJ¿. *A&A*, 451: L51–L54, June 2006. doi: 10.1051/0004-6361:20065116.

[216] A. Pellizzoni, A. Trois, M. Tavani, et al. Detection of Gamma-Ray Emission from the Vela Pulsar Wind Nebula with AGILE. *Science*, 327:663–, February 2010. doi: 10.1126/science.1183844.

[217] A. R. Duncan, R. T. Stewart, R. F. Haynes, and K. L. Jones. A deep radio continuum survey of the southern Galactic plane at 2.4 GHz. *MNRAS*, 277:36–52, November 1995.

[218] B. Aschenbach. Discovery of a young nearby supernova remnant. *Nature*, 396: 141–142, November 1998. doi: 10.1038/24103.

[219] W. Voges, B. Aschenbach, T. Boller, et al. The ROSAT all-sky survey bright source catalogue. *A&A*, 349:389–405, September 1999.

[220] T. Murphy, T. Mauch, A. Green, et al. The second epoch Molonglo Galactic Plane Survey: compact source catalogue. *MNRAS*, 382:382–392, November 2007. doi: 10.1111/j.1365-2966.2007.12379.x.